Statistical Classification of Jupiter's Aurora - A joint analysis of complementary Juno observations

Inaugural-Dissertation

zur Erlangung des Doktorgrades
der Mathematisch-Naturwissenschaftlichen Fakultät
der Universität zu Köln

vorgelegt von

Annika Pia Salveter

aus Troisdorf

Köln, 2023

Berichterstatter:	Prof. Dr. Joachim Saur
(Gutachter)	Prof. Dr. Bülent Tezkan
Tag der mündlichen Prüfung:	19.01.2024

ABSTRACT

Jupiter's aurora is the most powerful in our solar system and challenges our understanding due to its variable shape and intensities. The Jupiter magnetosphere, influenced by rapid rotation, a strong magnetic field, and Io's mass load, was studied extensively by the Juno mission, which arrived in 2016. Juno's observations of the auroral region, especially its low-altitude polar crossings, revealed diverse phenomena, questioning existing knowledge. The hypothesis that powerful wave-particle interactions cause auroral acceleration is gaining increasing attention while raising questions about the initial assumption that static electron potentials are responsible for intense emission. Measurements supporting this hypothesis are rarely seen, making it difficult to compare them with the auroral features we observe on Earth.

This study aims to explore acceleration theories driving Jupiter's auroras by calculating electron distribution occurrence rates and studying their connection with magnetic field changes and ultraviolet emissions, which is essential for understanding the auroras. Therefore, we combine data from 20 flybys, offering a global perspective by statistically comparing the perijoves observations, rather than focusing on individual local observations. The approach of this is to connect associated various instrument data, combining magnetic fields, electron intensities, and UV emissions, to better understand the electron acceleration mechanisms and processes that generate the intense auroral features.

This study found a link between the intense auroras on Jupiter and broadband broad electron energy distributions and azimuthal magnetic field deviations of several 100 nT, indicating field-aligned currents. Thus, stochastic processes might predominantly accelerate intense electron beams, occasionally involving electrostatic structures. Upward and downward beams aligned with the associated currents and bidirectional distributions in downward current regions are observed. Bidirectional electron distributions in downward current regions contradict electrostatic currents, providing adequate intensities for intense auroras. The electron beams display broadband energy distributions through energies from 30-1000 keV, contributing to 93% of auroral emissions, highlighting the importance of

stochastic processes. Significant magnetic field fluctuations of 100 nT were observed when the diffuse aurora was present at lower magnetic latitudes ($< 76°$). Despite magnetometer limitations at low altitudes, observations at up to 8 R_J revealed minor magnetic field fluctuations of a few nT occurring in one-second intervals during main emission crossings. Thus, minor magnetic field changes on periods shorter than a few seconds may indicate the acceleration of auroral electrons due to the interactions with related waves.

Examining various plasma characteristics revealed that electrostatic current and wave-particle interaction contribute significantly to intense auroral arcs on Jupiter. Wave-particle interactions are especially prominent. The coexistence of these accelerations underscores Jupiter's magnetospheric variability. Enhancing this analysis in spatial and temporal coverage by the Juno data and using the full range of Juno instruments would be valuable. Comparing plasma properties on a global scale is beneficial in uncovering the complex interaction of the various acceleration mechanisms to understand the most dazzling auroral phenomena observed in the solar system, the Jovian aurora.

KURZZUSAMMENFASSUNG

Die Aurora des Jupiters ist die stärkste in unserem Sonnensystem und stellt unser Verständnis aufgrund ihrer variablen Strukturen und Intensitäten infrage. Jupiter's Magnetosphäre ist hauptsächlich dominiert durch seine schnelle Rotation, ein starkes intrinsisches Magnetfeld und den Massenauswurf von Io. Die Magnetosphäre konnte bereits durch mehrere Raumsonden untersucht werden, darunter die Juno-Mission, welche Jupiter im Jahre 2016 erreichte. Junos Beobachtungen der polaren Aurora, insbesondere ihrer Polarüberquerungen in niedrigen Breitengraden, enthüllten vielfältige Phänomene und hinterfragten vorhandenes Wissen. Die Hypothese, dass starke Wechselwirkungen zwischen Wellen und Teilchen die Beschleunigung der Aurora verursachen, gewinnt zunehmend an Aufmerksamkeit und stellt die anfängliche Annahme infrage, dass statische Elektronenpotenziale für intensive Emissionen verantwortlich sind. Beobachtungen, die diese Hypothese unterstützen, werden selten beobachtet und lassen sich daher nur bedingt mit den Polarlichtern der Erde vergleichen. Diese Studie zielt darauf ab, die Theorien zur Erzeugung der Jupiter-Aurora zu erforschen, indem das Auftreten von verschiedenen Elektronenverteilungen bestimmt und die Verbindung zu Abweichungen des Magnetfeldes und ultravioletten Emissionen untersucht wird.

Daher kombinieren wir Daten von den ersten 20 polaren Vorbeiflügen und bieten eine globale Übersicht, indem wir die Vorbeiflüge statistisch vergleichen, anstatt uns auf einzelne lokale Beobachtungen zu konzentrieren. Unser Ansatz vereint verschiedene Instrumentendaten, darunter Magnetfelder, Elektronenintensitäten und UV-Emissionen, um eine Vielzahl verschiedener physikalischer Parameter zu beobachten und den Prozess von der Beschleunigung von Elektronen über elektromagnetische Beschleunigung bis zur Anregung von atmosphärischen Atomen durch die verursachenden Elektronen nachzuverfolgen.

Diese Studie hat eine Verbindung zwischen den intensiven Polarlichtern auf Jupiter und breitbandigen Elektronenenergieverteilungen sowie azimutalen magnetischen Feldabweichungen von mehreren 100 nT gefunden, die auf feldausgerichtete Ströme hinweisen. Somit könnten vorwiegend stochastische Prozesse intensive Elektronenstrahlen beschleuni-

gen, gelegentlich unter Beteiligung elektrostatischer Strukturen. Aufwärts und abwärts gerichtete Strahlen, die mit den zugehörigen Strömen ausgerichtet sind, sowie bidirektionale Verteilungen in abwärts gerichteten Stromgebieten werden beobachtet. Bidirektionale Elektronenverteilung in Regionen mit abwärts gerichteten Strömen liefern ausreichende Intensitäten für intensive Aurora und widersprechen dem Bild von elektrostatischen Strömen.

Die Elektronenstrahlen zeigen breitbandige Energieverteilungen im Bereich von 30−1000 keV und tragen zu 93% der polaren Emissionen bei, was die Bedeutung von stochastischen Prozessen hervorhebt. Signifikante Magnetfeldschwankungen von 100nT wurden beobachtet, wenn das diffuse Polarlicht in niedrigeren magnetischen Breitengraden (76°) vorhanden war. Trotz Einschränkungen der Auflösung von Magnetfelddaten auf kleinen Skalen bei niedrigen Höhen zeigten Beobachtungen in Höhen von bis zu 8 R_J geringfügige Magnetfeldschwankungen von wenigen nT, die in Ein-Sekunden-Intervallen während der Hauptemissionsüberquerungen auftraten. Daher könnten geringfügige Magnetfeldveränderungen in Zeiträumen von weniger als wenigen Sekunden auf die Beschleunigung Aurora-Elektronen durch Wechselwirkungen mit entsprechenden Wellen hinweisen.

Die Untersuchung verschiedener Plasmaparameter zeigte, dass elektrostatische Ströme und Wechselwirkungen zwischen Wellen und Teilchen erheblich zu intensiven Polarlichtern auf Jupiter beitragen. Wechselwirkungen zwischen Wellen und Teilchen sind hierbei besonders relevant. Die räumliche Nähe der Beschleunigungen unterstreicht die Variabilität der Jupiter-Magnetosphäre. Eine Erweiterung dieser Analyse durch erweiterte räumliche und zeitliche Abdeckung der Juno-Daten sowie die Nutzung des gesamten Instrumentenspektrums von Juno wäre sehr wertvoll. Der Vergleich der Plasmaeigenschaften auf globalen Skalen wäre sehr hilfreich, um die komplexen Wechselwirkungen der verschiedenen Beschleunigungsmechanismen zu verstehen und die faszinierendsten Polarlichtphänomene von Jupiter zu verstehen.

CONTENTS

LIST OF FIGURES

LIST OF TABLES

List of abbreviations

LC	loss cone
FA	field-aligned
FAC	field-aligned current
PA	pitch angle
PAD	pitch angle distribution
DifA	Diffuse aurora
ZI	Zone I
ZII	Zone II
UW	upward
DW	downward
Bidir	bidirectional
BB	broadband
Mono	mono-energetic
Juno	Jupiter Polar Orbiter
HST	Hubble Space Telescope
JEDI	Jupiter Energetic-particle Detector Instrument
JADE	Jovian Auroral Distributions Experiment
Waves	Plasma Waves Instrument
UVS	UV Spectrometer
JIRAM	Jovian Infrared Auroral Mapper
JunoCAM	Juno Camera
IUE	International Ultraviolet Explorer
UVS	Juno Ultraviolet Spectrograph
MAG	Juno Magnetometer
FGM	Fluxgate Magnetometer
SSD	solid state detector
SNR	signal to noise ratio
UV	Ultraviolet
JRM09	Juno Reference Model through Perijove 9
JRM33	Juno Reference Model through Perijove 33
SysIII	Jupiter System III coordinates
Con81	Connerney 1981 current sheet model
Con2020	Connerney 2020 current sheet model
DFT	Discrete Fourier Transform
PSD	Power Spectral Density
rms	root-mean-square
CWT	Continous Wavelet Transform
COI	Cone-of-Influence

CHAPTER 1

INTRODUCTION

Jupiter's auroras are formed by a combination of factors, including the planet's rotation, the pressure of the solar wind, and the innermost Galilean moons. The strong intrinsic magnetic field, the collisional thick atmosphere, and energetic electrons provided compelling evidence for auroral processes, where auroras are created by the collision of high-energy charged particles with the upper atmosphere, resulting in a wide range of emission brightnesses and shapes. Early satellite findings revealed the auroral region as a corotating high-variable structure, challenging previous knowledge gathered from Earth. Spectroscopic studies of these emissions and measurements of brightness above Jupiter's polar regions help investigate the energy of precipitating particles and the composition and structure of the atmosphere (Bonfond et al., 2009; X. Tao et al., 2011). The Juno spacecraft's arrival in a close orbit around Jupiter has provided compelling insight into the auroral processes that drive the intense and highly variable emissions. As expectations from auroral physics gained from observing Earth's aurora have not provided sufficient explanations for Jupiter's auroral structures, an ongoing discussion exists about the acceleration causes of the energetic electron precipitation. Different acceleration processes are discussed, considering the findings from the Juno mission so far. Juno's array of instruments provides a comprehensive overview of the auroral plasma properties. The combination of trapped, mono-energetic, and stochastic acceleration processes, along with interactions with plasma waves and magnetic field fluctuations, contributes to the complex and dynamic nature of the Jupiter system. By combining the different instrument data, this research yields a better understanding of the generation of auroral emissions. Therefore, the study consists of two parts.

The first part has already been published in the Journal of Geophysical Research - Space Physics. It comprises a classification of the electron distribution to obtain the electron precipitation budget in the Jovian aurora based on Juno's first 20 flybys at Jupiter. Using energy and pitch angles to associate various acceleration mechanisms, we determine the

electron distributions as pancake, field-aligned, mono-energetic, or broadband. Electrons are mostly broadband in energy through 93.0% of the field-aligned distributions, resulting in a minor fraction of mono-energetic structures showing electrostatic potential behavior. The energy flux statistics coincide with the findings. This study indicates that stochastic acceleration dominates the auroral processes in contrast to Earth, where the discrete aurora dominates.

The second part focuses on the interaction between magnetic field variations and particles within Jupiter's magnetosphere. This study expands the analysis using two Juno instruments, Juno Magnetometer (MAG) and Juno Ultraviolet Spectrograph (UVS), to examine magnetic field data and ultraviolet emissions during 20 flybys through polar regions. Intense auroral arcs were observed, along with broadband electron energy distributions and large azimuthal magnetic field deviations corresponding to field-aligned currents, suggesting the presence of strong electron beams accelerated by a stochastic process with occasional electrostatic structures. Magnetic field data were used to investigate potential sources of acceleration due to induced currents, while higher-altitude crossings improved the resolution of the magnetic field data. The magnetic field variations indicate strong electric currents and wave-particle interaction at higher altitudes, thus favoring stochastic and coherent particle acceleration.

In this research, we conducted a detailed examination of data from the Juno spacecraft instruments, which revealed that the most powerful auroral arcs are accompanied by considerable azimuthal magnetic field variations associated with field-aligned currents. The wave-particle interaction and the potential for acceleration through electrostatic forces are likely responsible for generating powerful electron beams, with stochastic acceleration playing a more significant role. Measurements of the magnetic field have revealed signs of wave-particle interactions, which are characterized by periodic fluctuations in the strength of the magnetic field. Examining these alterations with the auroral brightnesses of the Jovian aurora and the related electron distributions can help to understand the processes that drive auroral acceleration. Further investigations that involve more data from Juno's instruments could refine the findings of this study.

CHAPTER 2

JUPITER'S MAGNETOSPHERIC PROCESSES

Jupiter, the largest planet in our solar system, has been visible to the naked eye since before telescopes were invented. In the 17th century, Galileo made the first telescopic observations of Jupiter and its four largest natural satellites, the Galilean moons. Astronomers later studied Jupiter's atmospheric features, including its distinct equatorial bands and the iconic Great Red Spot. Spectroscopic analyses revealed that its composition mirrored that of the Sun, with hydrogen and helium dominating its atmosphere. Further exploration in the mid-20th century led to the detection of non-thermal radio emissions, indicating the presence of a powerful internal magnetic field (Burke & Franklin, 1955). These emissions were attributed to synchrotron radiation from electrons in motion, with the gyrofrequency as the highest frequency, indicating the presence of an internal magnetic field (Field, 1959; Drake & Hvatum, 1959), with a dipolar magnetic field tilt of 11 deg with respect to Jupiter's rotation axis and a dipole moment of $4\,\mathrm{GaussR}_\mathrm{J}^3$ (Kliore et al., 1974), with $\mathrm{R_J}$ the Jovian radii of 71 492 km. As seen from in situ measurements of the Pioneer spacecraft, the magnetic field showed considerable differences in strength and structure between the two hemispheres (Smith et al., 1974, 1975). Radio emissions have also shown variances with the position of Io in its orbit around Jupiter (Bigg, 1964), explained by the Voyager 1 flyby in 1979, showing that Io had intense volcanic activity. With a strong mass loading from Io's volcanic activity, a thin, electrically charged layer, defined as the current sheet, was identified within the equatorial region of Jupiter's magnetosphere. This sheet is essential for the dynamics of Jupiter's magnetosphere and for controlling the flow of charged particles and energy, which influences the planet's auroral emissions. The Voyager 1 and 2 probes in 1979 improved knowledge of the magnetic field and the current sheet, introducing an approximate layer $5\,\mathrm{R_J}$ thick and stretching out from $5\,\mathrm{R_J}$ to $\sim 50\,\mathrm{R_J}$ in radius, also known as the Connerney 1981 current sheet model (Con81) model and a more accurate map of the magnetic field (Connerney et al., 1981; Connerney, 1981). The strong intrinsic magnetic field, the collisional thick atmosphere, and energetic electrons provided

compelling evidence for auroral processes, where auroras are created by the collision of high-energy charged particles with the upper atmosphere, resulting in a wide range of emission brightnesses and shapes.

This chapter introduces Jupiter's auroral emissions and their unique characteristics. Early satellite findings are presented, which revealed the auroral region as a corotating high-variable structure, challenging the previous knowledge gathered from Earth. The northern poles show strong anomalies, resulting in a kidney-shaped emission zone. Different acceleration processes are discussed to deduce possible auroral drivers. Additionally, the chapter introduces the Juno spacecraft, detailing its instruments such as the Jupiter Energetic-particle Detector Instrument (JEDI) and Juno Ultraviolet Spectrograph (UVS). The findings from the Juno mission are also highlighted, including insights into the main emission zone, Jupiter's polar auroral emissions, solar emissions, and satellite footprints.

2.1 Jupiter's Aurora and Magnetospheric Structures

One of the most astonishing revelations by the Voyager spacecraft in 1979 was the first glimpses of Jupiter's auroras at ultraviolet wavelengths, as reported by Broadfoot et al. (1979). These auroras, generated by the collision of high-energy charged particles with the upper atmosphere, were unexpectedly intense. It was known that the auroras on Earth are mainly powered by solar wind particles that interact with the planet's magnetosphere, so the weaker solar wind at Jupiter's distance was expected to produce weaker auroras. However, the Jovian aurora was 100 times more energetic than the terrestrial one, with a surface brightness 10 times higher, indicating a powerful internal mechanism that generated the energy required for the auroras (Broadfoot et al., 1979). With the Voyager ultraviolet spectrometer, auroral emissions were observed, caused by electrons colliding with molecules H_2 and H in the Jovian atmosphere (Waite Jr. et al., 1983). The International Ultraviolet Explorer (IUE) was launched into Earth orbit and showed that the auroral emission regions rotate with Jupiter at a $\sim$10 h spin period (Livengood & Moos, 1990; Clarke et al., 1980) in contrast to Earth, where the emissions are bound to the direction of the solar wind. It was observed that the Jovian aurora is constantly active, with only slight changes from one day to the next. Io-induced aurora has also been observed with a footprint of the Io position equatorward of the main emission zone at various wavelengths, as indicated in Figure 2.1. Over the next ten years of auroral observations, a clear correlation between the brightness distributions and magnetic field lines mapping to $5 - 10$ R_J equatorial distance was observed, with an average power of 4.3 ± 1.510^{13}W for electrons at both poles and variations in brightness on short time scales. However, no long-term trend was detected (Livengood et al., 1992).

With the Hubble Space Telescope (HST) observations, the first direct images of the Jovian aurora were possible, observing ultraviolet wavelengths in 1992. Instruments like the

Faint Object Camera (FOC) and Wide Field and Planetary Camera 2 (WFPC2) mapped the magnetic footprints of the Europa, Ganymede, and Io equatorward of the main oval, therefore deducing the main emission zone to equatorial distances of to $20 - 25\mathrm{R_J}$ (Clarke et al., 2002) with $R_J = 71492$ km as Jupiter's equatorial radius. The bright footprint of Io could be accurately located and used to create a magnetic field model up to the fourth order (Connerney et al., 1998). An exceptional event was recorded in 2007 by Bonfond (2012), where the Ganymede footprint was observed within the main emission zone. The Callisto footprint, located at an equatorial distance of $\sim 26\,\mathrm{R_J}$, is located in the main emissions and thus is still challenging to observe.

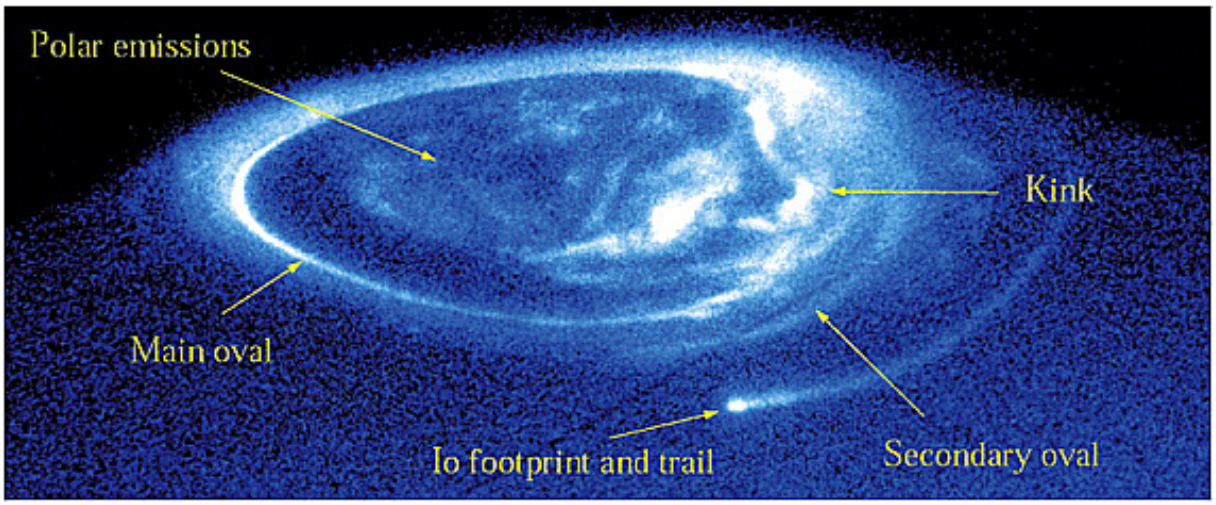

Figure 2.1: A Hubble Space Telescope Imaging Spectrograph (STIS) image is presented here, displaying the ultraviolet auroral emission at the north pole of Jupiter. Captured on the 14th of December 2000, the arrows indicate main auroral features: the main and secondary ovals, the Io footprint, and its trailing tail. The polar emissions, including the "flares", can also be seen poleward of the main oval. The distorted part of the main oval, known as the "kink", is also visible (Grodent, Clarke, Waite, et al., 2003).

The Hubble Space Telescope captured images of the primary aurora, which showed a consistent kidney-bean shape in the northern region, as seen in Figure 2.1 (Grodent, Clarke, Waite, et al., 2003). This was attributed to a magnetic anomaly in the northern hemisphere (Pallier & Prangé, 2001). Extended auroral observations demonstrated stability in both location (with variations of a few degrees) and intensity (with variations by a factor of a few), showing a limited response to solar wind variations (Nichols et al., 2009). The emissions were observed over various wavelengths, from radio to X-rays. X-ray emission was observed and attributed to the precipitation of highly energetic oxygen and sulfur ions around 10 MeV (Elsner et al., 2005; Elsner, 2005; Branduardi-Raymont et al., 2007; Hui et al., 2010; Cravens & Ozak, 2012). Spectroscopic studies of these emissions and measurements of brightness above Jupiter's limb helped diagnose the energy of precipitating particles and the composition and structure of the atmosphere (Bonfond et al., 2009; X. Tao et al., 2011). The main emissions were typically observed with a mean electron energy of around 100 keV, although this energy varies over time and location. For

example, the Io footprint is generated by electrons with a mean energy of approximately 1 keV, while during dawn storms, the mean electron energy reached approximately 460 keV (Bonfond et al., 2009).

Various spacecraft missions, including Ulysses and Galileo, explored the magnetospheric particles, providing details about low-energy electrons (Bame et al., 1992), thermal ion composition (Geiss et al., 1992), and energetic charged particles, including the discovery of field-aligned (FA) beams (Lanzerotti et al., 1993; Cowley et al., 1996; Krupp et al., 1997). Subsequent Galileo observation identified intense magnetic field-aligned electron beams at 20-30 R_J, contributing to significant energy fluxes in the Jovian auroral ionosphere (Frank & Paterson, 2002). These beams, ranging from several keV to tens of keV, supported Jupiter's brightest auroras with complex electric current circuits with upward and downward current regions (Mauk & Saur, 2007). The pitch angle distribution (PAD) of electron beams at higher magnetic latitudes was composed of two distinct regions. Near the planet, the PAD was broad, while far from the planet, the PAD was very pronounced, indicating energetic electron pitch angle diffusion (Frank & Paterson, 2002; Lanzerotti et al., 1993; Seidel et al., 1997; Williams & Mauk, 1997).

These globally resolved auroral pictures with the evidence of field-aligned electron beams provided the basis for theories of magnetospheric structures driving these continuous auroras. Cowley and Bunce (2001) quantitatively examined one of these theories, particularly concerning the amplitude and width of the field-aligned currents, which were in line with the field-aligned current system proposed by Hill et al. (1983). This system connects the magnetosphere and the ionosphere, resulting in partial corotation of the outward diffusion of iogenic plasma in the middle magnetosphere current sheet, located between 20-60 R_J (see section 2.1.1). These field-aligned currents are associated with the main oval emissions, which can generate potentials of around $\sim$100 keV to accelerate electrons up to $\sim$100 keV.

2.1.1 Global Current System and Auroral Drivers

The hypothesis of Hill et al. (1983) suggests that Jupiter's rotation is the primary energy source in its magnetosphere. The rapid rotation, combined with the powerful magnetic field and the internal mass loading of Io, creates a magnetospheric environment that is fundamentally distinct from Earth's. Io acts as the main source of plasma in the Jovian magnetosphere. About 1 ton/s (Delamere, 2004) of plasma is produced in the Io plasma torus and injected into the inner Jovian magnetosphere. This results in a dense plasma torus with peak densities of up to $\sim$3000 particles/cm^3 (Phipps et al., 2018; Bagenal, 1994; Dougherty et al., 2017), accelerated to corotation by Pedersen currents in the Jovian ionosphere. The internal pressure of the iogenic plasma is increased by centrifugal, thermal, and magnetic stresses, resulting in the particles being transported outward. This plasma

is confined to the equatorial region and forms a thin current sheet (Khurana et al., 2004; Thomas et al., 2004).

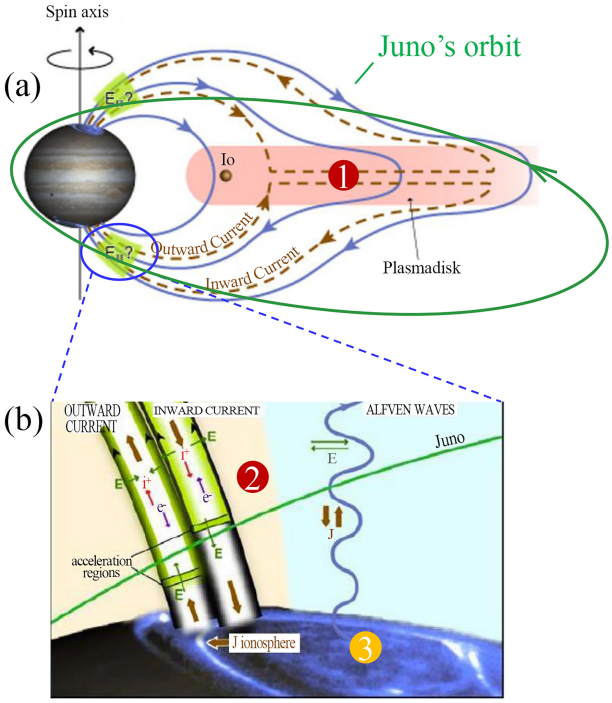

Figure 2.2: Jovian Magnetosphere-Ionosphere-Thermosphere (MIT) coupling connecting the high-latitude ionosphere/thermosphere. Panel (a) shows a sketch of the meridian cross-section of the Jovian magnetosphere, with blue solid lines indicating magnetic field lines and brown dashed curves representing two current loops with magnetic field-aligned currents (FACs). The red shading represents the plasma sheet. Panel (b) provides a close-up view of the Jovian ionosphere, showing the upward and downward FACs and particle acceleration processes related to field-aligned electrostatic potential drops and Alfvén waves. The Juno trajectory is represented schematically by the green curves in both panels. The image is adapted from Wang et al. (2021) using Cowley and Bunce (2001) and Bagenal et al. (2017).

Conservation of angular momentum implies that corotation cannot be sustained. This causes the magnetic field lines to bend back, creating magnetic field stresses in the system. An azimuthal current system is established to maintain corotation, which is powered by $\mathbf{j} \times \mathbf{B}$ forces in the current sheet. The currents in the ionosphere couple to the current sheet along the magnetic field lines, transferring angular momentum from the ionosphere to the particles in the plasma sheet and maintaining partial corotation. This large-scale current system, which is closed along the magnetic field lines to the ionosphere, is known as the magnetosphere-ionosphere (MI) coupling (Cowley & Bunce, 2001; Hill, 1979; Kivelson, 2005) and is schematically displayed in panel (a) of Figure 2.2. The primary distinction between Jupiter's aurora and Earth's aurora was determined to be due to the internal dynamics of Jupiter's magnetosphere rather than the external solar wind as seen on Earth (Cowley & Bunce, 2001; Hill, 2001).

2.1.2 Parallel Electrostatic Potentials

Field-aligned currents (FACs), or Birkeland currents (Hill, 1979), were first studied by Knight (1973) in connection to the Earth. The magnetosphere and ionosphere are linked by parallel potentials created by currents, which accelerate particles along the magnetic field lines and energize the main auroral oval (Nichols & Cowley, 2004; Ray et al., 2010). As particles move through these potentials, they accumulate energy, leading to unidirectional mono-energetic electron distributions. Hill (1979) stated that the strongest currents emerge when the plasma begins to slip behind rigid corotation. Investigations of field-aligned currents in Jupiter's middle magnetosphere have been conducted using Voyager 2 spacecraft magnetometer data, showing the plasma to depart significantly from corotation around $\sim 17 - 20\mathrm{R_J}$ (McNutt et al., 1979). Bunce and Cowley (2001a) and Khurana (2001) discovered radial and azimuthal currents in the current sheet, estimating field-aligned currents into the ionosphere at around $0.1 - 1\ \mathrm{mA/m^2}$, similar to the Earth system. They proposed that weak turbulence generated 100 kV, which increased the magnetospheric electron energy flux and explained Jupiter's main auroral emissions. The upward currents were modeled to correspond to dipolar co-latitudes of 10° to 16° to the ionosphere, with different models from Bunce and Cowley (2001b) and Hill (2001). These discrepancies demonstrate the middle magnetosphere's complexity and plasma transport dynamics in the current sheet, as highlighted by Cowley, Nichols, and Bunce (2002; 2003). Plasma transport in the current sheet is still an unsolved puzzle, particularly when considering the acceleration of Jovian auroral particles. The radial outward expansion of the plasma should lead to cooling, yet it is observed to be heated to temperatures of $\sim$10 keV. Flux tube interchange motions are expected, where flux tubes loaded with denser, cooler plasma move outwards, while relatively empty flux tubes, containing hotter plasma from the outer magnetosphere, move inwards (Thomas et al., 2004). Within radial transport, small-scale magnetic field perturbations have been observed (Saur et al., 2003; Mauk & Saur, 2007; C. Tao et al., 2015, e.g.) proposing an alternative explanation for field-aligned potential drops.

2.1.3 Weak Magnetohydrodynamic Turbulence

Saur et al. (2003) proposed a theory in which non-local force balance by radial mass transport leads to small-scale magnetic perturbations. Here, the coupling between the magnetosphere and the ionosphere is mediated by the weak magnetohydrodynamic (MHD) turbulence observed by the Galileo spacecraft in the middle magnetosphere of Jupiter (Saur et al., 2002). In this process, Alfvén waves non-linearly interact with counter-propagating wave packets that travel along the field lines. This turbulent cascade redistributes the turbulent energy to smaller wavelengths until it is eventually dissipated by Joule heating with an anomalous turbulent resistivity, resulting in a stochastic acceleration of electrons

and ions. An investigation of the plasma characteristics and wave-particle interaction of Alfvén waves by Saur et al. (2018) has revealed evidence that electron Landau damping of kinetic Alfvén waves occurs along dipole L-shells of 30. Energy is transferred from the wave to the particle on the electron inertial length scales, while ion cyclotron damping heats the magnetospheric plasma for $L \gtrsim 30$, as indicated in Figure 2.3. The auroral particles are primarily stochastically accelerated by Alfvén waves rather than by electrostatic potentials to a specific energy, as stated by Saur et al. (2003).

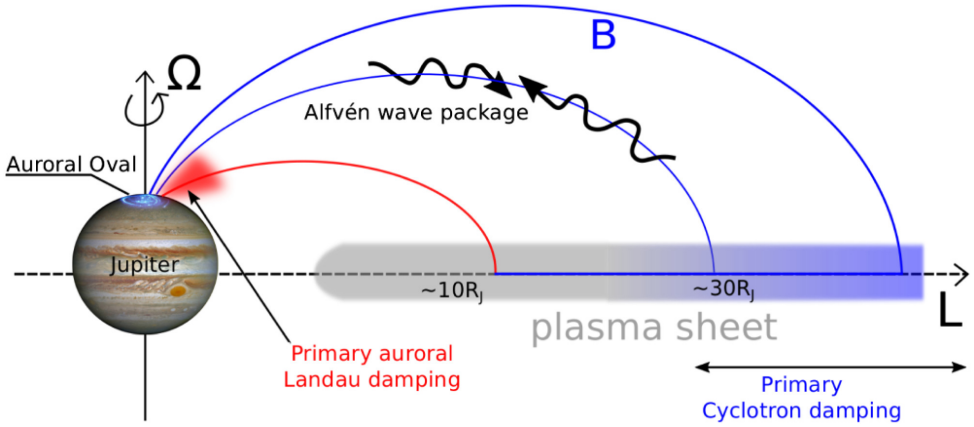

Figure 2.3: Alfvén waves interacting with particles in regions between 10 and 40 $\mathrm{R_J}$. These waves transfer stress between Jupiter's ionosphere and the plasma sheet in its magnetosphere. Within approximately $L = 30$, Alfvén waves dissipate mainly through electron Landau damping in the auroral region above Jupiter's ionosphere. Beyond this distance, Alfvén waves are predominantly dissipated by ion cyclotron damping in Jupiter's plasma sheet. Magnetospheric transport processes create an imbalance between the magnetosphere and ionosphere, leading to magnetosphere-ionosphere coupling through Alfvén waves. This coupling results in stochastic acceleration of particles due to electron Landau and ion cyclotron damping (Saur et al., 2018).

2.2 Juno Spacecraft

In 2011, the Jupiter Polar Orbiter (Juno) spacecraft was launched, giving scientists an unprecedented insight into Jupiter's magnetosphere and auroras. By using low-perijove, polar orbits, Juno's instruments could directly sample Jupiter's polar aurora and measure the precipitating electrons, magnetic field perturbations, and ultraviolet, radio, and infrared emissions. These data have enabled researchers to explore the magnetosphere locally and globally since it arrived in 2016, significantly advancing our understanding of Jupiter's auroras.

The Juno mission has used a variety of instruments, such as the Juno Magnetometer (MAG), the Plasma Waves Instrument (Waves), the Jupiter Energetic-particle Detector Instrument (JEDI), the Jovian Auroral Distributions Experiment (JADE), the Juno Ultraviolet Spectrograph (UVS), the Jovian Infrared Auroral Mapper (JIRAM), and the Juno Camera (JunoCAM), make in situ measurements of fields, particles, and auroral emissions. Juno's mission was to explore the high-latitude regions and the plasma sheet of Jupiter, taking extensive measurements to understand plasma properties, energy flow, and changes in the planet's magnetosphere. The spacecraft's rapid polar crossings through the main aurora at various angles enabled observations of the entire aurora, allowing researchers to differentiate between local-time effects and longitude effects. The mission's primary goals were to characterize structures in the low-density region between the plasma sheet and ionosphere and investigate the connection between the atmosphere, ionosphere, and magnetosphere.

The 53-day capture orbit was designed to reduce fuel consumption, allowing for close measurements of Jupiter's poles while avoiding areas of intense radiation. The spacecraft's orientation was adjusted to protect the instruments from radiation. The orbit precession caused a slight tilt and brought Juno's equatorial crossings closer to Jupiter with each orbit. During its mission, Juno crossed the orbits of Jupiter's moons Callisto, Ganymede, and Europa and is expected to cross Io's orbit in December 2023 during its 57th orbit. The Juno spacecraft moves fast near Jupiter, reaching up to 50 km/s while rotating at a slow rate of 2 RPM. During most polar crossings, the Juno rotation axis is pointed towards Earth, allowing for a strong communication link.

Juno's trajectory has the closest approach, also known as a perijove, with jovicentric radial distances as low as 1.05 Jupiter radii and enables quick collection of data from pole to pole, including azimuthal structures in the atmosphere and interior. The Jovian spin period of 10 hours provides full azimuthal coverage during the 33 flybys, as shown in the right panel of Figure 2.4. The flyby of the northern hemisphere was at a lower altitude than the southern hemisphere due to its orbital inclination, as seen in the left panel of Figure 2.4. This provides valuable magnetic field measurements to obtain a magnetic field model in greater detail, such as Juno Reference Model through Perijove 9 (JRM09)

and Juno Reference Model through Perijove 33 (JRM33), which provided insight into the strength and structure of Jupiter's magnetic field. This allowed for monitoring the auroral particles in each part of the primary emission zone, which rotates in sync with the planet. Due to the variable orientation of Juno from orbit to orbit, as well as the highly variable magnetic field orientation at close distances, the JEDI instrument could not provide a full-pitch angular view through all perijoves, as further discussed in section 2.2.1. JEDI made remarkable observations of the entire space with a temporal resolution of 0.5 s, a feat that had never been accomplished before.

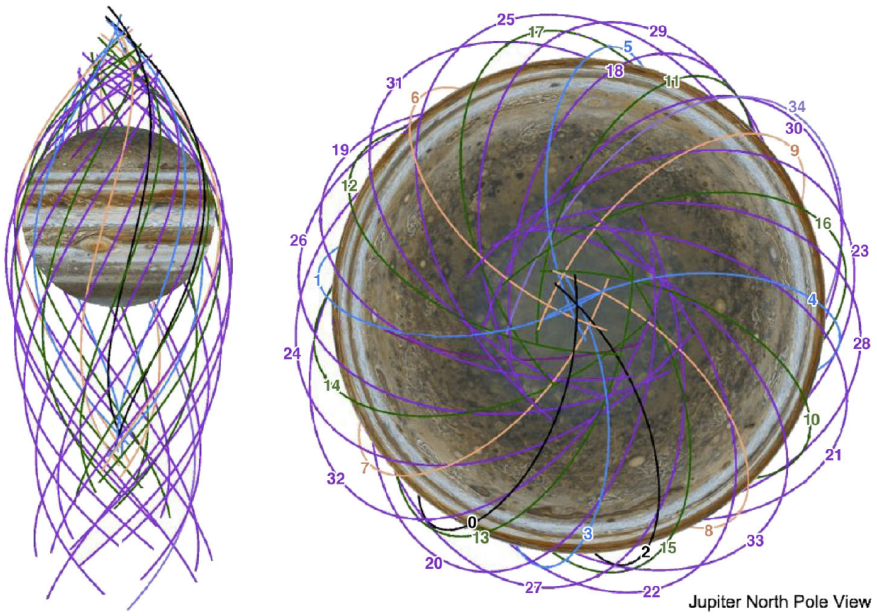

Figure 2.4: The Juno spacecraft's flight trajectory during the initial mission, including the first 33 perijoves. The left side shows a view from the side of Jupiter with the poles at the top and bottom. The right side shows a top view of the northern polar region (Bolton et al., 2017).

2.2.1 Jupiter Energetic-particle Detector Instrument (JEDI)

Because of the spacecraft's rotation rate, both Juno particle instruments, JEDI and JADE, can capture full-angle views every 30 seconds. JEDI and JADE, positioned at angular separations of 120 degrees, cover a broad energy range from a few eV to hundreds of keV. JADE focuses on lower energies, ranging from 0.1 keV to 100 keV for electrons and 0.005 keV to 50 keV for ions, while JEDI handles higher energies, from below 40 keV to over 1000 keV for electrons and 50 keV to 1000 keV for ions. JEDI comprises three identical detectors, as displayed in Figure 2.5, that measure the energy and angle of ions and electrons with a nearly full-pitch angular view. Using microchannel plates (MCP) and solid state detector (SSD), JEDI can measure essential characteristics such as energy, angle, and ion composition while reducing background radiation and ultraviolet foreground. The detector plates are pixelized, offering varying sensitivities and enabling coverage of a

wide electron intensity range. Efficient electron measurements (>20%) are achieved for energies greater than 30 keV.

2.2.2 Pitch Angle Coverage

Due to Juno's slow rotation rate of two spins per minute and a relatively high velocity of 40km/s above Jupiter's poles, achieving an instantaneous full-angle distribution is challenging. The spacecraft's spin axis, always directed towards Earth and the Sun for communication purposes, lies within the dawn-dusk plane. Thus, JEDI captures complete angle distributions using multiple sensor suites mounted around the spacecraft. Two instruments within the equatorial plane provide instant full angular distributions, whereas a third obtains complete distributions every 30 seconds. JEDI instruments are labeled based on their mounting positions (90, 180, 270) relative to the spacecraft's X-Y coordinate system. The JEDI180 viewing fan is restricted to 148° × 12° to avoid solar light contamination, while JEDI90 and JEDI270 have a full angular resolution of 160° × 12°. Each fan consists of six SSDs pointing in different directions, dividing the viewing fan into six roughly 26.7° × 12° fractions. To prevent glint from solar panels, JEDI90 and JEDI270 are tilted by 8° and 10° around two axes, affecting their angle coverage. A full angular view within auroral regions occurs when the viewing fan's normal is nearly orthogonal to the local magnetic field.

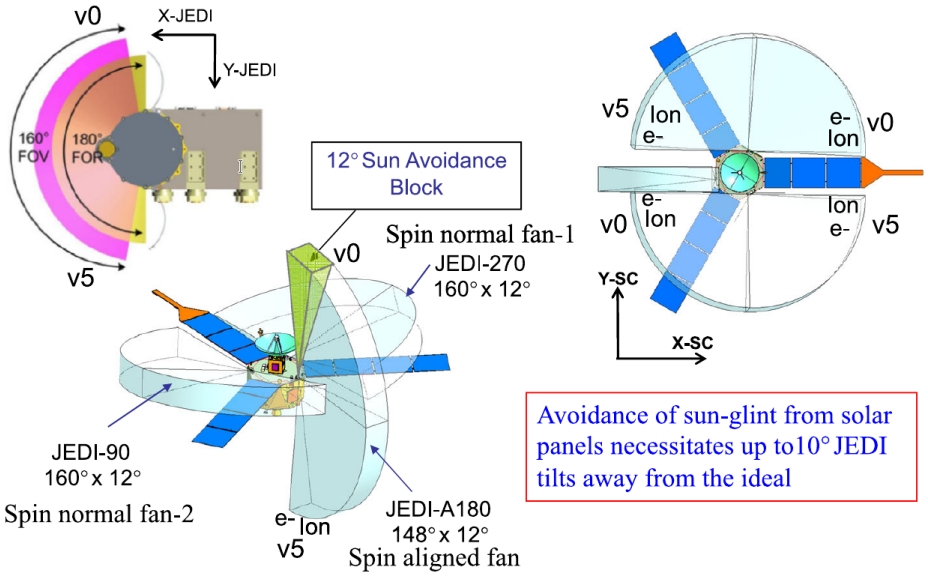

Figure 2.5: The JEDI sensor, mounted on Juno, is designed to measure instantaneous full-pitch angular coverage, encompassing the JEDI Fan 90, 180, and 270. Six solid state detectors monitor each fan, each with a pitch angular resolution of 36.7° × 12° of (Mauk, Haggerty, Jaskulek, et al., 2017).

Particles exposed to a magnetic field with an initial motion will rotate around the magnetic field in circular orbits due to the Lorentz force. If the motion has a component

parallel to the magnetic field, the motion is helical, with a velocity that is perpendicular and parallel to the magnetic field. This angle between the particle's motion and the magnetic field line is known as the pitch angle (PA). As particles move along magnetic field lines into stronger magnetic fields, they experience a retarding force known as the mirror force. The first adiabatic invariant, the magnetic moment $\mu = W_\perp/B$, is the source of this force. Here, B is the magnitude of the magnetic field, and $W_\perp$ is the transverse energy of the particle relative to the magnetic field. As the energy is conserved, the transverse energy must increase, and the parallel energy must decrease until the particle's parallel velocity is zero. Then, the parallel component of the gradient force produces a mirror force that pushes the particle back towards regions of lower magnetic fields. The third magnetic invariant, the magnetic moment expressed as $\mu = \frac{mv^2 \sin^2 \alpha}{2B}$, can be used to determine the pitch angle of a particle along its path along the magnetic field line. This is done by the equation:

$$\frac{\sin^2 \alpha_2}{\sin^2 \alpha_1} = \frac{B_2}{B_1} \tag{2.2.1}$$

Particles that are not reflected before entering the atmosphere can penetrate it. Those with a pitch angle of up to 90° at the atmosphere upper limit will be able to do so, and all particles with a pitch angle that satisfies the equation eq. (2.2.1) in lower magnetic fields will be inside the loss cone. The equation defines this loss cone by

$$\alpha_{LC} = \sin^{-1}\left(\sqrt{\frac{B_{sc}}{B_{atm}}}\right) \tag{2.2.2}$$

where B_{atm} is the magnetic field strength at the upper limit of the atmosphere.

In the context of auroras, pitch angle is essential as it determines whether energetic particles are directed toward the planet to excite atoms in the atmosphere and create auroral emissions. Particles with pitch angles close to 0° or 180° are aligned with the magnetic field. They can lead to phenomena such as auroras, while particles with pitch angles close to 90° do not align with the magnetic field or influence auroral processes. To accurately detect field-aligned particles, especially the pitch angles at both ends (0° and 180°) must be identified. Note that the pitch angle is defined in the direction of the magnetic field, so different pitch angles correspond to a motion toward the planet or away from it. The flyby geometry of the spacecraft can sometimes limit the full-pitch angular view, as the tilting of the spacecraft concerning the magnetic field lines results in a restricted coverage of pitch angles, creating gaps in the observable angles. Even when the pitch angles are almost entirely resolved, the sensors are still sensitive to the incoming angles of the particles, resulting in a Field of View (FOV) with a Full Width at Half Maximum (FWHM) of approximately 17° × 9°. This limitation can lead to misinterpretations of energy flux variations and must be carefully examined before interpreting the data.

2.2.3 Efficiency Correction of Particle Intensities

Shielding mechanisms protect against high-energy radiation, with tungsten-copper blades guarding against electrons >15 MeV and aluminum flashing covering electron sensors shielding protons and ions <250 keV. However, this interaction reduces efficiency for lower energies (Mauk, Haggerty, Jaskulek, et al., 2017). However, a correction method must be applied to the electron intensities to address the electron spectra contaminated by high-energy foreground electrons that penetrate the detector, as stated in Mauk, Haggerty, Paranicas, et al. (2017a); Mauk et al. (2018). Electrons with energies higher than 400 keV can scatter within the detector, leading to measurement at higher energies. The detection efficiency for these scattered electrons is parameterized based on empirical data and given by

$$\epsilon = 1 - \exp\left(-2\left(\frac{480}{E_{keV}}\right)^3\right) \tag{2.2.3}$$

with the kinetic energy of the incoming electron E_{keV}. The electron intensities can be calibrated by dividing them by the efficiency. In addition, each electron that enters the detector leaves a minimum energy deposit of around 160 keV, which is known as a minimum ionizing bump (Mauk, Haggerty, Paranicas, et al., 2017a). It is essential to be aware of these energy deposits, as they can indicate the presence of high MeV electrons in the detector but not necessarily an increase in electron intensity at other energies.

2.2.4 Energy Channel Limits

In order to obtain the global intensity of all JEDI fans, the intensities in each energy channel n are averaged across the SSDs m. Each energy channel has its own empirically determined limits $E_{min}(n,m)$ and $E_{max}(n,m)$, from which the bandpass width $\Delta E = E_{max} - E_{min}$ and the geometric mean $\sqrt{E_{min} \cdot E_{max}}$ can be calculated. The energy limits of each SSD vary by a relative difference of approximately $\sigma/\mu \approx \pm 2.9\%$. To determine the general energy limits for the intensity averages, the minimum and maximum values of the geometric means of each energy channel in all SSDs are first identified, for example, $E_{min}(n) = min(E(n,m))$. Subsequently, the average energies within each channel $E(n)$ and the energy boundary between the different channels E_{limits} are calculated again using the geometric means.

$$E(n) = \sqrt{E_{min}(n) \cdot E_{max}(n)} \tag{2.2.4}$$

$$E_{limit}(n) = \sqrt{E_{min}(n) \cdot E_{max}(n-1)} \tag{2.2.5}$$

The averaged energy bins over all SSDs are then arranged in the sequence $E_{bin} = [E_{min}(0), E_{limit}(n), E_{max}(N)]$.

The average intensity is calculated across the SSDs m after they have been sorted into pitch angle bins to obtain the average intensity across all pitch angles. It is important to exclude energy bins lower than < 30keV, as their probably overestimated intensities could otherwise dominate the intensities.

2.2.5 Energy Flux Calculations

Another important physical factor is the amount of energy expected to be released by the electrons that precipitate into the atmosphere. This energy input is mapped to the auroral processes that are available. It is assumed that no electric field is present beneath the spacecraft that would reduce the energy of electrons moving along the magnetic field line to Jupiter's atmosphere. Therefore, the intensities within the loss cone detected by the spacecraft are equal to or greater than those anticipated at the atmospheric boundary (Mauk, Haggerty, Paranicas, et al., 2017a). Assuming isotropic distributions and only electron velocity through the surface perpendicular to the background magnetic field, one can estimate the energy flux impacting the atmosphere through the given surface by

$$F_E = \pi \int_{E_{min}}^{E_{max}} I \cdot E \; dE \tag{2.2.6}$$

where π is the weighted area projection, which describes the azimuthal and polar integration over the loss cone at the atmospheric boundary and scales the energy flux through the surface. The particle intensity I_n is expressed in $1/(\mathrm{cm}^2\,\mathrm{s}\,\mathrm{sr}\,\mathrm{keV})$, the central energy E_n and the band pass ΔE_n in keV. The equation is written as:

$$F_E = \pi \sum_n I_n E_n \; \Delta E_n \tag{2.2.7}$$

Errors are estimated by considering JEDI's energy resolution of approximately 20% and Poisson counting statistics. However, these statistical errors are insignificant compared to the considerable systematic errors, such as those caused by the spacecraft configuration (Clark et al., 2018).

2.3 Juno Mission Findings

The Juno spacecraft has made significant progress in observing Jupiter's aurora over the past seven years. By providing the first in-situ measurements of the high latitudes close to Jupiter, Juno has enabled direct measurements of critical observables related to the main aurora. Its polar orbits have allowed in situ sampling of low-altitude magnetic field lines that thread Jupiter's polar aurora. The observations of Juno's instruments of the first perijoves challenged previously assumed knowledge of the auroral acceleration of the Jupiter system.

2.3.1 Main Emission Zone

In the initial perijove observations of Jupiter, there was no indication of electrostatic potentials driving the auroral particles linked to the most intense auroral emissions. Instead, the data showed mainly bidirectional broadband electron distributions, showing a power-law distribution that extended into the MeV range (Mauk, Haggerty, Jaskulek, et al., 2017). The first observations by JADE (Allegrini et al., 2017; Szalay et al., 2017) in Jupiter's main auroral oval revealed upward-going electron beams in the north and downward-going beams in the south, also broadband in shape. Auroral structures were found on the scale of a few tens of kilometers. Furthermore, higher-energy data from JEDI showed a net energy flux of approximately $200\mathrm{mW/m^2}$ of the broadband electron beams into Jupiter's auroral atmosphere, which could power the observed auroral emissions. Thus, the precipitating aurora particles appeared to be dominated by bidirectional and diffuse features that exceed the energy fluxes of $3\mathrm{W/m^2}$ (Mauk et al., 2018; Connerney et al., 2017). Both instruments, JEDI and JADE, detected diffuse auroral emissions in a wide area equatorward of the main auroral oval. These emissions were accompanied by precipitating electrons exhibiting nearly complete loss cone distributions, ranging from $0.1 - 700$ keV, and empty upward loss cones. The characteristic energy of these precipitating electrons aligned with the features observed in the auroral Juno-UVS false-color map (Li et al., 2017). The first evidence of inverted V energy distributions within the JEDI measurements was observed during the third flyby by Clark, Mauk, Haggerty, et al. (2017), with enhanced intensities at several hundreds of keV, indicating large-scale parallel electric potentials. JADE observed both inverted V structures and bidirectional distributions in the range of 1.4 to 2.9 $\mathrm{R_J}$. The upward flux of electron energy exceeded the downward flux ($0.01\,\mathrm{mW/m^2}$ to $5\,\mathrm{mW/m^2}$), potentially contributing to the $0.1 - 50$ kR ultraviolet emission (Ebert et al., 2017). The fifth perijove provided evidence of the acceleration region below the spacecraft as the ultraviolet brightness could not be solely deduced from downward energy fluxes but upward energy fluxes (Ebert et al., 2019), despite other bidirectional electron beams being capable of producing polar Ultraviolet (UV) emissions of comparable strength.

Several studies have been performed to explore the potential for possible acceleration

processes by observing plasma properties. Kotsiaros et al. (2019) studied magnetic field fluctuations that showed Birkeland currents related to auroral glows. The intensity and size of the currents are weaker and more filamentary than expected, which did not account for the expected currents of the northern and southern auroras. A multi-instrument study observed a dawn storm, with ultraviolet emissions accompanied by electron distributions ranging from 10 to 1,000 keV, providing the energy flux for the UV emissions. The more energetic electrons had 160–280 keV energies and downward energy fluxes that significantly contributed to UV emissions (Ebert et al., 2021). Magnetic field perturbations indicated both upward and downward field-aligned currents (FACs) and the presence of whistler mode waves. Observations of magnetic field fluctuations also showed the presence of Alfvénic turbulence in high-latitude regions related to auroral broadband aurora emissions with the Poynting flux reaching up to 100 mW/m^2 (Gershman et al., 2019). These turbulent magnetic field fluctuations link to the central plasma sheet in the inner magnetosphere. Lorch et al. (2022) also observed in Jupiter's mid-high latitude magnetosphere magnetic field fluctuations and revealed Alfvénic activity, characterized by turbulence and energy dissipation at the electron inertial scale. Calculations showed that the Poynting flux of these turbulent perturbations is significant to drive auroral emissions. Earlier studies have already proposed that broadband acceleration of auroral particles can be achieved by Alfvén waves propagating in the ionospheric Alfvén resonator, which is consistent with recent Juno observations (Lysak et al., 2021; Damiano et al., 2019). Several observations concerning the auroral high-latitude zone deduced another form of particle acceleration. According to Clark, Mauk, Haggerty, et al. (2017), JEDI detected protons with energies of around 200 keV with a conic shape. The conic shape suggests that these protons were accelerated away from the planet by energetic electron beams that created waves that propelled the protons out of the ionosphere. Observations of whistler mode waves above the poles of Jupiter were made during the first perijove when the Juno Wave instrument detected broadband plasma wave emission (ranging from 50 Hz to 40 kHz). Thus, whistler mode, likely caused by an energetic upgoing electron beam, leads to pitch angle scattering of these upgoing electrons away from the magnetic field line (Tetrick et al., 2017; Elliott, Gurnett, Kurth, Clark, et al., 2018). Kurth et al. (2018) deduced a strong correlation between probable intense whistler mode waves and intense downward fluxes of electrons with a broad energy spectrum, mapping to auroral bright spots by Haewsantati et al. (2023). Indirect observations of high-energy electrons by UVS observed a barcode pattern, indicating high energetic MeV electron bursts on time scales of $0.1 - 1$ s, indicating whistler waves. Furthermore, whistler mode waves are deduced to be the primary driver of diffuse auroral precipitation from several keV to several hundred keV (Li et al., 2017, 2021; Radioti et al., 2009). An extensive statistical analysis of proton energy fluxes revealed that the pitch angle distributions are mostly field-aligned at $M > 25$ and become more pancake-shaped at smaller M-shells (Shen et al., 2022). For energies

between $10 - 50$ keV, the pitch angle distributions are field-aligned between $M = 7$ and $M = 20$, which is consistent with the charge exchange of protons with neutral toroidal clouds (Sarkango et al., 2023).

Mauk et al. (2020) has introduced an overview of regions with common auroral structures, classifying the main emission zone into three distinct zones, focusing on the dusk hemisphere due to Juno's orbit configuration:

The Diffuse aurora (DifA) zone located at small M- and L-shells, mainly at the equatorward edge of the main emission zone, is defined by high intensities outside the loss cone with likely more intensities in downward than upward direction. Empty upward-loss cones underline the assumption of diffuse aurora in these regions. Sulaiman et al. (2022) suggested that Alfvénic fluctuations are most noticeable in the diffuse aurora and tend to decrease in intensity in Zone-I and Zone-II, likely due to dissipation, as altitude increases, thus providing energy to auroral electrons.

The downward flux region Zone I (ZI) at intermediate latitudes has electron intensities that are higher inside the downward loss cone than outside, with more intense downward electron intensities and energy fluxes than upward ones. This zone includes both downward electron inverted V's and broadband acceleration and is associated with upward magnetic field-aligned electric currents.

The Zone II (ZII) region located at higher latitudes has electron intensities within the upward loss cone that are higher than those outside. This region's upward intensities and energy fluxes are equal to or greater than the downward ones. Although the downward fluxes are low, ZII can still produce visible auroral emissions and link to upward acceleration in the opposite hemisphere. It sometimes displays downward ion inverted V's and could involve downward electrostatic acceleration of ions.

ZI and ZII link to upward and downward current regions, respectively, resulting in dominant unidirectional electron and ion accelerations. Thus ZI emissions are likely stronger than ZII emissions as seen in Figure 2.6, where Sulaiman et al. (2022) marked observed auroral events associated with both zones. The upward and downward electric currents observed by Kotsiaros et al. (2019) correspond well to the introduced Zone-I and Zone-II. ZI is associated with upward magnetic field-aligned currents, which leads to downward electron acceleration. These electron distributions can be coherent or broadband in electron spectra, with the latter providing the most intense electron energy flux. Mauk et al. (2023) noticed that when a strong downward electron broadband acceleration occurs, downward electron electrostatic acceleration disappears, and the cause of the broadband preference over coherence is still unknown.

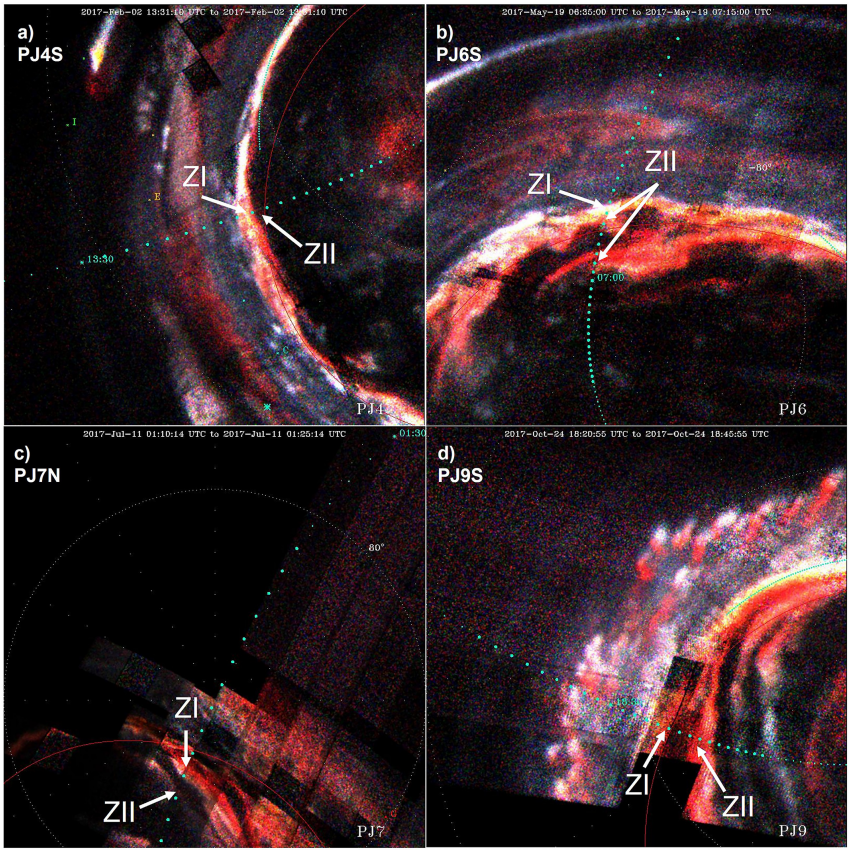

Figure 2.6: Orthographic projections of false-color ultraviolet images depicting Jupiter's aurora for several events. Magnetic footprint tracks of Juno, separated by 1-minute intervals, are superimposed. (Sulaiman et al., 2022)

Sulaiman et al. (2022) has found large-scale electron density reductions, known as auroral cavities, in Jupiter's polar regions between the diffuse aurora and Zone-I. Additionally, a significant decrease in Alfvénic fluctuations was observed between both regions, indicating their dissipation at higher altitudes. Given a specific Poynting flux, the magnetic field fluctuations would decrease with decreasing densities as the Alfvén speed would increase accordingly. Therefore, the lack of magnetic field fluctuations observed over Zone-I may be due to diminishing magnetic field amplitudes caused by density reductions. Moreover, density depletions are directly linked to auroral particle acceleration while reducing the number of charge carriers for a strong field-aligned current. A clear physical boundary to the polar cap could not be deduced by Mauk et al. (2020), possibly indicating a quantitative difference in plasma and energetic particle availability rather than a qualitative one.

2.3.2 Jupiter's Polar Auroral Emissions

The auroral emissions over Jupiter's polar cap are highly variable and differ from the satellite footprint and the main oval auroral emissions. Observing at high latitudes, these polar auroras map to distant regions in Jupiter's magnetosphere, approximately from 30 R_J to open field lines, and exhibit significant local-time effects. Polar emissions contribute

$\sim 30\%$ to the total auroral brightness and show bursts that last ~ 100s (Grodent, Clarke, Kim, et al., 2003). A comprehensive study of UV and IR observations has identified three polar cap regions: a dark area on the dawn side connected to inward-flowing magnetospheric plasma, an active region with bright flares around noon, and a swirl region with patchy emissions, possibly linked to solar wind reconnection (Bonfond et al., 2017; Grodent, Clarke, Waite, et al., 2003). Figure 2.7 presents an overview of the Jovian auroral emissions observed with the Hubble Space Telescope, with arrows pointing to the various regions. Auroral emissions in the swirl region show expanding circles with a typical brightness of up to 140 kR magnetically mapping to the outer magnetosphere, possibly generated by dayside reconnections (Hue et al., 2021; Greathouse et al., 2021). Reconnection events could be responsible for producing high-energy electron beams, which could explain the enigmatic polar auroras of Jupiter (Masters et al., 2021).

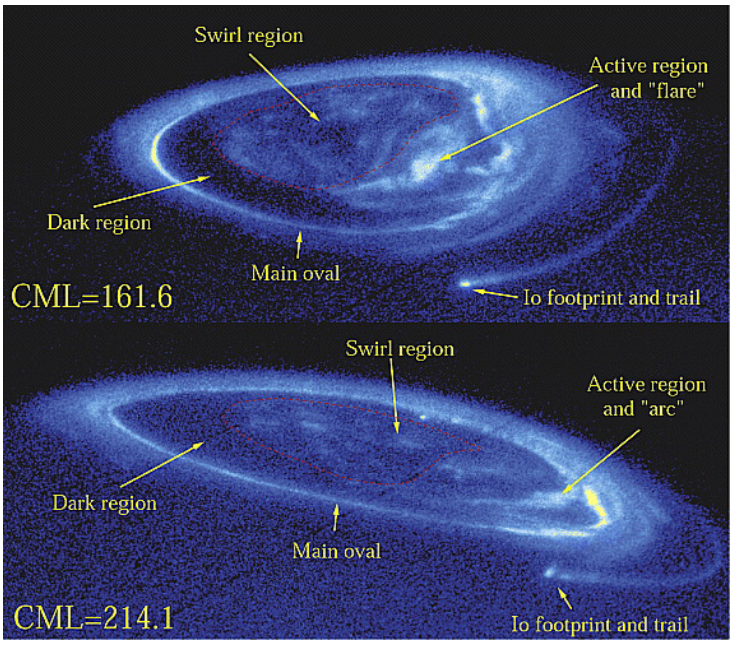

Figure 2.7: On December 14, 2000, Hubble Space Telescope Imaging Spectrograph (STIS) images revealed recurring auroral activity in Jupiter's northern region, including the main oval, the Io footprint, and its trail, and other emissions poleward of the main oval, referred to as the polar aurora. The upper image had a Central Meridian Longitude (CML) of $161.6°$, while the lower image had a CML of $214.1°$. The differences between the images demonstrate typical polar emission fluctuations in 1.5 hours. Additionally, the arrows outline the swirl, the active, and the dark region (Grodent, Clarke, Waite, et al., 2003).

Recent research has demonstrated that most of the polar cap region is filled with magnetic flux confined to the planet, while only a thin crescent-shaped flux area is exposed to the solar wind (Zhang et al., 2021). This is due to the slow reconnection rates at the magnetopause in comparison to the timescale of planetary rotation, which limits the amount of magnetic flux that can be open (Delamere & Bagenal, 2010; Masters, 2017, 2018; McComas & Cowley, 2007). Observations of ion conics have revealed a cone-like pitch angle shape following the conservation of the first adiabatic invariant. Anisotropic

electron distributions generate waves that heat the ions until they reach a critical energy, allowing them to escape and move along magnetic field lines into the magnetosphere (Clark et al., 2018; Szalay et al., 2018). The ions are initially trapped along the magnetic field lines, so even in Jupiter's polar cap region, magnetic structures must be enclosed.

The polar cap showed broad spatial regions with narrow electrostatic potentials in the megavolt range throughout 80% of the polar crossings (Mauk, Haggerty, Paranicas, et al., 2017b; Paranicas et al., 2018). These electrostatic potentials follow mainly from the observation of persistent, strongly field-aligned, downward-going heavy ions and mostly upward-going energetic electrons, both with inverted V and broadband distributions (Ebert et al., 2017; Elliott, Gurnett, Kurth, Clark, et al., 2018; Mauk et al., 2020; Paranicas et al., 2018).

Intense precipitating heavy ions with energies greater than 10 MeV were observed over the polar cap. They were insufficient to explain the intense polar x-ray emissions observed since the first Juno flyby (Haggerty et al., 2017). A comprehensive study of several instruments has shown that intense X-rays correlate with electromagnetic ion cyclotron (EMIC) waves, observed similarly to those seen on Earth. Yao et al. (2021) reveals an intriguing chain of events, beginning with compression, which sets off EMIC waves, ions traveling along magnetic fields, and culminating in pulsating x-ray auroras.

2.3.3 Solar Emissions

The planet's rotation mainly influences Jupiter's main aurora, but the pressure from the solar wind causes the planet's magnetosphere to have an asymmetric shape. The internal magnetic field of the planet interacts with the solar wind, leading to the formation of a bow shock and a magnetopause. This magnetopause stretches from $63\,R_J$ to $92\,R_J$ in the direction of the Sun. Specifically, the effects of the solar wind on Jupiter create a noon-midnight asymmetry, with compression on the day side and an extended tail on the night side. Additionally, there is a dawn/dusk asymmetry in Jupiter's magnetosphere due to solar wind pressure, leading to diurnal variations in its dynamics. Hot plasma further inflates the magnetosphere, making it more extensive and more compressible than a simple magnetic dipole (Joy, 2002; Thomas et al., 2004). Beyond a distance of 15 Jupiter radii, the thermal pressure of the charged particles exceeds the local magnetic field pressure by a factor of $\beta = 100$ at 45 R_J (Mauk, 2004). Eventually, centrifugal forces cause the disconnection of the plasma, forming plasmoids ejected down the tail (Kronberg et al., 2008; Vogt et al., 2014; Blöcker et al., 2022). It has been shown from several studies that the intensity of the main emission zone is anti-correlation to the solar wind dynamic pressure (Cowley & Bunce, 2001; Clarke et al., 2009; Kivelson et al., 2001; Baron et al., 1996; Connerney et al., 1996; Nichols et al., 2017; Pryor et al., 2005; Sinclair et al., 2019; Yao et al., 2019, 2022). Additionally, an asymmetry is visible between the dawn and dusk

sides of the northern aurora, with the dusk side exhibiting more diffuse emissions and the dawn side displaying narrow arcs (Gérard et al., 1994a). Studies of the first 20 perijoves by the Juno UVS have shown dawn storm events among the brightest auroral displays as small, fleeting spots evolve into a luminous arc, eventually dividing into two arcs with a central empty region. Subsequently, these arcs transform into patches of auroral emissions moving toward the equator, accompanied by signatures of plasma injection (Bonfond et al., 2021). Some dawn storms remain faint, while others occur consecutively within a short time.

In conclusion, the auroras of Jupiter are formed by a combination of factors, including the planet's rotation, the pressure of the solar wind, and the innermost Galilean moons.

2.3.4 Satellite Footprints

The footprint auroral emissions result from complex interactions between Jupiter's magnetosphere, moons (Io, Europa, and Ganymede), and surrounding plasma. The magnetospheric plasma interaction with these moons generates Alfvén waves, which travel along Jupiter's magnetic field toward the planet (Kivelson et al., 2004; Saur, 2004). These waves trigger radio emissions and bombard Jupiter's atmosphere, leading to bright auroral spots (Hess et al., 2008). The conductive ionosphere of Io allows electric currents to flow between the ionosphere of Jupiter and Io, resulting in auroral emissions on Jupiter. The interplay between Io, Jupiter's magnetic field, and the plasma torus surrounding Jupiter creates various auroral features, with different populations of protons and heavy ions observed at high latitudes with JADE (Szalay et al., 2017). Janser et al. (2022) presented evidence that small-scale magnetic field fluctuations in the Io flux tube can cause turbulence in the $0.2 - 800$ Hz frequency range associated with Doppler-shifted spatial variations. The interaction also leads to proton acceleration as a result of wave-particle interactions, generating energetic outflowing protons. Similar phenomena have been observed in the footprints of Ganymede and Europa and its associated flux tubes, showing the complexities of Jupiter's auroral processes (Rabia et al., 2023; Mauk et al., 2022).

CHAPTER 3

PART I: ELECTRON PRECIPITATION BUDGET IN THE JOVIAN AURORA

In this chapter, a comprehensive analysis derived within the doctoral research study is presented, where we investigated the electron distributions contributing to Jupiter's auroras based on data from the Juno spacecraft. The study, titled "Jovian auroral electron precipitation budget - A Statistical Analysis of Diffuse, Mono-energetic, and Broadband Auroral electron distributions", was previously published in the Journal of Geophysical Research: Space Physics. This paper is included in my doctoral dissertation and was published in Salveter et al. (2022). This chapter displays the paper Salveter et al. (2022), which examines Jupiter's auroral electron precipitation budget using data from Juno's first 20 perijoves. Section 3.2 explains how electron distributions were classified to identify acceleration mechanisms. Section 3.3 reveals that dominant broadband energy distributions support the dominance of stochastic acceleration processes driving strong auroral emissions. Section 3.4 discusses the findings in terms of aurora generation processes and associated acceleration mechanisms. The work of Salveter et al. (2022) was based on individual investigations of Juno observations, which were supplied by the JEDI science team, George Clark and Barry H. Mauk from the Johns Hopkins University Applied Physics Laboratory in Laurel, Maryland, USA, and supervised by Joachim Saur from the Institute of Geophysics and Meteorology at the University of Cologne in Cologne, Germany.

Keypoints

- We present a statistical study of Jupiter's auroral electrons within 30 keV to 1200 keV based on Juno's first 20 perijoves
- Broadband electron distributions dominates Jupiter's main auroral zone as they are observed in $93\% \pm 3\%$ of the intervals studied here.
- Dominance of broadband distributions underlines the importance of a turbulent or stochastic acceleration process

Abstract

Recent observations by the Juno spacecraft have shown that electrons contributing to Jupiter's main auroral emission appear to be frequently characterized by broadband electron distributions, but also less often mono-energetic electron distributions are observed as well. In this work, we quantitatively derive the occurrence rates of the various electron distributions contributing to Jupiter's aurora. We perform a statistical analysis of electrons measured by the JEDI-instrument within $30 - 1200$ keV from Juno's first 20 orbits. We determine the electron distributions, either pancake, field-aligned, mono-energetic, or broadband, through energy and pitch angles to associate various acceleration mechanisms. The statistical analysis shows that field-aligned accelerated electrons at magnetic latitudes greater than 76° are observed in $87.6\% \pm 7.2\%$ of the intervals time averaged over the dipole L-shells according the main oval. Pancake distributions, indicating diffuse aurora, are prominent at smaller magnetic latitudes ($< 76°$) with an occurrence rate of $86.2\% \pm 9.6\%$. Within the field-aligned electron distributions, we see broadband distributions $93.0\% \pm 3.8\%$ of the time and a small fraction of isolated mono-energetic distribution structures $7.0\% \pm 3.8\%$ of the time. Furthermore, these occurrence statistics coincide with the findings from our energy flux statistics regarding the electron distributions. Occurrence rates thus also characterize the overall energetics of the different distribution types. This study indicates that stochastic acceleration is dominating the auroral processes in contrast to Earth where the discrete aurora is dominating.

Plain Language Summary

With the Juno spacecraft arriving in the magnetosphere of Jupiter, first flyby particle measurements have changed the knowledge about the developing process of Jupiter's intense aurora. The observations of auroral particles show a stochastic behavior rather than a preference for specific energy. Our statistical analysis of the first 20 flybys at Jupiter compares the occurrence of different particle distributions and highlights the importance of different generation theories for Jupiter's aurora. A generation via stochastic rather than mono-energetic behavior is deduced and supports previous observations.

3.1 Introduction

Jupiter's aurora is powered by a very unique magnetospheric environment strongly differing from the magnetosphere of Earth. The magnetosphere of Jupiter is mainly dominated by the planet's high rotation rate, strong magnetic field, and mass source Io, which ejects approximately 1 ton/s of plasma into the middle magnetosphere, rather than from a solar wind interaction (Bagenal & Delamere, 2011). However, expectations on auroral mechanisms were initially drawn from analogies with Earth, supported by remote optical observations of Jupiter's aurora (Clarke et al., 2002; Mauk et al., 2002; Grodent et al., 2018; C. Tao et al., 2015; Kimura et al., 2015) and equatorial in-situ measurements from the Galileo spacecraft and flyby missions such as the Voyagers (Bagenal et al., 2017). The Juno spacecraft – a Jupiter polar-orbiting mission launched in 2011 (Bolton et al., 2017) – has fundamentally changed our view of the Jovian aurora with the first-ever high-latitude in-situ measurements.

The dynamic of the magnetosphere is driven by the high rotation rate of Jupiter. The plasma sourced primarily by Io is picked up and accelerated to corotation speeds; however, corotation can not be sustained at large distances. The radially outward moving plasma drives a current system associated with the breakdown of corotation that diverges and closes within the auroral ionosphere (Cowley & Bunce, 2001; Hill, 2001, 1979).

Knight (1973) introduced the theory of electric potentials along with the static current system to maintain the current density within the magnetosphere-ionosphere coupling, especially in low density regions at high latitudes. Knight (1973) formulated a relation of the current density to the field-aligned potential, which accelerates particles to a specific energy. The acceleration process is therefore described as an electrostatic process, causing mono-energetic electron distributions. Standard particle calculations prior to the Juno mission were based on the Knight formula (Cowley & Bunce, 2001; Nichols & Cowley, 2004; Ray et al., 2010).

The radial particle transport in the current sheet additionally causes small-scale magnetic field perturbations (Mauk & Saur, 2007; Saur et al., 2003; C. Tao et al., 2015) as a consequence of discontinuous flux tube-driven transport. It is argued that local deviations of the force or stress balance of Jupiter's magnetosphere - ionosphere coupling cause small-scale magnetic field fluctuations to achieve stress-balance (Saur et al., 2018). These magnetic field perturbations then cascade to smaller scales as they are counter-interacting along magnetic field lines. When reaching the kinetic length and temporal scales, wave-particle interaction converts electromagnetic energy in the wave fields into particle energy. The processes can be summarized as locally stressed magnetic field lines. Stressed magnetic field lines lead to Alfvén waves, which transfer momentum between the magnetosphere and the ionosphere, causing stochastic acceleration (Saur et al., 2018).

Both the large-scale electric current systems, as well as the small-scale magnetic

field stresses, maximize in the middle magnetosphere, ranging from 15 to 20 R_J up to approximately 50 R_J (Hill, 2001; Cowley & Bunce, 2001; Saur et al., 2018), and contribute to the main emission zone. Other regions such as the polar cap, here defined as the region poleward of the main emission zone, and satellite footprints are therefore not investigated. Magnetospheric processes in the middle magnetosphere are the root cause of the acceleration process of auroral particles, where the acceleration of particles is crucial to overcome magnetic mirroring forces to generate aurora. All acceleration processes, e.g. stochastic and electrostatic, contribute to different electron energy distributions, which are well observed by the Juno spacecraft with the JEDI at high electron energies (25 keV−1200 keV) (Mauk, Haggerty, Jaskulek, et al., 2017) and JADE at low electron energies (100 eV−100 keV) (McComas et al., 2017) (for more information on Juno see Bagenal et al., 2017).

Early observation of electrons along magnetic field lines connecting to the auroral regions by JEDI showed that the electron energy spectra are broadband, not structured in energy, and with a shallow slope (i.e. hard) extending beyond $\approx$ 800 keV (Mauk, Haggerty, Paranicas, et al., 2017a; Allegrini et al., 2017). Regions with upward loss cones indicate diffuse aurora, either seen by UVS, JEDI and JADE (Allegrini et al., 2017; Li et al., 2017). Additionally, no large magnetic perturbations ($\leq 1\%$) due to field-aligned currents associated with the auroral zones were observed, suggesting no potential drops as the primary auroral driver (Connerney et al., 2017; Kotsiaros et al., 2019). Later measurements then observed isolated mono-energetic distributions from 1.4 to 2.9 R_J associated with electric potentials up to 400 keV, but still with less energy flux than from stochastic characteristics (Mauk, Haggerty, Paranicas, et al., 2017b; Ebert et al., 2017; Clark, Mauk, Haggerty, et al., 2017). Several other mono-energetic distributions over the main emission zone have been observed, but the most intense auroras with high energy flux are still generated by stochastic processes (Mauk, Haggerty, Paranicas, et al., 2017a). The observations indicate no evidence for one clear assignable acceleration process, rather a composition or even a transition between broadband and mono-energetic distributions (Mauk et al., 2018).

Comparison with other Juno instruments has shown similar conclusions, as by comparison with UVS images. Gérard et al. (2019) concluded observed polar emissions are even more than an order of magnitude brighter than expected from downward energy flux calculations. However, upward energy flux calculations show sufficient energy flux, indicating a bidirectional broadband electron acceleration below Juno's altitude (Ebert et al., 2019). Upgoing electron beams also showed evidence of whistler-mode wave emission driven by downward electric potentials, but mainly within the polar cap (Tetrick et al., 2017; Elliott, Gurnett, Kurth, Clark, et al., 2018; Elliott, Gurnett, Kurth, Mauk, et al., 2018). A comparison of main aurora particle features and plasma waves that accompany the features is diagnosed with the Waves instrument by Kurth et al. (2018), where the

importance of whistler waves, as well as Alfvén waves, is highlighted. A separation of the auroral zones has been accomplished by Mauk et al. (2020), where three distinct zones are introduced, DifA, ZI, and ZII. The DifA primarily shows empty loss cones, with a small enhancement of energy flux in the downward rather than in the upward direction. Zone ZI and ZII are classified by filled loss cones, respectively, in either downward or upward direction, characterized by a dominating energy flux within the loss cones (Mauk et al., 2020). The two Zones, ZI and ZII, are associated with upward and downward currents, where both Zones are dominated by broadband distributions with some mono-energetic features.

In the case of Earth's aurora, mono-energetic electrons contribute a larger energy flux than broadband accelerated electrons (Newell et al., 2009). In contrast, Juno's observations reveal that broadband statistically accelerated electrons may be dominant for Jupiter's aurora (Mauk, Haggerty, Paranicas, et al., 2017a) and might play an important role in Saturn's magnetosphere as well (Saur et al., 2006). What has been missing so far is a quantitative study statistically analyzing the occurrence rates to quantify the contribution of different energy distributions and associated acceleration processes to the Jovian aurora. Such a study is now possible for Jupiter as the Juno mission acquired sufficient observation to perform a statistical analysis. Our study compares the occurrence of different auroral precipitation types such as diffuse, mono-energetic, and broadband aurora to investigate the occurrence of filamentation as a driving part for particle acceleration. Properties such as particle distributions and energy fluxes are used to classify regions into the corresponding precipitation types, as introduced by Mauk et al. (2020). This statistical study is based on the times when Juno's location magnetically maps to the main emission zones. We omit auroral processes in the polar cap and satellite regions. Several conditions to the time windows selection are therefore introduced in the section 3.2, followed by the classification of precipitation types based on Mauk et al. (2020).

3.2 Data and Classification Scheme

In-situ observations of electron and ion distributions with the Juno spacecraft are performed by JEDI and its complement at lower energies, JADE (Bagenal et al., 2017, for more information on Juno). In the following JEDI data will be used to investigate the precipitation of energetic electrons within an energy range from 25 keV to 1200 keV (Mauk, 2013). The JEDI instruments consist of 18 SSDs to measure single electron rates in different look directions at the same time. Six SSDs are arranged in a 160° fan for each of three instruments, together covering a nearly 360° field of view (Mauk, 2013). To characterize the acceleration process, we organize the electrons as a function of local pitch angle – the angle between the particle velocity and magnetic field vector measured by Juno's magnetometer (Connerney et al., 2017). The instrument's alignment with the

spacecraft plane allows full pitch angle coverage when the magnetic field line is contained within the plane roughly perpendicular to the spacecraft spin vector. In section 3.2.4 we will introduce a condition for reasonable data selection based on good pitch angle coverage. The SSDs measure for 0.25s every 0.5s. Even small structures of a few hundred kilometers are resolvable, because the spacecraft velocity is ≈ 50 km/s near Jupiter. JEDI's pitch angle coverage is decimated as Juno's orbit evolves and relies more on the S180 sensor that is mounted perpendicular to Juno's spin plane. The consequence is that instead of near instantaneous pitch angle coverage in the earlier orbits, full pitch angle coverage is built up over the 30 s spacecraft spin period. The smallest resolvable size close to Jupiter is then approximately 1500 km, broader than many auroral features. The statistical study is confined to the first 20 perijoves. Good pitch angle coverage will be additionally tested based on comparison to the local loss cone size, as further described in section 3.2.4, with the loss cone size defined as shown in section 3.2.3.

The observed electron counts need to be rigorously evaluated on signal to noise ratio, as electrons can scatter on foils, grids, and other internal surfaces and stimulate unintended SSDs as further described in section 3.2.5. The resulting adequately resolved times are processed by a classification in precipitation types considering the electron pitch angle and energy distributions, as further explained in section 3.2.6.

3.2.1 Emission Zone

The subject of our investigation of auroral acceleration mechanisms is the main emission zone. The observation of associated precipitating auroral electrons is restricted to small radial distances and along magnetic field-lines mapping to the main emission zone. To ensure the observation of accelerated particles, the spacecraft needs to be below expected heights of acceleration and within a radial distance where the geometric loss cone is large enough that the loss cone distribution is resolved by JEDI's angular field of view (Clark et al., 2018). We, therefore, select the data by a radial distance of 1.2 to 2.5 R_J (Ebert et al., 2017; Clark et al., 2018). We assume the shape of Jupiter to be a sphere with a radius of 71492 km as the JPL navigation team proposes throughout all Juno activities (Bagenal et al., 2017). Note that the polar radius of Jupiter is much less (66854 km) because of the high rotation rate of the planet, described by a flattening of 1/15.4 of Jupiter's surface (Bagenal et al., 2017). Furthermore, the spacecraft footprint in the atmosphere should locate in the expected zones of main auroral emission. The mapping from the spacecraft onto the atmosphere can be processed by the combination of the JRM09 (Connerney et al., 2018) with the current sheet model (CAN)(Connerney et al., 1981).

To describe the position of the Juno measurements the M-shell model (JRM09 and current sheet model) has been used in the literature with M-shells which range up to 100. However, the current sheet model is defined only within 5 to 50 R_J and thus cannot be

used for values larger than 50, where it leads to spurious values (see Text S1). Since the purpose of this paper is not the mapping of the observed electrons into the magnetosphere, but a characterization of the electrons near Jupiter, we use coordinates which are as model-independent as possible. We will therefore use magnetic latitude θ_M, which is additionally related to L-shell. However, we point out that L-shell does not provide an accurate mapping into the equatorial region of Jupiter's magnetosphere in particular for large distance starting at 20 to 30 R_J. Therefore we will use in this work magnetic latitude as the primary coordinate to describe the position of the measurements and will show in addition the L-shell value as a lower limit for the real L-shell crossing. We will use the dipole L-shell boundaries from 8 to 50 R_J to include observations mapping to the HST main auroral oval (Bonfond et al., 2012), as shown in Figure 3.1.

3.2.2 L and M-shell Parameter

Note: This subsection is from the supplementary material of the published paper for ease of reading.

The choice of the coordinate system to compare properties perpendicular to the main auroral emission zone of Jupiter is important. We therefore investigate the different available parameters and especially compare the dipolar magnetic model with the multipolar magnetic field model adjusted by the current sheet model (CAN) introduced by Connerney et al. (1981). The underlying magnetic model, the Juno Reference Model through Perijove 9 (JRM09), was introduced by Connerney et al. (2018). Both models, dipole and multipole, can be used to define auroral properties for magnetic field lines mapping to equal equatorial crossing distances, expressed by the dipole L-shell parameter (Dipolar moment of JRM09) and the M-shell parameter (higher moments of JRM09 + CAN). The parameters are displayed in Figure 3.1 for all Juno spacecraft positions during the first 20 perijoves.

The ratio of the L-shell and M-shell L/M is not unique, especially for equatorial mapping distances greater than 10 R_J. The colors of the data points in Figure 3.1 scale with the radial distance of the spacecraft to Jupiter and indicate the dependency of the ratio L/M on the radial distance. For the spacecraft positions in the direct vicinity to Jupiter $R < 4$, the ratio L/M is highly variable, which is due to the high influence of higher magnetic moments on the magnetic field line topology for small radial distances. Measurements at larger radial distances show a ratio between L and M with a strong kink arising at $M = 50$ R_J which coincides with the current sheet model (CAN) outer boundary. In Figure 3.1 we can see this kink at $M = 50$ R_J with a stronger rise in M-shell with L-shell compared to the region inside the CAN boundaries between 5 R_J and 50 R_J. The M-shell parameter thus does not yield reliable parameters, especially around the M-shell parameter 50 R_J.

The mapping of the magnetic field lines onto the Jovian atmospheres shows that the

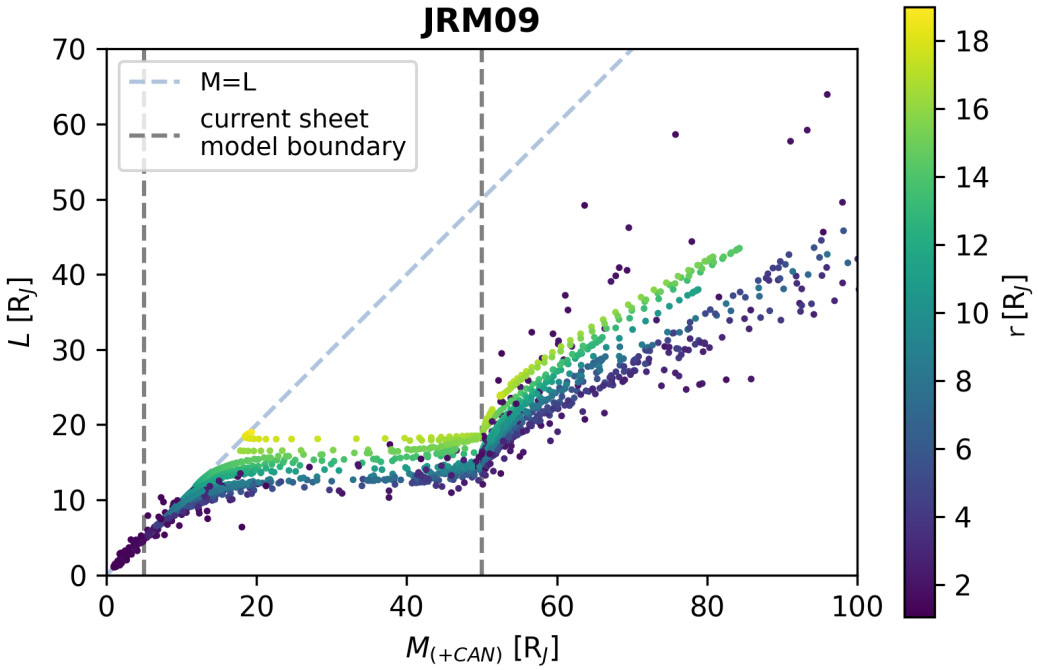

Figure 3.1: Ratio of JRM09 dipole L-shell parameter L to the JRM09 + Con81 M-shell parameter M for all Juno positions during the first 20 perijoves. The datapoints are colored by the radial distance r from the center of Jupiter in R_J. The grey lines show the radial boundaries of the current sheet model (CAN). The blue lines displayes **the ratio of one, thus where** L-shell equals M-shell.

magnetic field lines corresponding to an M-shell parameter of 50 locate into the main emission zone and thus near the kink, too. Figure 3.2 shows exemplary the fourth perijove, where the region of main interest maps to an M-shell parameter of $R = 50$ R_J, and thus to the kink. Both models do not seem to provide an adequate mapping into the equator because L-shell neglects the current sheet effects and M-shell leads to spurious effects for M-shells values around and larger than 50.

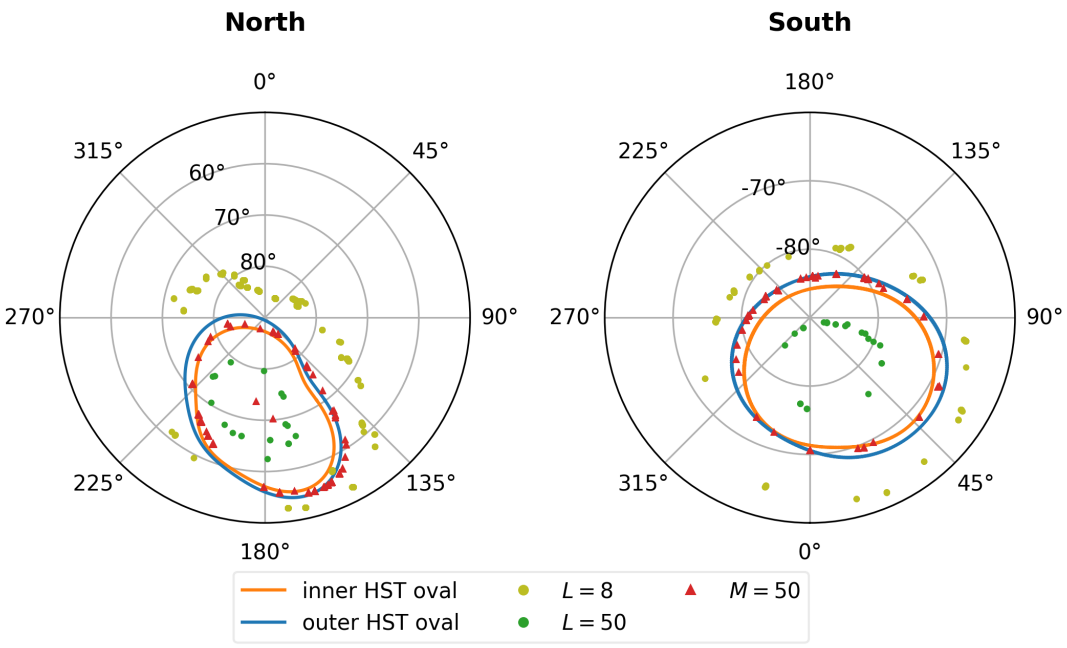

Figure 3.2: Dipole L-shell parameter (JRM09) of 8 and 50, as well as the M-shell parameter (JRM09 + Con81) 50 at the atmosphere in Jupiter System III coordinates (SysIII) West longitude and latitude. The parameters are mapped from Juno's position of the first 20 perijoves onto the atmosphere using the JRM09 and Con81. The orange and blue lines mark the boundary of the mean Hubble Space Telescope oval Bonfond et al. (2012).

3.2.3 Loss Cone Calculations

High energy particles precipitate into the atmosphere to excite atoms generating auroral emission. This is possible when the relation of parallel velocity to orthogonal velocity, in the frame of the magnetic field lines, is sufficiently large to overcome mirroring forces arising from the invariant magnetic moment, constant energy of motion, and converging magnetic field lines (Baumjohann & Treumann, 1996). Those precipitating particles, therefore, possess a smaller PA than the maximal angle of α_c the loss cone (LC) angle. All particles inside the loss cone therefore contribute to the precipitating particles generating discrete aurora. Particles outside of the loss cone cannot overcome mirroring forces and are trapped above the atmosphere, bouncing between both hemispheres.

The definition of the loss cone

$$\alpha = \sin^{-1}\left(\sqrt{\frac{B_{sc}}{B_{atm}}}\right) \tag{3.2.1}$$

depends on the relation of magnetic field strength at the spacecraft B_{sc} and the magnetic field strength at the atmosphere B_{atm} (Baumjohann & Treumann, 1996). The magnetic field strength at the spacecraft is measured with the onboard fluxgate magnetometer. The magnetic field strength of Juno's footprint at the atmosphere is primarily computed using the JRM09 (Connerney et al., 2018) taking the high influence of the higher magnetic

moments at small radial distances into account, as well as using the current sheet model (Connerney et al., 1981) whose influence is negligibly small at small radial distances. The top atmospheric layer, the exosphere, does not have a specific upper boundary, but several studies and models suggest an upper boundary of $\sim$ 400 km above the 1 bar level (Gérard et al., 2014; Seiff et al., 1998), where the 1 bar level is computed as the dynamically flattened (1/15.4) surface of Jupiter (Connerney et al., 2018).

3.2.4 Pitch Angle Coverage

The resolution of the loss cone strongly depends on the pitch angle coverage which is mostly sufficient when the spacecraft rotation axis is nearly perpendicular to the magnetic field line. Restrictions to the mounting of the sensors and the alignment of the spacecraft cannot provide the full field-aligned pitch angular coverage to 0° and 180°. For some times the maximal and minimal covered pitch angle from all detectors does not reach into the loss cone. A sufficient loss cone coverage is thus provided when these boundary pitch angles lie within the identified loss cone from section 3.2.3. To neglect the temporal influence of the spacecraft spin, we calculate the mean of the pitch angle boundary with a rolling window of 30 s width corresponding to the spacecraft spin period. This ensures that the spacecraft orientation provides at least a loss cone coverage over at least 50% of the time interval.

3.2.5 Signal to Noise

We only address times when a sufficient amount of electron counts has been observed and an appropriate signal-to-noise ratio is obtained. The electron counts are measured by the SSDs which detect particles coming through the sensor head over a predefined time interval. As the detectors measure finite numbers of counts over finite time intervals, the uncertainties or the noise arises from the independence of the events, rather than from a lack of precision in the measuring instrument (Bevington et al., 1993; Mauk, 2013). We therefore consider the measurements as Poisson-distributed events with the associated statistical uncertainties. If the counts per accumulation are small, then they might not contribute to a sufficient signal to noise ratio (SNR) and thus cannot be used to derive auroral fluxes. Relative uncertainties of Poisson-distributed counts are high when count rates are small, described by the signal-to-noise ratio $SNR = \sqrt{N}$, with N counts in the time interval Δt (Bevington et al., 1993). To neglect weak intensity regions from statistics, we only address times with a signal-to-noise ratio of at least 3, resembling a relative error of 33%, and a measurement of at least 9 counts for the mean of one energy channel. This threshold works fine with by-eye-inspections as shown in Figure 3.3, where the low intensity region after 13:40:30, panel B, has an insufficient SNR to be considered as signal (orange beam in panel A). The threshold has shown that all important features

as known from previous main emission observations (e.g., Mauk, Haggerty, Paranicas, et al., 2017a; Clark, Mauk, Paranicas, et al., 2017) has been included. Figure 3.3 shows a flyby over the northern polar region during Juno's fourth perijove, where the orange bar within part A of the figure marks regions with sufficient SNR including all significant beam structures as observed in the energy (part B) and pitch angle (part E) spectra.

3.2.6 Classification

The classification of types of electron distributions is processed by two steps. The first step is used to distinguish between field-aligned and trapped particles by considering pitch angle distributions, as described in 3.2.6. The second step is used to distinguish between mono-energetic and broadband distributions, by observing the intensity-energy spectra on broadband and mono-energetic structures, as described in 3.2.6. The two-step classification is applied to time intervals chosen under the conditions summarized in previous subsections.

Pancake and Field-Aligned Distributions

Plasma particles contributing to the aurora are characterized by field-aligned motion, confined to the downward loss cone. Hence, particles within field-aligned distributions can precipitate into the atmosphere and generate aurora. Pancake distributions correspond to a dominant fraction of particles outside of the loss cone, which are not likely to precipitate into the atmosphere. Trapped particles can be scattered back into the loss cone and contribute to diffuse aurora, an unstructured and semi-permanent type of aurora. The diffuse aurora mainly results from wave-induced scattering processes, whereas discrete aurora results from particle acceleration along the magnetic field-lines at low-altitudes, showing sharply defined and time-variable structures (Ni et al., 2016; Mauk & Bagenal, 2012).

To determine the corresponding distributions for each timestep, we compare energy fluxes inside the loss cone, for upward or downward direction, with the energy flux outside of the loss cones, as introduced by Mauk et al. (2020). We filter the intensities for every sensor by the corresponding pitch angles and perform the sum

$$\pi \cdot \sum_{n} I_n(\alpha)\ E_n \cdot \Delta E \tag{3.2.2}$$

where n stands for each energy channel, E_n is the central energy of the channel, ΔE_n is the energy bandpass of the channel, and I_n is the measured Intensity of the channel n (Mauk, Haggerty, Paranicas, et al., 2017a). The projection of the loss cone onto the atmosphere with the area-projection-weighted size π is applied while assuming that the loss cone is fully populated. The resulting fluxes correspond to the energy fluxes at Jupiter's surface if

we assume that there is no retarding electron potential comparable to the energies involved (Mauk, Haggerty, Paranicas, et al., 2017a). The electron population outside of the loss cone does not reach the atmosphere. The one-directional energy flux at spacecraft altitude is given by the same expression as in (3.2.2) under the assumption that the loss cone angle $\alpha_L \ll \pi/2$. At spacecraft altitude the local one-directional energy flux within the loss cone and outside of the loss cone scale by $\tan^2 \alpha_L$ for similar intensities inside and outside of α_L. In this work, we compare the downward going energy fluxes at the surface of Jupiter, which is responsible for the aurora, and the energy fluxes outside of the loss cone at spacecraft altitude and therefore use (3.2.2) in both cases.

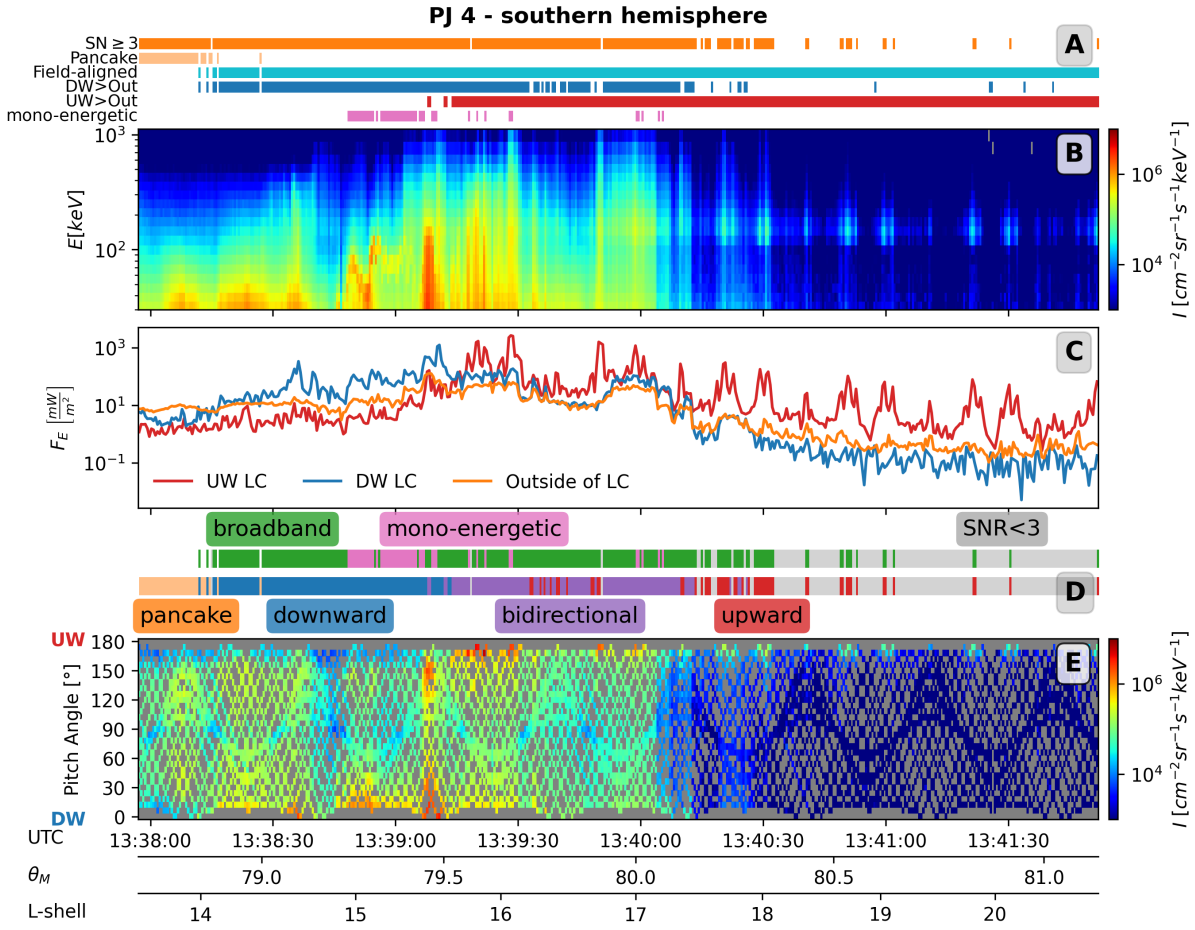

Figure 3.3: Classification of Juno's fourth southern hemispheric flyby over the main emission zone. **B** and **E** show energy-time and pitch angle-time spectrograms of intensities, respectively, measured by the JEDI instrument. The "speckled" pattern of the pitch angle distribution results from incomplete pitch angle coverage, where the grey color corresponds to absent measurements. The energy flux calculated by equation 3.2.2 is shown in **C** for the upward (UW) and downward (DW) loss cone, as well as outside of the loss cone (Out). **A** shows color-coded the status of the applied criteria tagged on the left side and **D** shows the resulting classification into the type of the energy distribution, broadband (green) or mono-energetic (pink), and the various types of pitch angle distributions, pancake (orange), downward (blue), bidirectional (purple), and upward (red). The JRM09 L-shell, and the corresponding magnetic latitude at $r = \mathrm{R}_J$ are also provided.

The resulting energy fluxes are shown in Figure 3.3C for Juno's fourth perijove. The different regions dominated by downward or upward energy flux are shown in part A of Figure 3.3. Pancake distributions are recognized in regions where neither the downward or upward energy flux are greater than outside of the loss cones, as defined by Mauk et al. (2020). All other times, when neither the downward nor the upward energy flux is greater than outside the loss cone, are defined as field-aligned distributions. The classification scheme is applied to every timestamp of the raw data with the highest temporal resolution of 0.5 s. The results from the classification are shown in Figure 3.3D with pancake or field-aligned distributions, where the field-aligned distributions are subdivided into mono-energetic and broadband distributions, as further described in 3.2.6. Field-aligned distributions are furthermore subdivided in upward, downward, and bidirectional regions, where either the upward or downward energy flux is greater than outside of the loss cones or both directions are greater resulting in a bidirectional distribution. Additionally, Zone I and Zone II as introduced by (Mauk et al., 2020), are classified corresponding to either region of dominating downward or upward energy flux, respectively.

Broad and Mono-energetic Energy Distributions

Field-aligned particles show enhanced energy fluxes within at least one loss cone direction, upward and downward, and thus show evidence of highly energetic or dense particle distribution contributing to a specific acceleration process. The signatures of electrostatic and stochastic acceleration are used to define the respective classification into broadband and mono-energetic structures for each timestep's energy distribution. Broadband structures show a long tail in the energy distribution with strong intensities even exceeding into high energies. Broadband distributions can be similar to kappa distributions, which are based on Maxwellian distributions but provide a high-velocity tail with a power-law distribution (Baumjohann & Treumann, 1996). A typical broadband distribution is shown in Figure 3.4A for a selected timestamp of Juno's fourth southern perijove. The energy spectrum is limited to the measuring range of JEDI and the efficiency of the channels. However, distinct from a broadband distribution is the continuous decrease of the intensities with high energies. The rising intensities with increasing energy at low energies result from increasing efficiencies within each channel that are not yet accounted for in the calibration process, as marked by "Uncal" in Figure 3.4. The channels are properly calibrated above 30 keV. Low energy channels are thus excluded from the energy distribution classification. Channels between 130 keV and 270 keV, as marked by "Pen" in Figure 3.4, are additionally excluded due to the minimum ionizing effect of very high energetic electrons. Electrons in the MeV-class can fully penetrate the SSDs and leave a fraction of their full energy behind. This minimum ionizing energy for 0.5 mm SSDs at JEDI peaks at 160 keV (Mauk et al., 2018, supporting material Text S1). Enhanced intensities around this minimum ionizing energy indicate very energetic electron distributions extending into mega electron

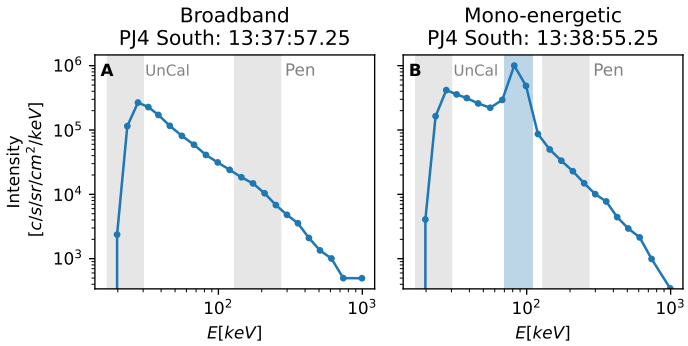

Figure 3.4: Example energy spectra for two selected times of Juno's fourth perijove in the southern hemisphere. **A** shows a typical broadband distribution, **B** shows a mono-energetic distribution with a peak around 100 keV, marked by the blue zone. Peaks within the grey zone marked by "pen" for penetration would indicate high electron energies of $>$ 10 MeV penetrating the sensor head and leaving behind contamination at roughly 160 keV by secondary electrons. The grey zone marked as "Uncal" is yet not accounted for with the calibration process of the efficiencies.

volt ranges and do not contribute to the electron's energy distribution. Intensities within remaining energy channels need to decrease continuously with increasing energy to define regions with broadband acceleration, where the mean intensity from all solid state detectors is used.

The determination of mono-energetic structures with JEDI are limited by the observable energy range, the altitude of Juno's flyby as well as the impact of penetrating particles on the electron distribution. Penetrating particles can leave behind high intensities similar to mono-energetic structures but mark highly energetic particles outside of the JEDI measuring range. But energy distributions with a high impact by highly energetic particles penetrating into the detector are not expected to show inverted-V structures in the JEDI energy range, as Mauk et al. (2018, Supporting Information S1) stated that energy distributions with mono-energetic structures observed by JEDI are rarely accompanied by a minimum ionizing peak due to a high energy tail.

However, we define an energy distribution as a mono-energetic distribution when at least one energy channel, outside of the minimum ionizing energy range, peaks in intensity throughout the monotonically decreasing spectra. To neglect the impact of noise on the distribution classification, the enhancement needs to occur in both intensities and counts. The intensity enhancement is thereby not restricted, but the counts need to increase by at least 9 counts to reduce the influence of noise, as further described in section 3.2.5. An underestimation of mono-energetic structures might arise, as downward accelerated electrons from potentials below the spacecraft cannot be observed, but are expected, as deduced from upward accelerated protons (Szalay et al., 2021).

The energy distributions are summed over all SSDs and thus all pitch angles. A further classification can also be accomplished by filtering the intensities for the upward and

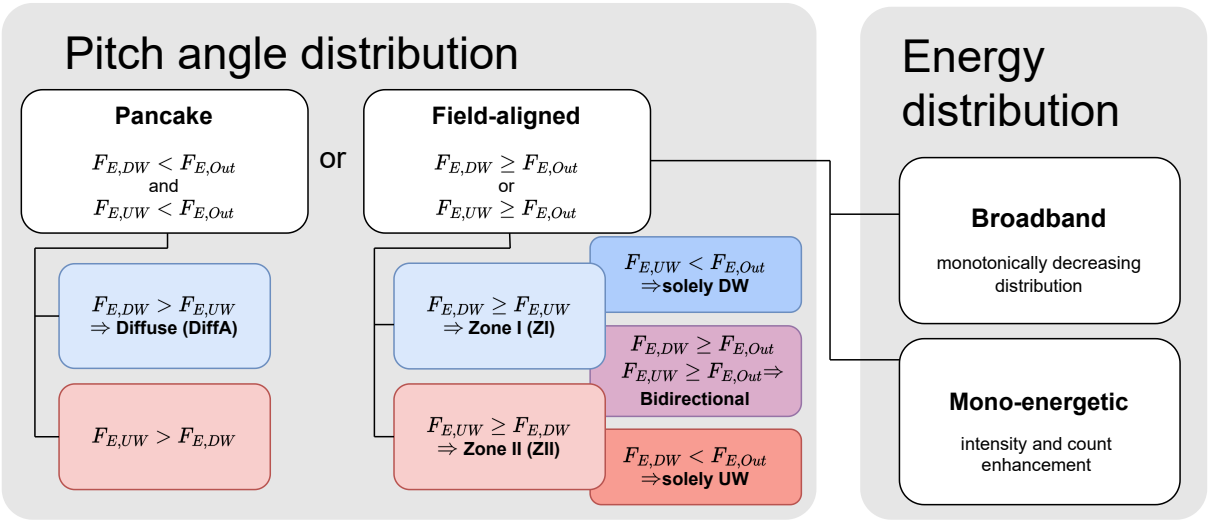

Figure 3.5: Classification scheme based on pitch angle and energy distribution analysis. The classification is based on energy flux F_E comparisons for electrons outside the loss cone (Out) and electrons inside the loss cone, either in the upward (UW) or downward (DW) direction.

downward loss cone and outside of the loss cone. An example of mono-energetic signatures is shown in Figure 3.4. Figure 3.4b shows a significant and clear intensity enhancement at 13:38:55 around roughly 100 keV identifying signatures related to mono-energetic acceleration processes (Mauk, Haggerty, Paranicas, et al., 2017b). The corresponding regions are marked in parts A and D of Figure 3.3. The classification of broadband or mono-energetic completes the classification scheme for mono-energetic, broadband, and diffuse aurora as summarized in Figure 3.5.

3.3 Results

The application of the classification scheme is only applied to times when Juno is located over the main emission zone, selected by restrictions on the distance r and dipole L-shell parameter L, as described in section 3.2. An overview of the spacecraft's location over the poles is given in Figure 3.6A. Good pitch angle coverage is only provided for the first twenty flybys over the main emission zone, and verified by loss cone calculations depending on the local magnetic field strength (see section 3.2). The resulting time spans with adequate data coverage thus strongly vary in duration while considering all restrictions. Some perijoves only resolve the desired region for less than a minute, some others for more than 10 min. An overview of the resulting length of applicable data is shown in Figure 3.6B. The number of flybys in the southern hemisphere is very limited, as the spacecraft is farther away from Jupiter. A sufficient signal-to-noise ratio also reduces the usable times. Figure 3.6B shows the resulting times in red. The resulting times are used to apply the classification scheme, as described in section 3.2.6, on the pitch angle distribution as well

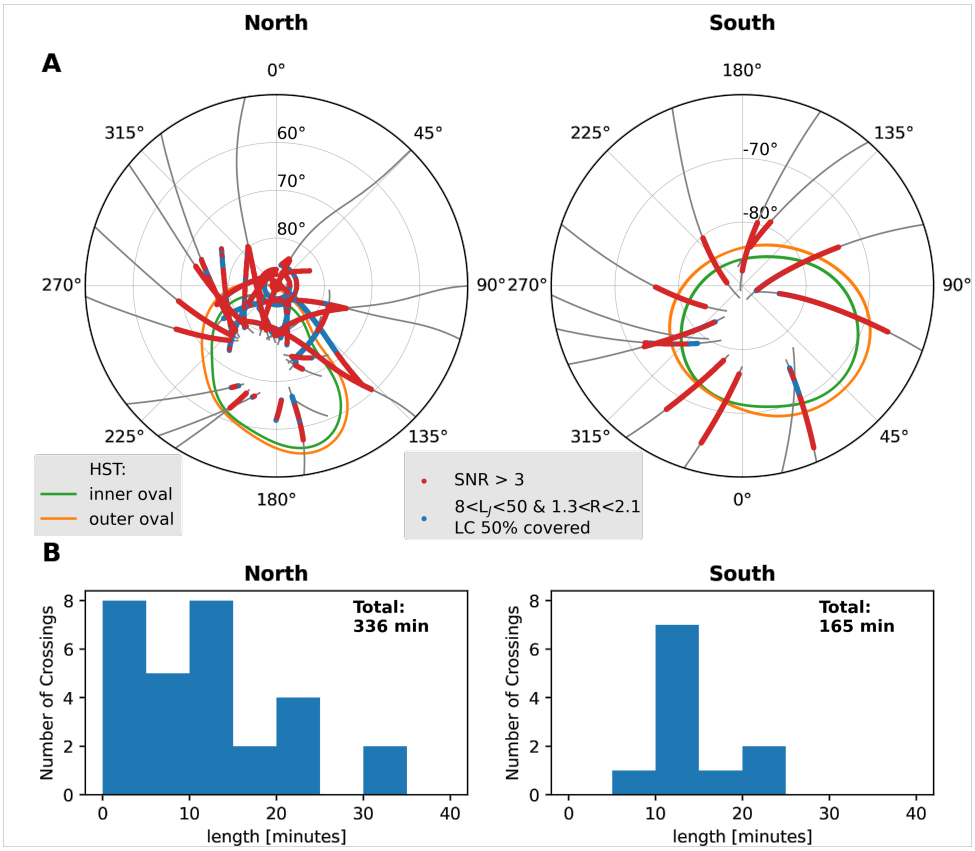

Figure 3.6: Part **A**: Overview of the processed data over the main emission zone in SysIII coordinates. The gray lines show the perijoves of the first 20 flybys, where the blue points mark regions above the main emission zone. The red points overlay the blue points and show the fraction over the main emission zone which provides a sufficient signal to noise ratio of at least 3. Both criteria, blue and red, need to be fulfilled for the distribution to contribute to the statistical analysis. The averaged HST oval from Bonfond et al. (2012) is added by the green and orange lines. Part **B**: Histogram of the spacecrafts crossing duration's over the main emission zone, meeting the blue criteria, for all perijoves.

as on the energy distribution. Both together are used to define the regions of broadband, mono-energetic and diffuse aurora.

The classification via pitch angle distribution shows that the greatest amount of observed particles with pancake distributions is confined to magnetic latitudes less than 76° corresponding to an L-shell of 17, where they contribute by $86.2\% \pm 9.6\%$, as shown in Figure 3.7 A and B. This is not surprising, as diffuse aurora is associated with the scattering of magnetically trapped particles in the radiation zone at low altitudes.

Field-aligned particle distributions increase in occurrence with increasing magnetic latitude and dominate with a fraction of $87.6\% \pm 7.2\%$ for magnetic latitudes greater than 76°, with the mean and standard deviation calculated from their occurrence throughout the L-shell bins. These studies however do only represent the instrument's observation times. A complete overview covering the complete main emission zone is not feasible and our studies are biased by the supported number of measurements within the different magnetic latitudes.

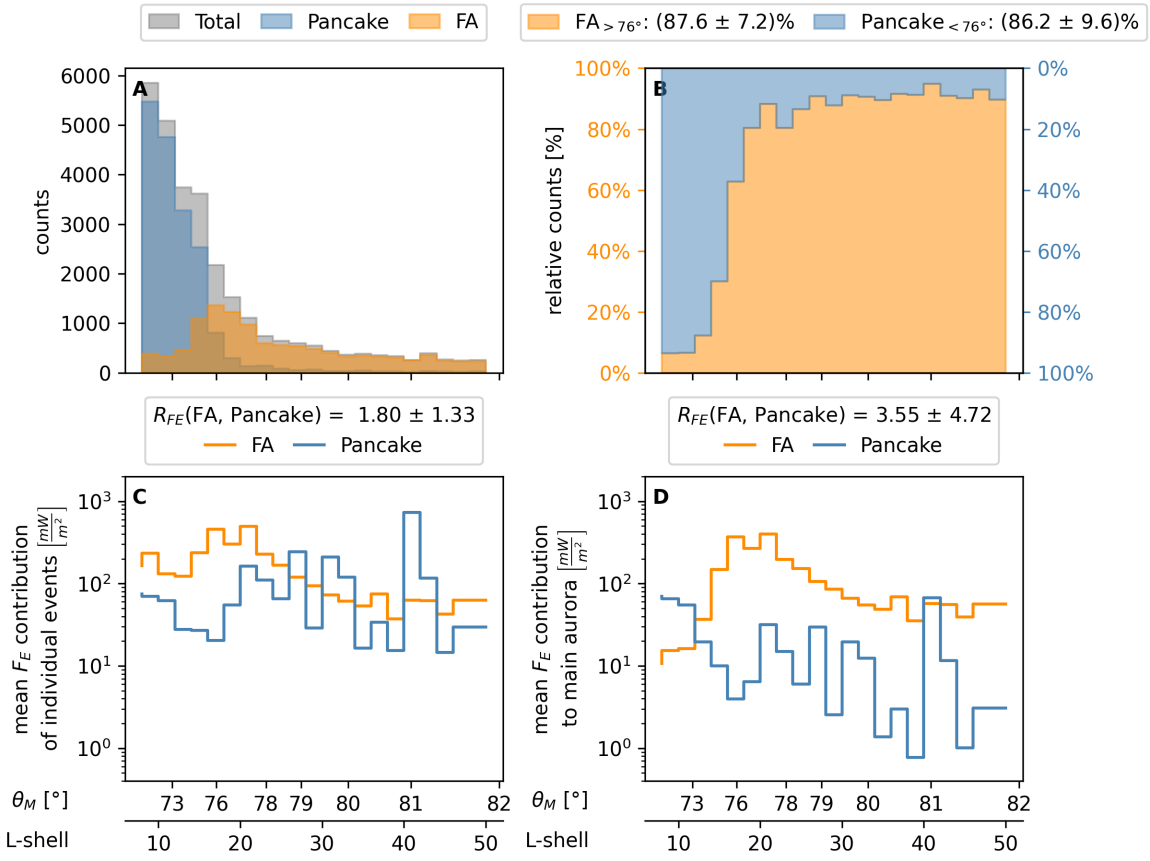

Figure 3.7: Histogram of field-aligned (FA) and pancake distributions as a function of the magnetic latitude, organised by the dipole L-shell. Part **A** shows the absolute number of observations in the corresponding dipole L-shell range. The stacked part of both plots shows the absolute counts of observations, where one count resembles one 0.5 s measurement. Part **B** shows the counts relative to the total number of observed distributions. **C** and **D** show the mean energy flux for the classified distributions for the individual events and over the main emission zone, respectively.

The results from the classification via energy spectra into either broadband or mono-energetic distributions are shown in Figure 3.8, again as a function of the magnetic latitude. Mono-energetic distributions are less frequent than broadband distributions throughout all perijoves. Most of the mono-energetic structures are observable on very small time scales, but some emerge for a long duration even with inverted-V structures as seen in perijove 4 (Figure 3.3). But still, broadband distributions are dominating the field-aligned distributions over 93.0% of the time, where mono-energetic distributions contribute with a small fraction of 7.0% averaged over all dipole L-shells, both with a standard deviation of 3.8% from Figure 3.8B.

The statistical study is applied to the highest temporal resolution of 0.5 s. However, a constant pitch angle coverage, due to the SSDs separation, can only be obtained with a bin size of at least 5 seconds (Mauk et al., 2020). We, therefore, compare the results of our classification scheme based on 0.5 s and 5 s bin size. The contribution of field-aligned and pancake distributions differed by 0.5% and the contribution of broadband and mono-energetic distributions showed a difference of 1.25%. The choice of the bin size between

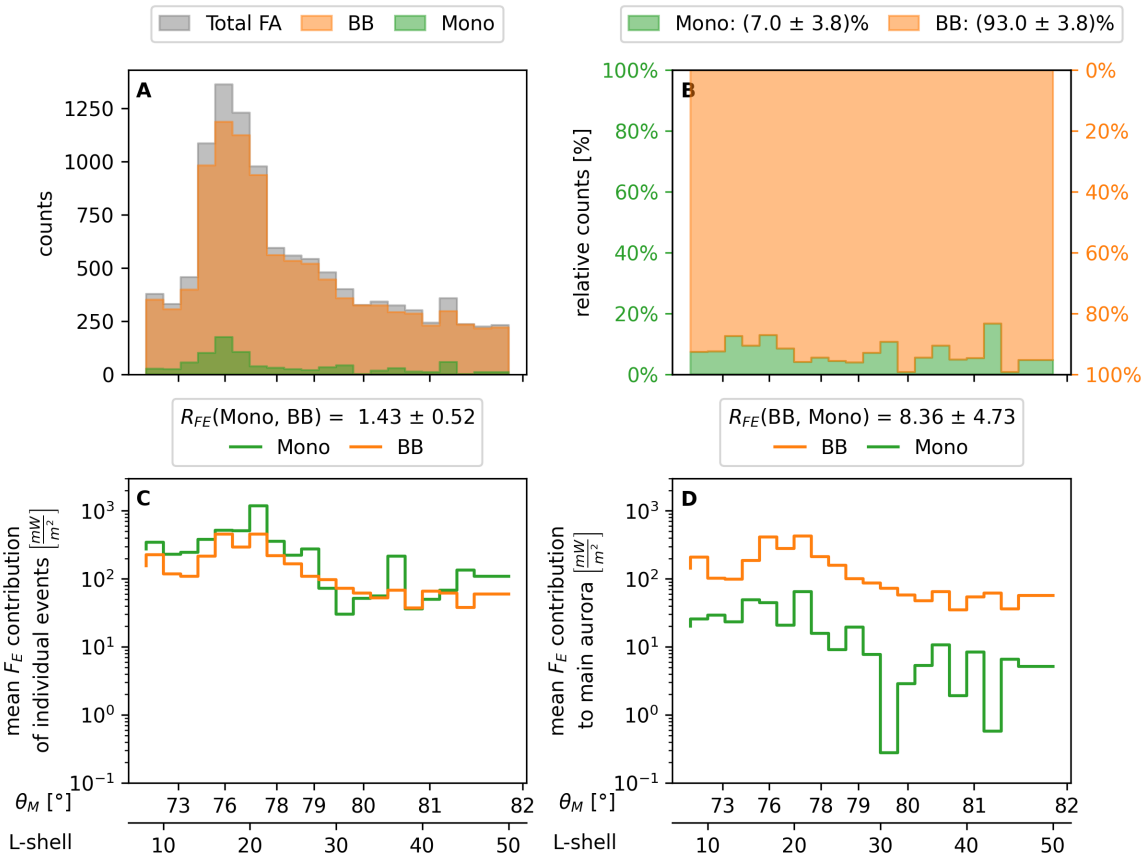

Figure 3.8: Histogram of broadband (BB) and mono-energetic (Mono) distributions for field-aligned particles as a function of the magnetic latitude, distributed/organised by the dipole L-shell. Part **A** shows the absolute counts of classified distributions in the corresponding dipole L-shell range. The stacked part of all plots shows the absolute counts of observations, where one count resembles one 0.5 s measurement. Part **B** shows the counts relative to the total number of observed distributions. **C** and **D** show the mean energy flux for the classified distributions for the individual events and over the main emission zone, respectively.

0.5 s and 5 s thus only shows a minor influence, especially while comparing to the standard deviations of the contributions.

The statistical results are based on comparing the number of 0.5 s measurements identified within each classification category. The statistical analysis can also be performed on the mean energy flux f_E. Let us denote the energy flux within an 0.5 second event at time t_k within a L-shell bin L_j as $f_E^i(t_k, L_J)$, where $i = 0$ stands for field aligned, $i = 1$ for pancake, $i = 2$ for the field aligned subclass broadband, and $i = 3$ for field-aligned subclass mono-energetic events. The average energy flux of individual events of type i within L_j is given by

$$F^i_{E,individual}(L_j) = \frac{1}{N^i_k(L_j)} \sum_k^{N^i_k(L_j)} f^i_E(t_k, L_j) \tag{3.3.1}$$

with $N^i_k(L_j)$ the number of events of type i within L-shell bin L_j. The overall average

energy flux deposited into Jupiter's auroral region is given by

$$F^i_{E,abs}(L_j) = \sum_k^{N^i_k(L_j)} f^i_E(t_k, L_j). \tag{3.3.2}$$

With an average energy flux F_E (i.e. equation 3.3.1 or 3.3.2) we can define the average ratio of the energy flux between types $i = 0$ and $i = 1$ (field-aligned vs pancake) or types $i = 2$ and $i = 3$ (broadband vs mono-energetic) within individual events $R(F_{E,individual})$ and within the auroral region $R(F_{E,abs})$. The following equations describe the ratios between distribution types $i = 2$ and 3, but the ratio of energy fluxes between distribution types $i = 0$ and 1 are defined, similarly. The average ratio of the energy fluxes is given by

$$R(F_E) = \sum_j^{N_j} \frac{F^2_E(L_j)}{F^2_E(L_j) + F^3_E(L_j)} \Bigg/ \sum_j^{N_j} \frac{F^3_E(L_j)}{F^2_E(L_j) + F^3_E(L_j)} \ , \tag{3.3.3}$$

calculated with the energy flux of individual events $R(F_{E,individual})$ and the energy flux within the auroral region $R(F_{E,abs})$. The latter takes into account the higher occurrence numbers of broadband events N^2_k compared to mono-energetic events N^3_k.

The energy flux contribution of field-aligned and pancake distributions shows similar statistics compared to the relative counts, as seen in Figure 3.7 B. Only magnetic latitudes of less than 79° show significant changes. Considering the average energy flux of individual events, we find that the field-aligned distributions exhibit slightly larger energy fluxes than pancake distributions (3.7 C). If we compare the overall energy flux to the main aurora which additionally considers the higher occurrence of the field-aligned electrons compared to the pancake distributions (Figure 3.7B, then we find that the field-aligned energy fluxes significantly dominate. The overall energy flux of the field-aligned distribution is 3.55 ± 4.72 times larger compared to the pancake distribution. Only latitudes of less than 76° show a dominant energy flux contribution by pancake distributions. Some inaccuracies in the determination of these precipitation energy fluxes are governed by the determination of the loss cone size, because of the smearing of the energy flux response due to the finite width of the instrument view cone. This causes an uncertainty in characterizing the energy fluxes associated with trapped pancake distributions.

Similarly, we compare the energy fluxes between the mono-energetic and the broadband distributions. First we consider the energy flux contributions from individual events. We find that individual mono-energetic structures provide on average slightly larger energy fluxes, i.e., $R_{individual} = 1.43 \pm 0.52$ times larger than broadband events. It seems possible that the average energy flux of mono-energetic structures is overestimated by their nature, as they are only prominent when peaking with higher intensities than the background broadband intensities supplying only high-intensity data to the statistics. However, mono-energetic structures are much less frequently observed than broadband

distributions and only contribute an overall energy flux of $10.7\% \pm 5.9\%$ (see Figures 3.8D and 3.8D). This implies that the energy flux of broadband distributions contributing to the main aurora is $R_{abs} = 8.36 \pm 4.73$ times higher (see Figure 3.8D). Therefore, we find that Jupiter's main auroral emissions are primarily produced via precipitating broadband electron distributions.

The classification of pitch angle distributions can be used to study another class of field-aligned distributions into two Zones, introduced by Mauk et al. (2020). Zone I defines the region of dominating downward energy fluxes with $F_{DW} > F_{UW}$ and Zone II where the dominating energy fluxes are upward, with $F_{UW} > F_{DW}$. Mauk et al. (2020) states that Zone I tend to occur at intermediate latitudes characteristic for an active downward acceleration process. Zone II tends to occur at high latitudes and is associated with an upward acceleration process. Bidirectionality in this zone is possible due to downward energy fluxes originating from an upward acceleration process in the opposing hemisphere Mauk et al. (2020). The occurrence of both zones in dependency on the magnetic latitude for field-aligned particles distributions is shown in Figure 3.9A and B. Both zones are present over the whole magnetic latitude range. Zone I has a high occurrence at small magnetic latitudes of less than 78°, whereas Zone II dominates the higher magnetic latitudes. A maximum occurrence of Zone II is given around $\theta_M = 80°$. Part C and D of Figure 3.9 show that bidirectionality is dominating the intermediate magnetic latitudes centered around $\theta = 76°$. All 4 plots show a region dominated by downward energy fluxes for small magnetic latitudes. One may speak of three regions, the first one dominated by downward flux, followed by a mostly bidirectional region, and one region at high magnetic latitudes with strong upward energy fluxes.

3.4 Discussion

This statistical study is based on JEDI measurements located over the main emission zone, with a radial distance of 1.2 to 2.5 R_J and dipole L-shell between 8 and 50. Further restrictions follow from appropriate pitch angle coverage and sufficient signal-to-noise ratio larger than three. Hence, the first twenty Juno flybys enable a total observation length of 336 min in the northern hemisphere and 165 min in the southern hemisphere. An overview of the different occurrences resulting from the classification scheme is summarized in Table 3.1.

The classification via pitch angle distributions showed that field-aligned distributions dominate with a mean fraction of $87.6\% \pm 7.2\%$ over magnetic latitudes between 76° and 82°. Pancake distributions have a little contribution of 13.8% within the higher magnetic latitudes but strongly contribute by $86.2\% \pm 9.6\%$ within small magnetic latitudes of less than 76°. 63% of the pancake distributed measurements provide a larger energy flux in the downward direction compared to the upward direction and thus, are associated with

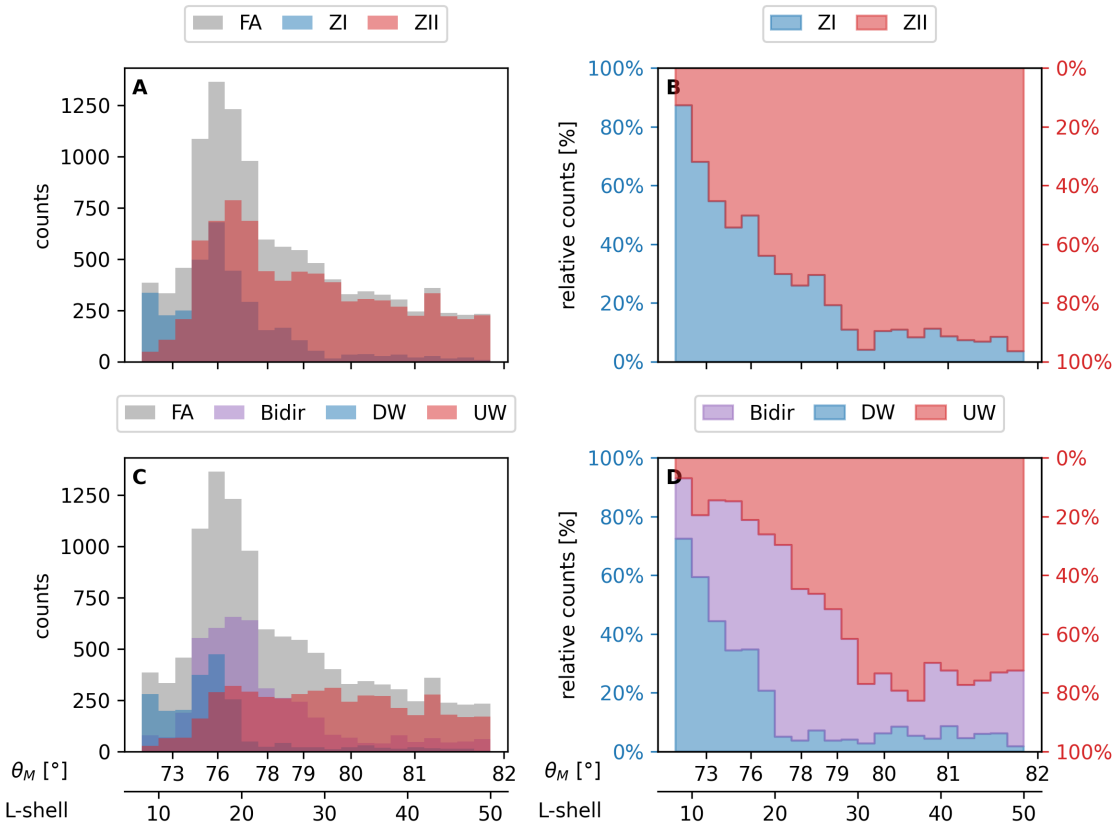

Figure 3.9: Histogram of Zone I (ZI) and Zone II (ZII), as well as upward (UW), downward (DW), and bidirectional (Bidir) distributions, for field-aligned particles as a function of the magnetic latitude, distributed/organised by the dipole L-shell. Part **A** and **C** show the absolute counts of classified distributions for the corresponding magnetic latitude. The stacked histogram (gray) of both parts shows the absolute counts of observations, where one count resembles one 0.5 s measurement. Part **B** and **D** show the counts relative to the total number of observed distributions.

diffuse aurora. Pancake distributions with dominating upward energy flux are embedded in low energy flux regions, where downward and upward energy fluxes are equally small. Our statistics showed that pancake distributions are likelier at smaller dipole L-shells, confirming expectations from Diffuse aurora.

The classification via energy spectra showed that broadband distributions observed account for $93.0\% \pm 3.8\%$ of the measurements averaged over all observed dipole L-shells, clearly dominating the field-aligned distributions. Mono-energetic structures are rarely observed with a total amount of $7.0\% \pm 3.8\%$ averaged over all dipole L-shells, with no clear preference to particular spatial parameters, such as radial distance or magnetic latitude. Most of the identified mono-energetic structures were observed when the background broadband intensities were small. Some mono-energetic structures showed only small deviations from strong background intensities indicating a broadband distribution. It thus appears that some mono-energetic structures possess smaller intensities than broadband structures and are therefore hard to distinguish within strong background broadband distribution. The rate of mono-energetic structures may therefore be underestimated,

Table 3.1: Summary of relative occurrence of the analyzed distribution functions. Pitch angular distributions are compared within two intervals separated at the 76° magnetic latitude corresponding to a dipole L-shell of 17.

	Field-aligned	Pancake	standard deviation
$\theta_M > 76°$	87.6%	13.8%	7.2%
$\theta_M < 76°$	12.4%	86.2%	9.6%
	Mono-energetic	Broadband	standard deviation
Field-aligned	7.0%	93.0%	3.8%

but the contribution of mono-energetic structures to auroral acceleration may still be comparable due to the small intensities. Broadband distributions, though, are also somewhat underestimated as a superposition of broadband and mono-energetic distributions is classified as a mono-energetic distribution.

The classification via pitch angle distributions also offered an overview of dominating flux in the upward and downward directions. The statistics showed that dominating downward energy fluxes often occur at small magnetic latitudes, whereas upward energy fluxes are dominant within higher magnetic latitudes. A transition between both regions occurs in presence of bidirectional distributions, which dominate the magnetic latitudes from 74° up to 79°. These results confirm the observations made by Mauk et al. (2020) that downward electron acceleration mainly occurs at intermediate latitudes, whereas upward electron acceleration mainly occurs at high latitudes, possibly originating from upward and downward current regions, respectively. This conclusion partly explains the bidirectional pitch angle distributions, resulting from upward electron acceleration from both hemispheres. We summarize our findings in the following list:

1. Two zones are observed, separated at magnetic latitude 76°, where field-aligned distributions are prominent at higher magnetic latitudes and pancake distributions at smaller magnetic latitudes, indicating diffuse aurora.

2. Our statistic shows a dominant occurrence of broadband distributions, rather than mono-energetic structures which were rarely observed with a total amount of 7.0% averaged over all dipole L-shells within 8 and 50. No clear preference to particular spatial parameters could be observed.

3. A transition takes place, where dominating downward energy fluxes at small magnetic latitudes interchange through a bidirectional zone with dominating upward energy flux with higher magnetic latitudes, affirming observations made by Mauk et al. (2020).

4. Bidirectionality is a persistent pitch angle distributions property throughout the high magnetic latitudes and therefore suggests rather a bidirectional acceleration process than an upward acceleration from both hemispheres.

Our observed results might not fully represent the real statistical distribution because of the observational bias by the spatial coverage and restrictions of Juno's flybys. Field-aligned distributions are strongly dominated by broadband energy spectra with a contribution of 93.0%. Comparison of mean energy flux statistics with the count statistics showed similar results. Although broadband and mono-energetic distributions have comparable energy fluxes, mono-energetic distributions contribute little to the total amount of energy flux compared to broadband distributions and do not provide the main energy flux to the main emission zone.

The type of energy distribution gives information about the acceleration processes of the particles. Mono-energetic distributions usually result from electrostatic potentials, whereas broadband distributions result from stochastic acceleration processes. The presented statistic therefore contribute to the discussion about possible and probable acceleration processes and theories about the generation processes of Jupiter's aurora and most importantly to a quantitative contribution of the associated acceleration processes. The dominant occurrence of broadband distributions, within our statistics, supports the theory of a stochastic acceleration process as the dominant auroral driver. Mono-energetic structures are rarely observed, additionally, neither over a great amount of time or spatial sizes nor with a strong energy flux contribution.

These findings identified a mono-energetic distribution occurrence of 7.0% , which does not match the expectations prior to the Juno mission. A static current system as the dominant auroral driver, accelerating particles along with electrostatic potentials as introduced by Knight (1973), does not seem to be the dominant acceleration process for the electrons observed by Juno. The average occurrence of broadband distribution with more than 90% over the observed times does not suit the classic image but underlines the importance of a turbulent or stochastic acceleration process (e.g. Saur et al., 2018; Damiano et al., 2018; Elliott, Gurnett, Kurth, Clark, et al., 2018; Lysak et al., 2021), as the dominant driver of the unique Jovian aurora.

Open Research

The Juno-JEDI data were obtained from the website of the NASA Planetary Data System:Planetary Plasma Interactions (`https://pds-ppi.igpp.ucla.edu/mission/JUNO/JNO/JEDI`). Juno footprints data using JRM09 and CAN models is available at `https://lasp.colorado.edu/home/mop/files/2020/04/20190412_Imai_MagFootReader_UIowa_rev.pdf`. The classification results of this study are listed in Table 1 within the Supporting Information.

Acknowledgments

This research was supported by Deutsche Forschungs Gemeinschaft through the specialty program Jupiter's aurora: Data analysis of Juno/JEDI data and modeling of auroral electron acceleration (SA 1772/6-1) and by the Graduate School of Geosciences (GSGS) of the University of Cologne. Bagenal et al. (2017) was used as a reference to the utilized coordination systems (`https://lasp.colorado.edu/home/mop/files/2015/02/CoOrd_systems7.pdf`).

Data availability

Classification results for perijoves 1 to 20 for times when the spacecraft location is mapping to the main emission zone (r from 1.3R_J to 2.1R_J and L from 8 to 50).

Line 1: Column headings

> `PJ` perijove, `Epoch`, `SNR` signal to noise greater 3, `LC_resolved` loss cone is resolved, boolean classification results [`Broadband`, `Monoenergetic`, `FieldAligned`, `Bidirectional`, `Pancake`, `Diffuse`], `FE_Out` upward energy flux, `FE_UW` energy flux outside of the loos cone, `FE_DW` downward energy flux, `L-shell`, `M-shell`, `R` radial distance, `Wlon_JRM09` JRM09 West longitude, `Lat_JRM09` JRM09 latitude of satellite, and `magnLat_JRM09` magnetic latitude at r =R_J.

Lines 2-end: Listing of variables

CHAPTER 4

PART II: MAGNETIC WAVE-PARTICLE INTERACTION

The research into auroral electrons, as discussed in chapter 3, showed that the acceleration of these electrons cannot be solely attributed to static potential differences, as is the case on Earth. The electrons exhibit high intensities over a wide range of energies, resulting in a broadband energy distribution for more than 90% of the times observed in chapter 3. This dominant fraction of broadband distributions emphasizes the importance of other acceleration processes and a potential transition or combination of different acceleration processes in Jupiter's magnetosphere. As seen in section 2.1, other acceleration theories have already been discussed. In particular, broadband acceleration has been attributed to wave-particle interactions resulting from turbulent processes in the plasma sheet. The magnetospheric waves can cover a wide range of frequencies and wavelengths on which wave-particle interaction with electrons and ions may occur, resulting in accelerated particles on a broad range of energies. Therefore, it is essential to explore the wave-particle interactions by examining the particles and waves in the plasma that power the intense auroral emissions at Jupiter.

Plasma waves are composed of electric and magnetic fields that oscillate perpendicularly to each other. These fields are self-sustaining, meaning that the oscillations in one field induce oscillations in the other, leading to continuous wave propagation. The magnetic and electric fields' oscillations exert forces on charged particles within the plasma, creating a complex interplay between the electric and magnetic fields and the particles in the plasma. For example, when the wave's frequency matches the inertia length of the electron's motion, energy is transferred between the wave and the electron, resulting in an acceleration of the electron and damping of the wave. Thus, magnetic field fluctuations provide a deeper insight into the wave-particle interactions and, thus, possible acceleration sources for the auroral electrons. The magnetic field fluctuations can be detected by observing sudden, random changes in the intensity and direction of a magnetic field. These changes must be distinguished from the background magnetic field, provided by internal and external sources, as further explained in section 4.1.2.

4.1 Instrument, Data and Methods

This chapter examines the analysis and interpretation of the data collected by the Juno spacecraft using the Fluxgate Magnetometer (FGM) and the Juno Ultraviolet Spectrograph (UVS). The primary focus is to understand the magnetic field fluctuations, auroral patterns, and the limitations of the instruments used for the analysis. Initially, the FGM is introduced (see section 4.1.1), and the processing of the magnetic field data is outlined. In section 4.1.2, fluctuations are identified to detect any local or temporal changes in the environment. Unidirectional changes, known as "magnetic surges," are discussed and linked to associated electric currents (section 4.1.3). The energy of varying field amplitudes is investigated in the frequency domain, introducing the Fourier theorem and Power Spectral Densities (PSDs) (section 4.1.4). Finally, the images of the UVS are presented in section 4.1.5, mapping the associated image slices along the spacecraft flight trajectory.

4.1.1 Fluxgate Magnetometer

Juno is equipped with a Fluxgate Magnetometer (FGM), which can detect the magnetic field intensity and direction at 64 samples per second. The magnetometer allows observing magnetic field variations on short temporal and spatial scales. The Fluxgate Magnetometers (FGMs) works by measuring the magnetic flux changes in a ferromagnetic core when exposed to an external field, allowing it to identify and measure the surrounding magnetic field. All three dimensions are measured simultaneously using one sensor for each direction. Two sensor suites are connected to a four-meter-long magnetometer boom and attached to one of the three solar arrays. The first suite is mounted ten meters from the spacecraft, while the second is twelve meters away. The magnetic field offsets of the sensor suites are utilized to acquire an accurately measured field, mostly unaffected by the spacecraft rotation (with a rotation period of 30 s). An onboard star camera is utilized to achieve an accuracy of 100 ppm for the magnetic field vectors. This camera provides four attitude solutions per second based on the position of fixed stars concerning the spacecraft's orientation. The magnetometer can measure a wide range of values, from a few nT up to 16 Gauss (equivalent to 1.6 million nanoteslas). The analog magnetic field data is brought to a digital form, leading to a quantization of each value, meaning that they are rounded to the nearest available digital value. The digitization level corresponds to the minimum step size of the digital values. It is dynamically adjusted, with the most sensitive range of $\pm 1600\,\mathrm{nT}$ per axis digitized with a resolution of $\sim 0.05\,\mathrm{nT}$, and the highest range digitized with a resolution of 25 nT. An example of the different dynamically adjusted digitization levels is shown in Figure 4.1. When examining Jupiter's magnetic field at radial distances of less than $2\,\mathrm{R_J}$, the magnetic field is already of the magnitude of $1 \times 10^5\,\mathrm{nT}$. In this case, the digitization level is mainly determined by levels 5 and 6, which correspond to 6.25 nT and 25 nT, respectively. The FGM has an intrinsic noise level that is extremely small, with

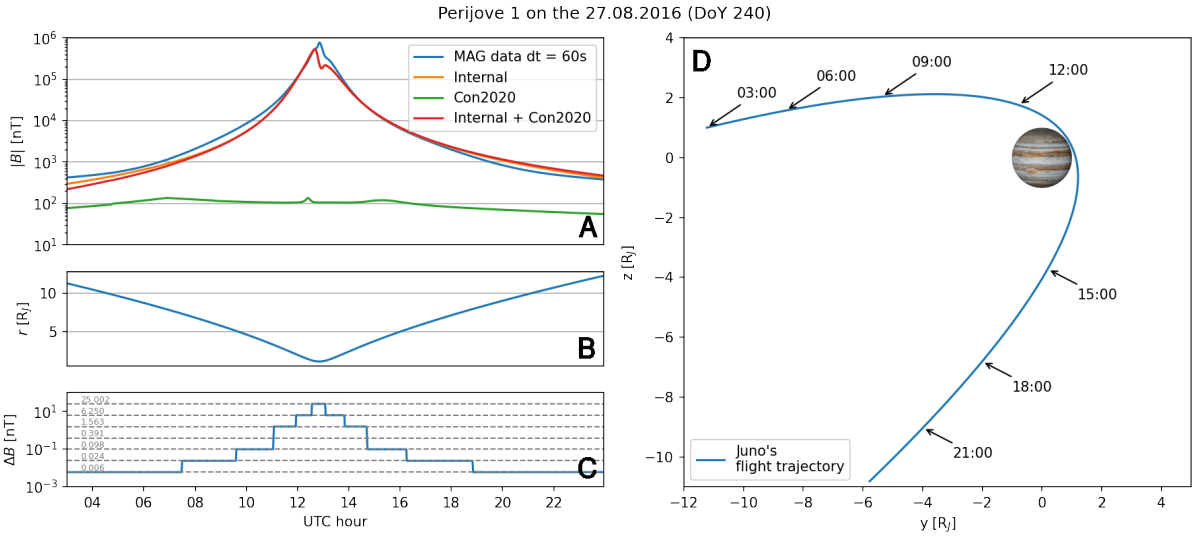

Figure 4.1: This graph gives an overview of the magnetic field data from the first Perijove on 27.08.2016. Panel A shows the magnetic field data from the MAG instrument and the magnetic field model based on internal and external sources. Panel B displays the radial distance from Jupiter's center. Panel C illustrates the digitization level of the given times, with the exact value indicated by the gray line and the respective value written on the left side. Lastly, panel D presents the Juno flight trajectory in the non-rotating Jupiter-centric coordinate system.

$\ll$1 nT, compared to the digitization levels. This means that the digitization level is the limiting factor when observing the magnetic field components at the smallest variations. Further details of the resulting limitations to the analysis are given in section 4.1.4.

The magnetic field data used are accessible from the Planetary Data System (NASA Planetary Data System, 2022) in planetocentric coordinates. It has already been calibrated and can be obtained in different temporal cascades. The smallest temporal resolution is 64 samples per second, which can sometimes drop to 16 samples per second. The timestamps of the data points are digitized at a resolution lower than the time cadence, meaning that the digital representation does not precisely reflect the original continuous-time signal. This results in unevenly spaced or nonequidistant time intervals between data points. To address this temporal quantization error, the timestamps must be adjusted to equidistant time steps in a 64 Hz cascade, using the nearest value at each equidistant step.

4.1.2 Magnetic Field Fluctuations

In order to observe the magnetic field fluctuations due to local or temporal environmental changes, the statically assumed background magnetic field needs to be subtracted. Therefore, the community code from Wilson et al. (2023) is used to obtain the internal and external magnetic field components in SysIII coordinates. The internal magnetic field model is given by JRM33 from Connerney et al. (2022), conducted by observing the first 33 perijoves and describing the first 30 degrees of spherical harmonics. The external magnetic field model is given by the Connerney 2020 current sheet model (Con2020) introduced

by Connerney et al. (2020). By subtracting internal and external fields from the original magnetic field data, the magnetic deviations δB_i for each component i in the ϕ, θ, and r directions can be calculated. These magnetic deviations are exemplarily shown for the first perijove in Figure 4.2 panel A. Panel B and C of Figure 4.2 show a time of the

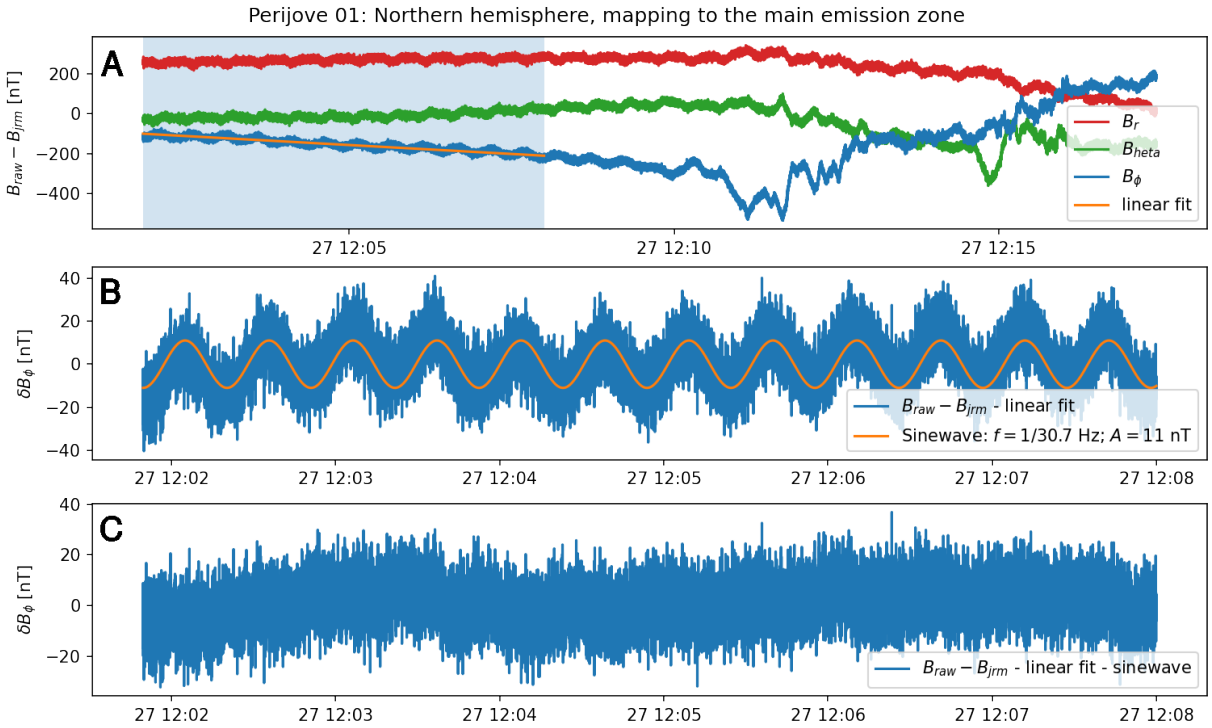

Figure 4.2: The magnetic field deviations for the first perijove over the northern main emission zone are displayed in panels A, B, and C. Panel A shows the original magnetic field data minus the background magnetic field, with a linear fit added to the area highlighted in blue. Panels B and C only display the times corresponding to the blue-shaded region. Panel B shows the magnetic field data minus the linear fit, with an additional sine wave fit in orange. The magnetic field fluctuations are depicted in panel C after subtracting them. The sine fit demonstrates the cyclic nature of the magnetic field fluctuations but is not used for further analysis.

perijove where the changes in the magnetic field are of amplitudes less than 50 nT. A linear fit can subtract any potential misfit from the background magnetic field, leaving a residual that indicates periodic changes, suggesting an effect caused by the spacecraft's rotation. The magnetic field components are given in SysIII coordinates, which should not be affected by any rotation of the coordinates with the spacecraft system. However, a clear sine-wave dependence is observed, with a period of 30.7 s corresponding to the spacecraft rotation period. These periodic changes are seen throughout most flybys and always have a period of ≈30 s. Kotsiaros et al. (2020) studied these periodic deviations and analyzed the correlation with eddy currents, which occur in strong magnetic field environments at Juno's periapsis. These currents emerge from the electrically conductive material near the magnetic sensors rotating in the strong magnetic field environment with more than 1 Gauss (= 10^5 nT). These currents then induce magnetic fields themselves, affecting the magnetic field measurements of the FGM. Kotsiaros et al. (2020) introduces a finite

element model of the induced field and a model to eliminate the contribution of the eddy currents to the measured field. The correction is applied in the payload coordinate system of the spacecraft and thus cannot be directly applied to the planetocentric coordinates used here. Consequently, no correction will be made due to the spacecraft's spin. It is essential to remember that any period changes with periods multiples of the spacecraft's rotation may be induced by eddy currents. An automated fitting procedure for a basic sine wave is not used since the period alters rapidly, even in a few minutes. Furthermore, the eddy currents are directly associated with the intensity of the background magnetic field, which also fluctuates. The magnetic field fluctuations are closely monitored to the original magnetic field data in order to avoid any misinterpretation of any computational effects that may be superimposed.

Thus, the magnetic field fluctuations are only determined by subtracting the background magnetic field (JRM33 and Con2020) and a linear trend to eliminate any remaining discrepancies. The resulting magnetic field components are given by longitudinal δB_ϕ, latitudinal δB_θ and radial δB_r direction, as displayed in Figure 4.2. The longitudinal and latitudinal components of the magnetic field show the most notable changes, while the radial component remains almost unchanged, apart from the oscillations caused by the spacecraft's rotation. The radial component of the magnetic field is generally consistent with the magnetic field vector, assuming a dipolar magnetic field observed at a close distance. Thus, the radial component can be described as the field-aligned magnetic field component. The longitudinal and latitudinal components of the magnetic field are perpendicular to the magnetic field. When the changes in these perpendicular components are analyzed, it can be inferred that parallel electric fields are present. These parallel electric fields can generate perpendicular magnetic fields, which in turn cause changes in the components of the perpendicular magnetic field. Thus, the magnetic field components shown in Figure 4.2 provide evidence of parallel electric fields above the main emission zone.

Examining the presence of magnetic field fluctuations can benefit both the time and frequency domains, as the fluctuations occur over a wide range of periods, from several minutes to less than a second. Magnetic field alterations on a broad time scale usually demonstrate a single powerful magnetic field alteration in a positive or negative direction. These modifications can be associated with electrostatic field-aligned currents, also known as Birkeland currents. The following subsection briefly discusses corresponding magnetic field changes, considering possible static current directions and resulting magnetic field observations. Investigations of magnetic field fluctuations on shorter temporal scales of a few seconds or minutes are better studied in the frequency domain, where the contribution of the magnetic field changes on different time scales can be separated. Wavelet analysis examines the energy within changing field intensities, considering both temporal and frequency changes, as discussed in section 4.1.4.

4.1.3 Magnetic Surges and Unidirectional Currents

As Juno passes through magnetic field lines that map to the main emission zone along connecting magnetic field lines, particle observations have revealed large spatial regions with either dominant electron acceleration towards or away from the planet. These regions, referred to as Zone I (ZI) and Zone II (ZII), show a dependence of the preferred direction of electron acceleration on the magnetic latitude. It is hypothesized that powerful Birkeland currents are created along the magnetic field lines, causing electrons to be accelerated in one direction. These currents can be detected by mainly observing unidirectional changes in the perpendicular components of the magnetic field. The sign of the magnetic field gradient can thereby directly be related to the direction of the filed-aligned current, which points either upward or downward to Jupiter. The sign thereby depends additionally on the Juno flight direction, either towards or equatorward, and the direction of the magnetic field which is either upward in the northern or downward in the southern hemisphere.

Let us assume the configuration of poloidal current regions, represented as oval bands on top of Jupiter's atmosphere, as illustrated in Figure 4.4. Red ovals indicate upward current regions and blue ovals indicate downward current regions. An approximated Juno flight trajectory is indicated by the horizontal red line, disregarding the planet's rotation. As the spacecraft passes through different regions of upward and downward currents, it experiences the curl of $\mathbf{B}$ induced by the field-aligned current following Ampères law

$$\nabla \times \mathbf{B} = \mu_0 \mathbf{j}. \tag{4.1.1}$$

Here, the current density $\mathbf{j}$, the vacuum permeability μ_0, and the magnetic field $\mathbf{B}$ describe the basic relation for the current densities with the magnetic field. Let us assume a current flowing in the z direction parallel to a background magnetic field; then the j_z component can be deduced from eq. (4.1.1) as

$$j_z = \frac{1}{\mu_0} \left(\frac{\partial B_y}{\partial x} - \frac{\partial B_x}{\partial y} \right), \tag{4.1.2}$$

where x and y are the coordinates in the perpendicular plane and B_x and B_y the corresponding magnetic field components. Assuming a perpendicular flight through a current sheet that is sufficiently elongated in the y and z directions, the x direction is normal to the sheet, and changes in the B_x component along the sheet in the y direction are negligible. Thus, the second term on the right-hand side of eq. (4.1.2), $\frac{dB_x}{dy}$, can be ignored.

$$j_z = \frac{1}{\mu_0} \frac{\partial B_y}{\partial x} \tag{4.1.3}$$

A single spacecraft does not allow for instantaneous measurements of spatial gradients but provides spatial resolution over time due to the spacecraft's velocity. Hence, if we assume

the magnetic field to be static, the spatial gradient can be calculated using the velocity with

$$j_z = \frac{1}{\mu_0 v_\perp} \frac{\Delta B_y}{\Delta t}, \tag{4.1.4}$$

where Δ is the difference between two data points. It must be noted that the spatial gradient can only be determined along the path of the spacecraft, meaning that only a portion of the field-aligned current can be identified unless the current sheet is perpendicular to the spacecraft trajectory, as introduced by (Luhr et al., 1996).

A different approach is to approximate the current in the sheet by several current wires. The magnetic field of a single current filament can be represented by the Biot-Savart law for an infinite wire.

$$\mathbf{B}(\mathbf{r}) = \frac{\mu_0 I}{2\pi r} \quad \mathbf{e}_\phi \tag{4.1.5}$$

$$\mathbf{B}(\mathbf{r}) = \frac{\mu_0 I}{2\pi r} \left(\cos\theta \mathbf{e}_y - \sin\theta \mathbf{e}_x\right) \tag{4.1.6}$$

Let us assume the current sheet is a locally confined current region described by an infinite wire. One can distinguish the relation of the magnetic field components to the radial distance r and x coordinate relative to the wire with $x = r \cdot \cos\theta$, as follows:

$$B_y(x, r) = \frac{\mu_0 I}{2\pi r^2} \cdot x \tag{4.1.7}$$

$$B_y(x, r) = \frac{\mu_0 I}{2\pi r^2} \cdot \sqrt{r^2 - x^2} \tag{4.1.8}$$

This equation is then applied to various synthetic cases, as shown in Figure 4.3.

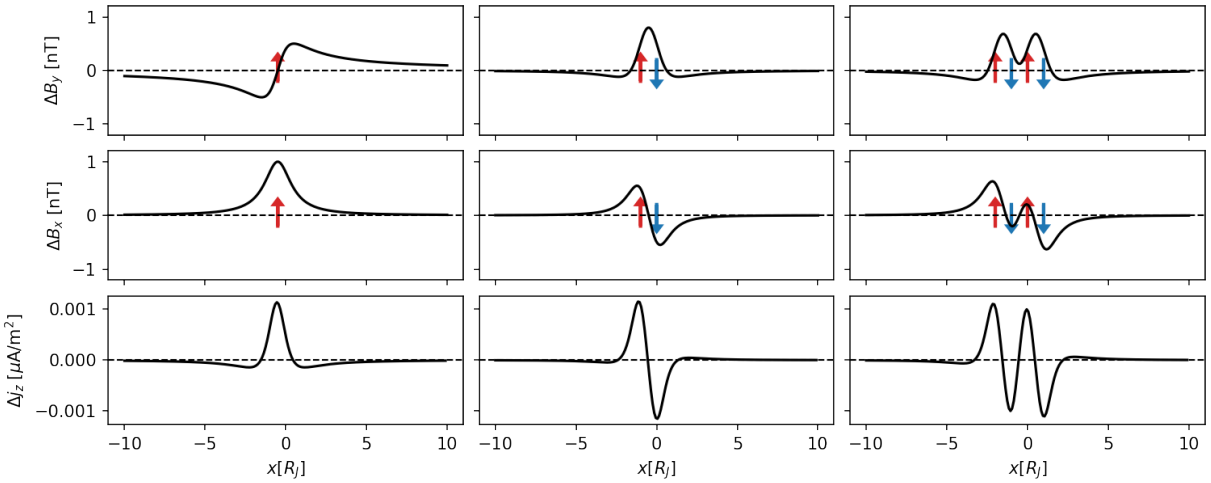

Figure 4.3: The three panels show different arrangements of 1, 2, and 4 field-aligned currents (indicated by blue and red arrows) and the associated magnetic field component B_ϕ. The x-axis indicates the spacecraft's position relative to the field-aligned currents, while the y-axis shows the magnetic deviation. The magnetic field component varies when the spacecraft crosses a field-aligned current with $j_\parallel$.

In Figure 4.3, the magnetic field components B_x and B_y perpendicular to a current along the axis z are depicted. Particular attention should be paid to B_y, parallel to the x, z plane. If a current sheet is present in the x, z plane, then changes in the magnetic field in the y direction will be cumulative, while those in the x direction will be counterbalanced. The B_y component shows a distinct pattern for each current, where a sudden sharp deviation occurs each time. The deviation is characterized by a rapid increase or decrease centered on the current wire location. The magnetic field is seen to experience strong fluctuations with a distinct slope and considerable deviation from the standard. For the sake of simplicity, these variations are referred to as *magnetic surges*, which are possibly caused by electrostatic potentials.

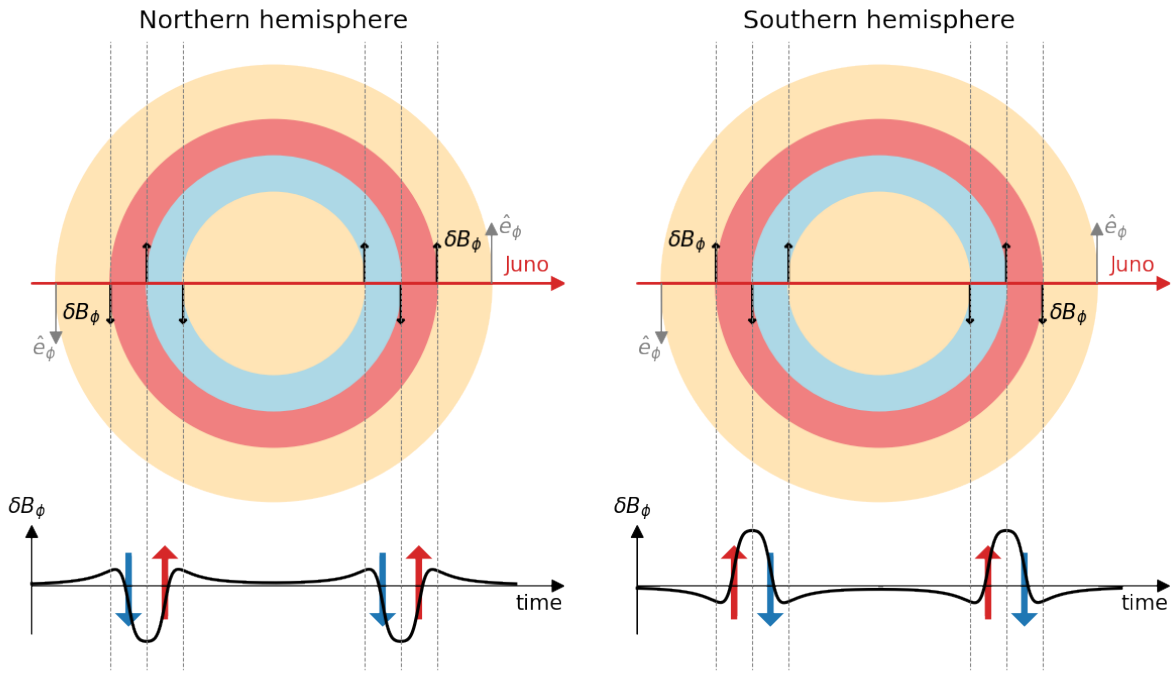

Figure 4.4: The FGM on Juno observed changes in the B_ϕ component of the magnetic field when crossing poloidal static current sheets. Red regions correspond to upward currents, and blue regions correspond to downward currents. Both hemispheres are shown from the top view from north of Jupiter, with coordinates given in the right-hand side SysIII. Magnetic field gradients are schematically emphasized with the colored arrows in the lower part of the figure.

To transfer these observations to the polar current system of Jupiter, we will consider the z axis again aligned with the FAC, therefore in the r direction of the Jupiter system. This approximation holds for low altitudes and thus is sufficient for the following investigations. The y component is aligned with the current sheet plane and resembles the ϕ components, whereas the x component resembles the θ component. The magnetic field component B_ϕ thus corresponds to the direction of the strongest expected magnetic field deviation from the radial current. This component reverses its direction when the spacecraft transitions from one side of the sheet to the other. Assuming that the current flows in the radial

direction along the background magnetic field, one can approximate the parallel current density $j_{\parallel}$ by the current density in the r direction. The current density can be derived from Ampère's law in the cartesian coordinate system (see eq. (4.1.3)) while changing to the spherical coordinate system as follows:

$$j_r = \frac{1}{\mu_0 r \sin\theta} \left(\frac{\partial (B_\phi \sin\theta)}{\partial \theta} - \frac{\partial B_\theta}{\partial \phi} \right) \tag{4.1.9}$$

A significant advantage of the current density is that the flight direction and the direction of the magnetic field do not affect its direction. Positive current densities point away from the planet, and negative currents point toward the planet. However, the magnetic field variations depend on the direction of the magnetic field and the flight direction, either towards the poles or the equator, as demonstrated in the following study.

We will consider a perfectly symmetric current sheet to gain a schematic understanding of the directional changes in the component parallel to the current sheet B_ϕ and perpendicular to it B_θ. Figure 4.4 displays a schematic diagram of the related set-up, with a top-down view from the northern hemisphere at the north and south poles. As the perspective is the same for both hemispheres, the orientation of the SysIII unit vectors remains the same, represented by the gray arrows. It is worth noting that the upward currents, i.e., away from Jupiter, point out of the plane for the northern hemisphere but into the plane for the southern hemisphere. The opposite is true for downward currents, which point towards the planet. When the spacecraft transitions a current sheet, each time it experiences a magnetic field change in the B_ϕ component. If two current sheets are placed side by side, the curl of B accumulates in the middle, leading to a significant difference in the magnetic field between the two regions. This alteration is seen each time the current sheets are crossed, as shown in Figure 4.4 by the graph at the bottom. However, the direction of the magnetic field change depends on the direction of the currents within the sheets and on the direction of the flight, either in the same direction as the latitudinal unit vector or in the opposite direction. We can identify four distinct crossings for Juno's flight path, two of which are towards the poles and the other towards the equator. The interplay with the direction of the magnetic field, which is different in both hemispheres, leads to typical flight trajectories, resulting in two groups experiencing the same magnetic field fluctuations with downward or upward currents. When Juno is located at a radial distance of less than $3\,\mathrm{R_J}$, upward electrostatic currents can cause δB_ϕ to transition from a positive field strength to a negative field strength. In contrast, when Juno is situated between $3\,\mathrm{R_J}$ to $8\,\mathrm{R_J}$, downward electrostatic currents can cause δB_ϕ to change from a positive field strength to a negative field strength. In either case, the opposite direction of the current would result in δB_ϕ changing from negative to positive field strength.

We can infer that electric currents flow along the magnetic field lines away from and toward the planet when determining whether a surge is of a positive or negative slope.

These findings can then be compared to UVS and JEDI data to validate them with more detailed particle data. For instance, if negative surges are observed in the northern hemisphere when the spacecraft passes through the main emission zone while traveling toward the equator, this would suggest a downward current region. This would likely mean that ions are accelerated upwards away from the planet, and electrons are accelerated towards the planet. With intense electron energy fluxes in the downward direction, strong UV emissions are expected. Therefore, observing all three instrument data will expand the view of the event and partially validate each other.

4.1.4 Power Spectral Densities

The magnetic field fluctuations observed during the perijoves vary greatly in amplitude and time, from a few seconds to an hour. However, the contribution of short-term changes over a few minutes is usually not visible in the temporal domain. Additionally, the spacecraft's rotation significantly influences the magnetic field components in almost every perijove. Therefore, analyzing the magnetic field components in the frequency domain separates the different frequency components in a signal to disregard the noise by focusing on specific frequencies of interest.

The next part will briefly overview wavelet analysis theory, further discussed in Torrence and Compo (1998). This theory is based on the Fourier theorem, which states that a finite and piece-wise continuous signal can be expressed as a combination of sine and cosine functions of various frequencies f_n.

$$u(t) = \sum_{n=-\infty}^{\infty} \bar{u}[n] \exp\left(-2\pi i f_n t\right) \tag{4.1.10}$$

$$\bar{u}[n] = \frac{1}{T} \int_{t_0}^{t_0+T} u(t) \exp\left(2\pi i f_n t\right) dt \tag{4.1.11}$$

with $\bar{u}[n]$ the Fourier coefficients. The terms in eq. (4.1.10) each represent an oscillation at a frequency $f_n = n/T$. The sum of the two terms in n and $-n$ is the amplitude of the signal associated with a particular time scale $1/f_n$. When considering a real signal, the sum must be real. The Fourier coefficients must satisfy $-\bar{u}[n] = \bar{u}^*[n]$, resulting in the sinusoidal wave amplitudes being $2\bar{u}[n]$ for frequencies $f_n > 0$ (Paschmann & Daly, 1998). Through Parseval's relation

$$\frac{1}{T} \int_{t_0}^{t_0+T} u^2(t) dt = \sum_{n=0}^{N-1} |\bar{u}[n]|^2 \tag{4.1.12}$$

another physical interpretation is added to the Fourier series, stating that the average signal energy or signal power is conserved while changing from time to frequency space.

The Parseval relation of a real signal is given by

$$\frac{1}{N}\sum_{m=0}^{N-1} u^2[m] = \bar{u}^2[0] + 2\cdot\sum_{n=1}^{\infty}\bar{u}[n]^2 \tag{4.1.13}$$

where each term contributes to the signal energy from frequency f_n (Paschmann & Daly, 1998). The mean energy of a signal $u(t)$ is not affected by the interval length, for example, when it is doubled to $2T$. However, the coefficients $\bar{u}[n]$ depend on the signal length, so the same energy will be spread over twice as many terms. Therefore, the Fourier coefficients are unsuitable for describing the physical contribution and the Power Spectral Density (PSD) is introduced (Paschmann & Daly, 1998), which describes the Power Spectral Density, rather than the signal energy density in the frequency domain, by

$$S_u[n] = 2T\cdot|\bar{u}[n]|^2, \quad n = 0, 1, 2, ..., N/2 \tag{4.1.14}$$

The Parseval's relation for real signals (eq. 4.1.13) then yields

$$\frac{1}{N}\sum_{m=0}^{N-1} u^2[m] = S_u[0]\cdot\frac{\Delta f}{2} + \sum_{n=1}^{\infty} S_u[n]\cdot\Delta f \tag{4.1.15}$$

The discrete values of the PSDs offer a direct physical interpretation, with the contributions to the signal energy for a frequency interval Δf around f_n being equal to $S_u[n]\cdot\Delta f$ (Paschmann & Daly, 1998).

The magnetic field data is a set of N measurements with a Δt sampling space instead of a continuous function. Consequently, the integral of the Fourier coefficients in eq. (4.1.11) is replaced by a sum, where dt is substituted by Δt, and the sampling frequency is $f_s = n/N\Delta t$, introducing the Discrete Fourier Transform (DFT) and its inverse by

$$\bar{u}[n] = \frac{1}{N}\sum_{j=0}^{N-1} u[j]\exp\left(2\pi i n j/N\right) \tag{4.1.16}$$

$$u[j] = \sum_{n=0}^{N-1}\bar{u}[n]\exp\left(-2\pi i n j/N\right) \tag{4.1.17}$$

The Power Spectral Density is expressed as

$$S_u[n] = 2\frac{N}{f_s}\cdot\bar{u}[n]^2, \tag{4.1.18}$$

for $n = 0, 1, 2, ..., N/2$, where N is the number of samples, f_s is the sampling frequency, and $\bar{u}[n]$ is the Fourier transform of the signal. The physical energy density S_u is given in units of $(nT)^2/Hz$, with the signal corresponding to a magnetic field component measured in nT and the frequency unit being Hz.

The Discrete Fourier Transform (DFT) can recognize the contributions to the signal energy for a given frequency range Δf over the entire time but is unable to capture temporal changes when switching to the frequency domain. However, the magnetic field data is dynamic in the frequency domain and cannot be assumed to be static. Therefore, the wavelet technique, which uses basis functions that are localized in both time and frequency, is introduced, allowing the correlation of the time series to be displayed. Depending on the physical process, different basis functions can be used. Sinusoidal waves with a Gaussian envelope are chosen to resolve both time and frequency equally well, defined through the Morlet wavelet

$$\Psi_0(\eta) = \pi^{-1/4}\ e^{i\omega_0\eta}\ e^{-\eta^2/2}, \tag{4.1.19}$$

where w_0 denotes the number of oscillations in a wave packet (Torrence & Compo, 1998). The Morlet wavelet will be used with the nondimensional frequency $\omega_0 = 6$ to obtain a Fourier period of $\lambda = 1.03s$, indicating that the wavelet scale is almost equal to the Fourier period. Other resulting empirical values, not further introduced, are given in Table 2 in Torrence and Compo (1998).

The convolution of the signal with the shifted and stretched versions of the wavelet yields the so-called Continous Wavelet Transform (CWT) coefficients denoted by

$$W(s,n) = \sum_{n'=0}^{N-1} \Psi^* \left[\frac{(n'-n)\delta t}{s}\right]\ x(n') \tag{4.1.20}$$

The coefficients depend on the scale parameter s of the wavelet, the position n localized in time, a non-dimensional time parameter η, and the normalized Morlet wave Ψ, which is obtained from wavelet Ψ_0 normalized to have unit energy for each scaling s. This allows comparing the CWT coefficients for the different scales and times. The scales are defined by $s_j = s_0 2^{j/N_j}$ for $j = 0, 1, ..., J$, where $N_j = 1/\delta j$ is the number of frequencies between an octave, $s_0 = 2\Delta t$ is the smallest resolvable scale and J the number of scales. The wavelet transform $W_n(s)$ for each scale and time can be converted to a wavelet power spectrum $W_n(s)^2$. This can then be transformed into a PSD by multiplying it by $2T$. The resulting PSD coefficients signify the density of physical energy for a given time and frequency. Parseval's theorem states that the total energy within the wavelet transform $W_n(s)$ is given by

$$\sigma^2 = \frac{\delta j \delta t}{C_\delta N} \sum_{n=0}^{N-1} \sum_{j=0}^{J} \frac{|W_n(s_j)|^2}{s_j} \tag{4.1.21}$$

where $C_\delta = 0.776$ is the reconstruction constant for a Morlet wavelet with $w_0 = 6$ (Torrence & Compo, 1998). The Parseval theorem is a useful tool for verifying the accuracy of the

wavelet transform, allowing for the acquisition of precise values for the physical energy density in both the time and frequency domains.

The Power Spectral Density coefficients S_n can be displayed over frequency and time, as demonstrated in Figure 4.5. The Power Spectral Density (PSD) shown in panel B

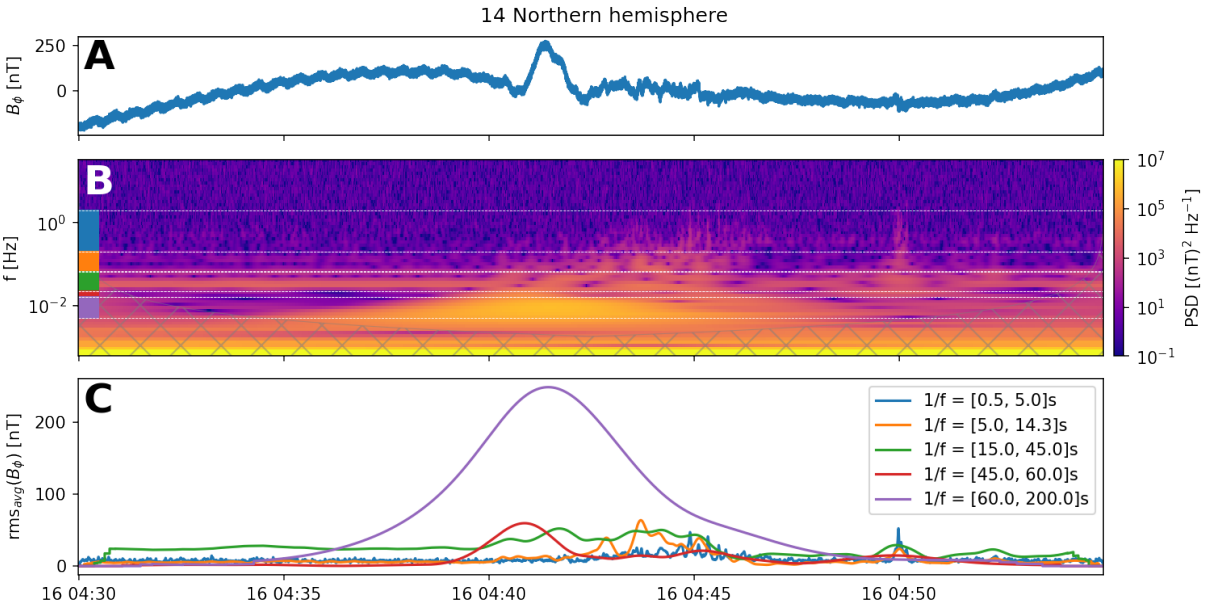

Figure 4.5: Panel A shows the B_ϕ magnetic field component used to obtain the wavelet transform, shown in Panel B, with the PSD coefficients in both the time and the frequency domains. The gray-hash region indicates the area affected by edge effects. The white dashed lines indicate the frequency boundaries of the frequency bands used to calculate the scale-averaged wavelet power, which is displayed in panel C. The frequency bands are marked on the left side of Panel B.

of Figure 4.5 is displayed for frequencies ranging from the highest resolvable frequency of 32 Hz to the smallest frequency of 1/1496 Hz, which corresponds to the length of the interval of 1500 s $\approx$ 25 min. Thus, the lowest frequencies depict the part of the signal with a wavelength nearly as long as the window size. A Cone-of-Influence (COI) is introduced to address this, marked by the gray-hashed region in panel B. This region is determined by the e-folding time $\tau(s) = \sqrt{2}s$ of the Morlet wavelet amplitude for each scale s. The COI is defined by $x_{COI}(s) = \lambda/\tau(s)$ with the Fourier wavelength $\lambda = \frac{4\pi s}{w_0+\sqrt{2+w_0^2}}$ and denotes the area where the side lobes of the Morlet wavelet are greater than e^{-1}. To avoid further edge effects, the signal is padded with zeros up to the next power of two. Additionally, a pre-whitening and post-darkening routine is applied. The prewhitening process involves an application of the wavelet transform to the increment time series of the data given by $b(t,\tau) = B(t+\tau) - B(t)$, where τ denotes the time increment of the series. This eliminates any large-scale trends or changes in the data. After performing the wavelet transform, the post-darkening process must be applied, where the PSD is multiplied by the factor $(4\pi \sin^2(\pi f \Delta t))^{-1}$ to ensure energy conservation according to Bieber et al. (1993). All three mechanisms are considered to minimize any edge effects in the wavelet transform,

yet the COI needs to be addressed when interpreting the wavelet power. For the following wavelet transform calculations, the wavelet was calculated in expanded time ranges to minimize the influence of the edges on the COI. The wavelet spectra only demonstrate a portion of the wavelet transformation, with the COI limited to frequencies mostly below 1×10^{-3} nT.

As shown in panel A of Figure 4.5, the time signal is highly variable throughout the time window. A large amplitude variation occurs at 04:42, whereas smaller amplitude changes occur throughout the other times. It cannot be deduced if small-scale fluctuations align with large-scale changes, only considering eye inspection. Therefore, the scale-averaged wavelet power is calculated for different frequency bands. A horizontal slice through the power spectral densities provides the average power over a range of frequencies or scales and is thus defined as the scale-averaged wavelet power between scales s_1 and s_2:

$$\bar{S}_n = \frac{\delta j \delta t}{C_\delta} \sum_{j=j_1}^{j_2} \frac{S_n(s_j)}{s_j} \tag{4.1.22}$$

From Parseval's theorem eq. (4.1.21), we can infer that the scale-averaged wavelet power $\bar{S}_n$ is the time series of the average variance in a specific frequency range (Torrence & Compo, 1998), the root-mean-square (rms) is determined by the square root. The comparison of the average wavelet powers can be used to observe the contribution of different frequency bands to the overall power. An example of the scale-averaged wavelet power through different frequency bands is shown in panel C of Figure 4.5. One can differentiate between areas with considerable amounts of minor fluctuations from PSD of the frequency bands ranging from 0.5 Hz to 14.3 Hz, which is represented by the orange and blue lines. Both lines show enhanced rms for around $04:45$. The great magnetic surge is notable through the frequencies from 1/60 Hz to 1/200 Hz, where also the amplitude $\approx$250 nT can be denoted from the rms. The impact of the spacecraft rotation is visible in the frequency band from 1/15Hz to 1/45Hz, especially at times before the great magnetic surge. The power provided by the eddy currents originating from the spacecraft's rotation is also clearly visible by eye inspection in panel B, where a horizontal bright line is observable at 0.03 Hz. Thus, the scale-average power spectra provide significant insight into the individual contributions of the different frequency bands to the signal power.

A vertical cut through specific regions of the wavelet graph gives the local spectrum. Time averaging over a certain period between index n_1 and n_2 can provide the corresponding power spectral wavelet spectrum given by

$$\bar{S}_n(s) = \frac{1}{n_2 - n_1 + 1} \sum_{n=n_1}^{n_2} S_n(s) \tag{4.1.23}$$

Time-averaged wavelet spectra for different time bands of Perijove 5 are shown in Figure 4.6.

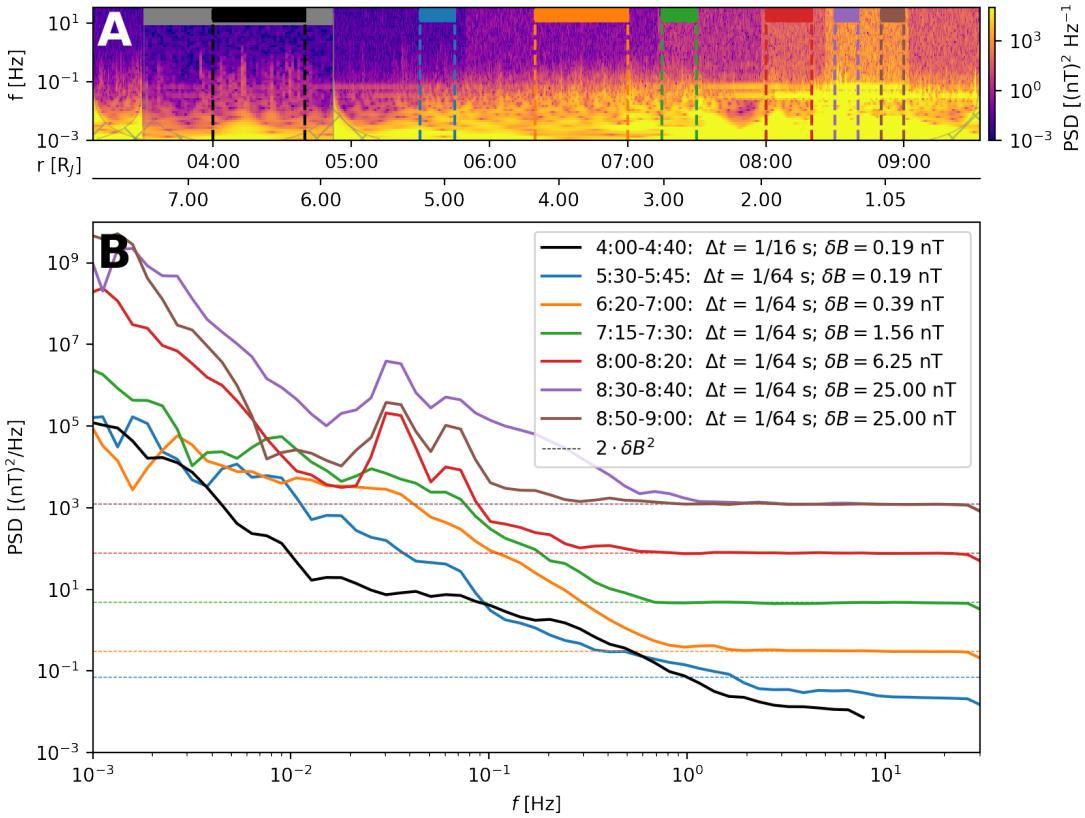

Figure 4.6: The wavelet spectra of the northern flyby of Fifth Perijove are displayed over a wide temporal range. All the different digitization levels are visible. The lower part of the graph shows the time-averaged wavelet spectra, with the gray dashed lines indicating the corresponding digitization levels.

We can observe that the power spectral densities of the different time spans are limited in resolving the higher frequencies. All spectra seem to be limited by a different lower limit indicated by the gray lines in Figure 4.6 following $2 \cdot \delta B^2$ of the corresponding time intervals. The digitization level results from the processing routine of the FGM data, where a 16 bit analog to digital (A/D) converter is used. The converter provides the data with a resolution of $\pm 1/2 \cdot 2^{16} = \pm 32768$ steps for each dynamic range (Connerney et al., 2017, sec. 3). These dynamic ranges are given at six levels i each with a dynamic range up to 2^i kG and thus by a resolution of $2^i/2^{16}$ kG depending on level i. The digitization levels range from 0.05 nT to 25.0 nT, which corresponds to the magnetic field amplitudes of 0.0160 Gauss to 16.385 Gauss, or of 1600 nT to 16.385×10^5 nT (Connerney et al., 2017). The Power Spectral Density is restricted by the square of the quantization noise, which is caused by the digitization of the A/D converter. Generally, the mean Power Spectral Density increases with increasing magnetic fields, and the transition to frequencies dominated by the quantization noise is usually around ≈ 0.5Hz. Therefore, amplitude changes with a wavelength less than 2 s are not resolvable. However, the lowest digitization levels can observe amplitude changes on smaller wavelengths down to 0.3 s. Here, the power spectral densities are at mean still greater than $0.1\,(\mathrm{nT})^2/\mathrm{Hz}$, exceeding the lower

quantization noise of 0.072 nT. The correlation of the quantization error δB with the lowest resolvable Power Spectral Density PSD_{min} is seen in panel A of Figure 4.7, where the relation $PSD_{min} = \delta B^2 \cdot 2$ envelopes the minimum resolvable PSDs. The strength of

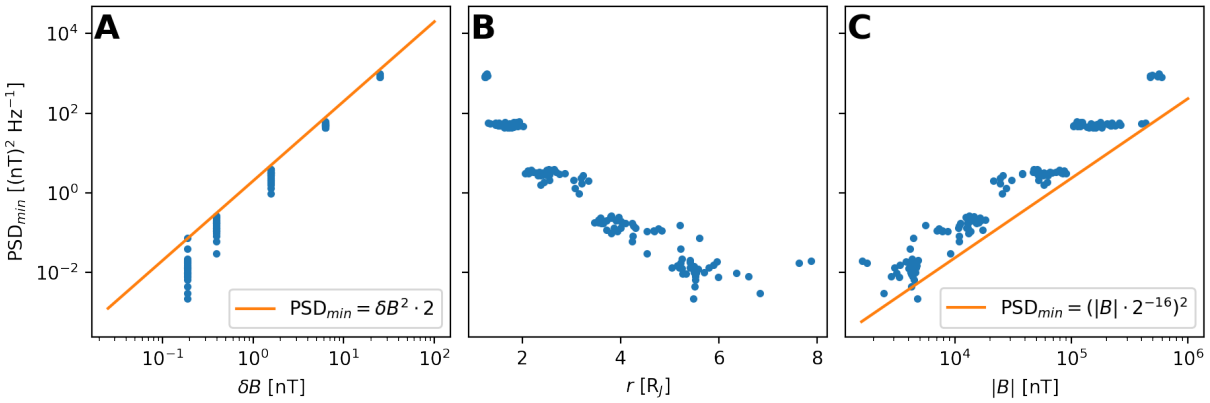

Figure 4.7: The minimum resolvable Power Spectral Density PSD_{min} for each digitization level (panel A) and its correlation to the total magnetic field strength (panel C) and the radial distance to Jupiter (panel B). The orange slopes indicate the relation of the x and y parameters.

the magnetic field is associated with the least resolvable Power Spectral Density PSD_{min} through equation $PSD_{min} = (B \cdot 2^{-16})^2$, which is illustrated in panel C. This, in turn, is associated with the radial distance to Jupiter, as seen in Panel B. Consequently, radial distances less than 5 R_J are unlikely to be able to detect small-scale fluctuations with wavelengths less than 2 s. Thus, only nobservations of a greater radial distance can resolve the entire frequency range.

4.1.5 Juno Ultraviolet Spectrograph (UVS)

The Juno Ultraviolet Spectrograph (UVS) is one of the instruments mounted on the Juno spacecraft. It is designed to analyze ultraviolet light emitted in Jupiter's polar regions. By studying the Jovian aurora in the ultraviolet range, scientists can gain valuable insight into the composition and dynamics of Jupiter's upper atmosphere and magnetosphere. The UVS can detect emissions from specific gases and ions in Jupiter's aurora, as it can capture wavelengths between 68 and 210 nanometers (Gladstone et al., 2017). Each time the spacecraft passes close to the polar regions, it offers a close-up view of the polar emissions, providing a detailed look at its structure, brightness, and dynamics.

A comprehensive method has been introduced by Bonfond et al. (2021) to obtain an image covering the entire polar region. They provide detailed images of the auroral emission. This routine uses the observation from the UVS through a slit in the shape of a dog bone, which can be shifted by ±30° with the help of a scan mirror, allowing for the targeting of particular areas during the rotation of the spacecraft. In the data processing stage, UV photons are distinguished from noise caused by penetrating particles (Bonfond

et al., 2021). The UV photons are then mapped onto an ellipsoid in the shape of Jupiter, located 400 km above the 1-bar level. Each detection event is projected onto this ellipsoid, forming quadrilaterals based on the four corners of the field-of-view element. During each spacecraft rotation, each slit updates the UV image of the polar regions. These quadrilaterals, weighted counts, and exposure time contribute to building the auroral map. To enhance the completeness of the auroral map, images of the auroras are assembled using a weighted sum of consecutive spins, with more weight given to recent spins (Bonfond et al., 2021). However, due to the spacecraft's spinning motion, there can be uncertainties in the exact timing and duration of transient events, with temporal knowledge gaps of 30 seconds at best. Multiple rotations are necessary to acquire a completely resolved polar region. This process takes around 50 minutes. Therefore, the UVS image provided by Bonfond et al. (2021) may not accurately reflect the observed area's current state. However, it does provide a good overview of the UV emission's morphology for that particular day, as is exemplarily shown for the first perijove in Figure 4.8 panels A and D.

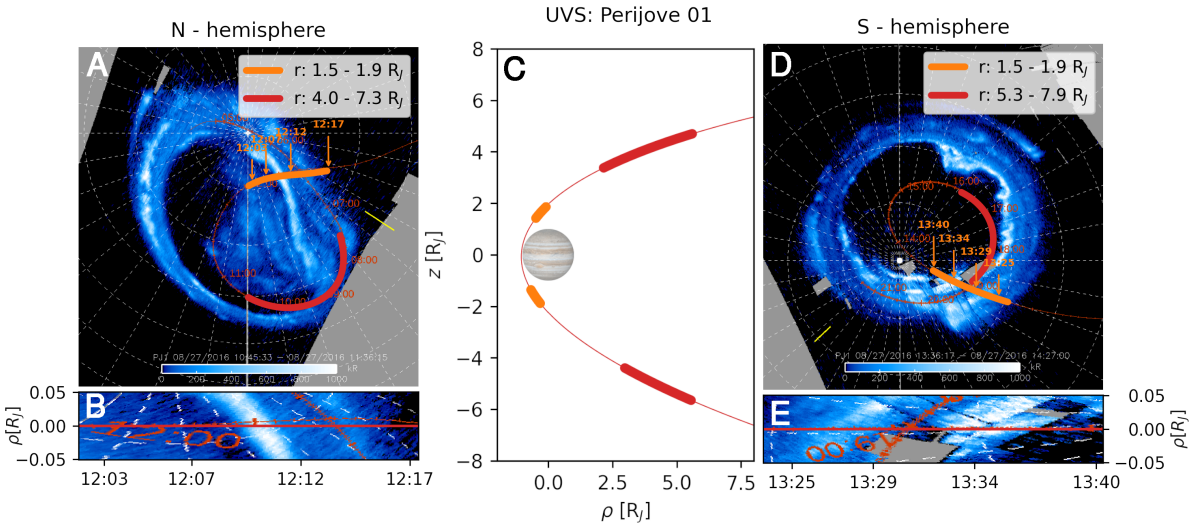

Figure 4.8: Overview of the flight trajectory of the first perijove for SysIII coordinates, as shown in panel C. Radial distance is calculated by $\rho = \sqrt{x^2 + y^2}$. The spacecraft's location is mapped onto the ionosphere and marked with red lines on the left and right sides of the UVS panels. The UVS images, adapted from Bonfond et al. (2021), are shown for the northern hemisphere (A) on the left and the southern hemisphere on the right side (D). The lower parts (B and E) show the UVS image slice along the flight trajectory for both hemispheres, where Juno crosses the main emission zone at times marked by the orange lines in the top plots. The perpendicular ρ extend in panels (B and E) are expressed in jovian radii.

By studying these UVS images of the different perijoves from Bonfond et al. (2021), one can observe considerable variations in the shape, location, and pattern of the aurora. For instance, near the orange-marked observation times in panel A, thin lines partially encircle the oval shape of the aurora. During other perijoves, the same region displays patchy structures with no distinct form. This diversity in auroral patterns is nearly visible in every quadrant of the aurora in the northern and southern hemispheres. Panel C shows

an example of auroral patterns without distinct forms in Figure 4.8. Therefore, it is very interesting to consider the patterns of the UVS images mapped to any magnetic or intense particle pattern.

In order to link any in situ measurement of the Juno spacecraft with the relevant UVS features, we track the location of the spacecraft along the magnetic field lines onto the ionosphere using the community code (Wilson et al., 2023). The tracing code uses internal and external magnetic field sources described by JRM33 and Con2020. This software can be used to trace the paths of field lines from any point in the magnetosphere of Jupiter to, for instance, the ionosphere or the equator. It can also be applied to other planets. The code uses starting coordinates and initial step size, and it will trace a path until either the current position reaches Jupiter or the maximum number of steps is reached. We then used the traced footprints to calculate the flight trajectory within the image coordinates. Parallel lines are established using the orthogonal line element, forming a curved rectangular region along the flight trajectory in the image coordinates. The pixels along these lines are extracted and plotted as an uncurved rectangle plot, with the timeline as the x-axis and the distance ρ from the line of flight in the atmosphere in the y direction (see panels B and E in Figure 4.8). The routine has been tested using a standard PAL test pattern (see Figure A.7). It was determined that the best representation of the slice is obtained when the slice grid has a minimum step size of $0.0025\,\mathrm{R_J}$, which means that there are at least 40 lines per $0.1\,\mathrm{R_J}$.

It is important to note that because of the curvature of the flight trajectory, the UV structures are likely to be bent into a rectangular shape. This means that the image slices are only helpful in mapping the flight trajectory onto the UV radiations. The extension of the flight trajectory is only provided to give a better view of the surrounding areas. The slices are not reversed but rotated in the same direction as the flight path. The resulting image slices of the UVS directly compare to the magnetic field and electron intensity structures. Various factors may cause discrepancies between the UVS images and the observed in situ measurements. Constructing the image throughout approximately 50 min, any in situ observation may already be related to different auroral structures, as the time variability cannot be shown. Additionally, the time frames used to create the images do not directly correspond to the observed time frames used for subsequent investigations. Lastly, tracing the field lines may not be perfectly accurate, as temporal magnetic field variations or others may occur. Therefore, the UVS slices provide a good indication of the current structures of the main emission zone but cannot precisely match any UV structure with the in situ observations.

4.2 Results

The wide range of spacecraft flyby configurations, the environment's characteristics, and the spacecraft's rotation restrict the number of flybys captured accurately by the three instruments. In particular, the spacecraft's rotation can impede the magnetometer and particle instrument. Therefore, some auroral crossings do not provide sufficient data resolution to investigate the correlation between the different instrument observations. Those crossings are listed in Table A.1.

The spacecraft's path allows multiple crossings of the main auroral emission, as demonstrated in Figure 4.8. For most flybys, the innermost radial crossing above the main emission zone occurs between a jovicentric radial distance of 1.25 R_J to 2.0 R_J in the northern hemisphere and 1.25 R_J to 3.0 R_J in the southern hemisphere. The flightpaths of these regions are marked in orange in Figure 4.8 for both hemispheres of the fifth flyby. The crossings last for 15 minutes in the north and 20 minutes in the south, during which the planet rotates about ≈10° below the spacecraft. The red lines within the figure indicate the second period of the flight path for each hemisphere. Here, at greater radial distances, the spacecraft location again maps to the main emission zone. These crossings occur between a radial distance 1.6 R_J to 7.5 R_J in the northern hemisphere and 2.8 R_J to 8.2 R_J in the southern hemisphere. The average time length is much longer here, with an average of around 111 min, because the movement of the spacecraft is more aligned with the magnetic field lines.

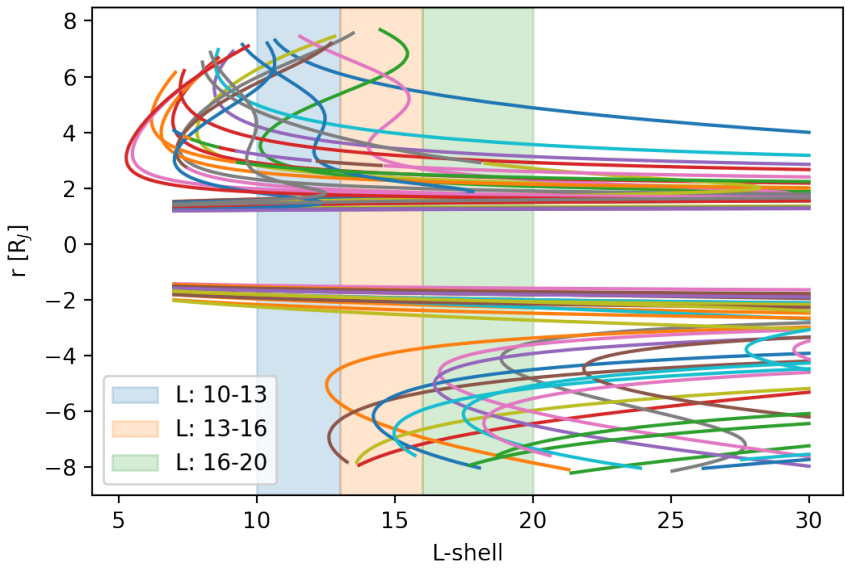

Figure 4.9: The coverage of radial distances and L-shells for the first 20 perijoves. The radial distances are given with positive values for the northern and negative values for the southern hemisphere. Different L-shell regions are marked to resemble the different auroral regions, with DifA in blue, ZI in orange, and ZII in green.

Meanwhile, Jupiter rotates about ≈60° below the spacecraft, resulting in a more pronounced azimuthal motion along the main emission zone. Figure 4.9 illustrates the radial and L-shell coverage of the various flybys. When observing radial distances below $3\,R_J$, the southern hemisphere resolves larger L-shells than the northern hemisphere. Therefore, observations at radial distances greater than $2\,R_J$ rarely show a perpendicular fly through all three regions, DifA, ZI, and ZII, marked as blue, orange, and green areas in Figure 4.9, respectively. Some flybys even do not cross ZI or ZII and move along the oval shape, staying poleward or equatorward of ZI and ZII. The northern hemisphere will show the equatorward boundary of the main emission zone, whereas the southern hemisphere can identify the poleward boundary of the main emission zone. Flybys over the polar cap and thus not resolving the main emissions are primarily seen in the southern hemisphere, as listed in Table A.1. Here, magnetic variations, apart from fluctuations caused by noise, are not perceptible during these auroral crossings. The electron intensity is also extremely low, with either none or a few detected per second. The ultraviolet images show either faint or no intensity, indicating that the spacecraft is in an area with no evidence of accelerated auroral particles.

All perijoves, listed in Tables A.2a and A.2b, are observed at radial distances smaller than $3\,R_J$ with a perpendicular flyby through magnetic field lines with L-shell values from 8 to 20. Therefore, these perijoves can distinguish the three regions of the main emission zone, DifA, ZI, and ZII. Most of these perijoves are observed with an adequate pitch angle coverage and magnetic field resolution, thus providing an appropriate foundation for comparing the observations from all three instruments. Observations of these accurately resolved perijoves can be partially complemented by the perijoves listed in Table A.2c, which lacked the necessary resolution to encompass the entire range of electron pitch angle space, making it impossible to interpret the electron intensity data. Still, the correlation between UV emissions and magnetic field variations is observed.

Despite the limitations of the polar crossings at higher altitudes, some of these time spans expand the observation of the auroral region. Due to the nearly azimuthal flight path of the spacecraft at higher radial distances, only half of the perijoves offer the opportunity to observe the different zones of the main emission zone. Additionally, half of the remaining time intervals do not have full pitch angle coverage, as listed in Table A.3b, and can only be used to analyze magnetic field fluctuations and their correlation with UVS observations. Therefore, only one-quarter of the crossings at higher altitudes, listed in Table A.3c, allow interpretation of the pitch angle electron distribution, the magnetic field components, and the UV emissions over the different auroral regions. However, as the magnetic field decreases with $B \sim 1/r^3$, the magnetic field components at these larger distances can be digitized with a resolution of 1 nT, providing a more detailed view of the magnetic field variations. In comparison, magnetic field components at radial distances less than $3\,R_J$ are usually digitized with a minimum difference of 25 nT.

Together, these auroral crossings at radial distances from 1.25 R_J to 8.2 R_J offer a comprehensive qualitative analysis of the relationship between electron distributions, magnetic field fluctuations, and UV emissions across the three different regions, summarized in the following sections.

4.2.1 Diffuse Aurora at low Latitudes

First, the DifA region is found at small L-shells between 10 to 13 marked by the orange bar at the top of Figure 4.10. Pancake distributions dominate the electron intensities throughout these times at both low and high altitudes. With empty loss cones in the pitch angle distribution of electrons, the energy flux of trapped electrons between the loss cones ranges from 10 mW/m^2 to 100 mW/m^2 at radial distances of $\approx$1.3 R_J, as shown exemplarily in Figure 4.10. The UVS images show dim and blurred intensities without a clear structure. The azimuthal magnetic field exhibits minimal variation, usually similar to the amount of noise. These areas appear to have very low auroral activity.

Occasionally, auroral beams of mostly downward-accelerated electrons fill the downward LC, reaching higher energy fluxes of $\approx$100 mW/m^2, both outside and inside the downward loss cone, as seen in Figure 4.10 (G) between 16:33-16:37. Consequently, there is a diffuse auroral display with a consistent brightness of approximately 200 kR, and occasionally some patchy UV glows. However, these structures are less luminous than other areas identified by higher L-shells. Simultaneously, these regions are dominated by small-scale magnetic field fluctuations at periods ranging from 0.5 sec to 60 sec with rms of 50 nT to 100 nT. Thus, the wave-particle interaction may accelerate and scatter trapped electrons to higher pitch angles, generating diffuse auroras at Jupiter.

It is possible to observe specific areas where the pancake regions transition into pitch angle distributions that are almost isotropic, hence with uniform electron intensities regardless of the pitch angle. The spacecraft moves along an L-shell of around 8 or less, entering the radiation zone of Jupiter and its scattered electrons. The transition from diffuse auroral regions to regions with isotropic distributions is seamless, as seen in Figure 4.11. Generally, L-shell values less than 8 are dominated by isotropic distributions, while those greater than 11 usually display empty loss cones unless specific auroral beam structures are present. This leads to a transition zone from DifA to ZI, observed for many perijoves. Here, it appears that between both zones, a region of pure pancake distributions with empty loss cones is present, surrounded by field-aligned electron beams at higher L-shells and diffuse auroral beams at smaller L-shells, as seen in Figure 4.11 at 04:43, marked by the gray dashed lines. Therefore, dim UV emissions are directly between the strong, intense auroral emissions from ZI and the blurry diffuse aurora, separating the two zones.

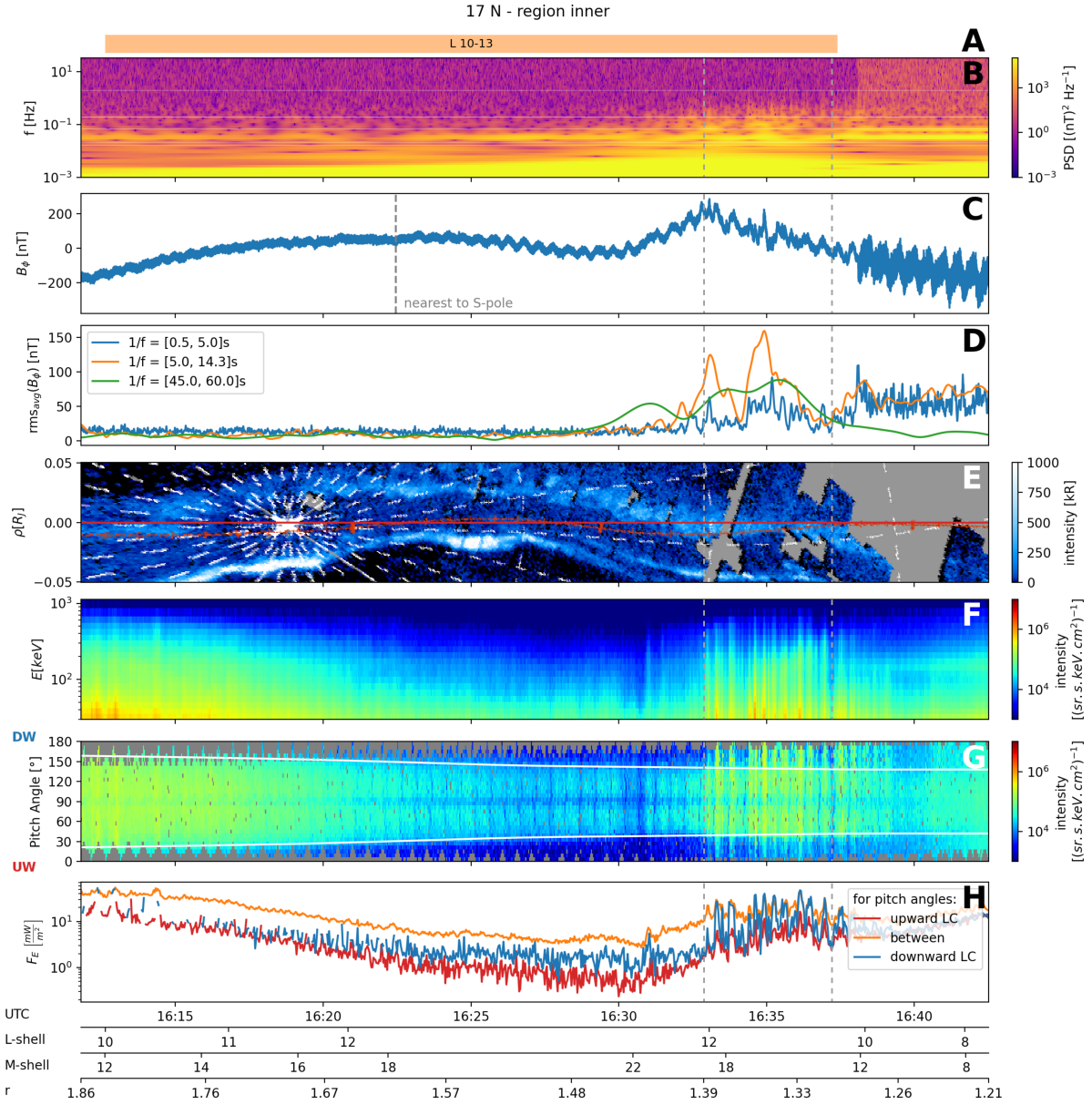

Figure 4.10: Overview of the instrument data from Perijove 17, which crossed the northern hemisphere at altitudes lower than $2\,\mathrm{R_J}$. Panel (A) displays the L-shell value color-coded in red, blue, and orange, representing the three expected auroral regions: ZII, ZI, and DifA, respectively. (B) Wavelet spectrum of the B_ϕ component, as shown in (C). The magnetic field components were obtained from the raw magnetic field data after subtracting the JRM33+Con81 model. Panel (D) shows the rms averaged between the frequency ranges, labeled in the legend. Panel (E) adds the UVS observations projected along the Juno flight trajectory adapted from Bonfond et al. (2021). Panels (F) and (G) provide the electron intensity distribution through energy and pitch angles, respectively. The white line in panel (G) corresponds to the loss-cone boundary, which was calculated from the ratio between the magnetic field at the spacecraft and the magnetic footprint in the atmosphere. Lastly, panel (H) provides the mean energy flux for each resulting pitch angle in the loss cones and between.

4.2.2 Strong Electron Beams connected to Auroral Arcs

Second, ZI region is found at L-shells between 13 to 16 marked by the blue bar at the top of Figure 4.11. Small-scale magnetic field fluctuations are hardly seen through this region. Moreover, strong magnetic field deviations are observed from a few nT to several hundreds of nT. These substantial deviations are mostly mapped to intense auroral lines in the UVS images as seen in Figure 4.11 (D), marked by the black vertical dashed lines.

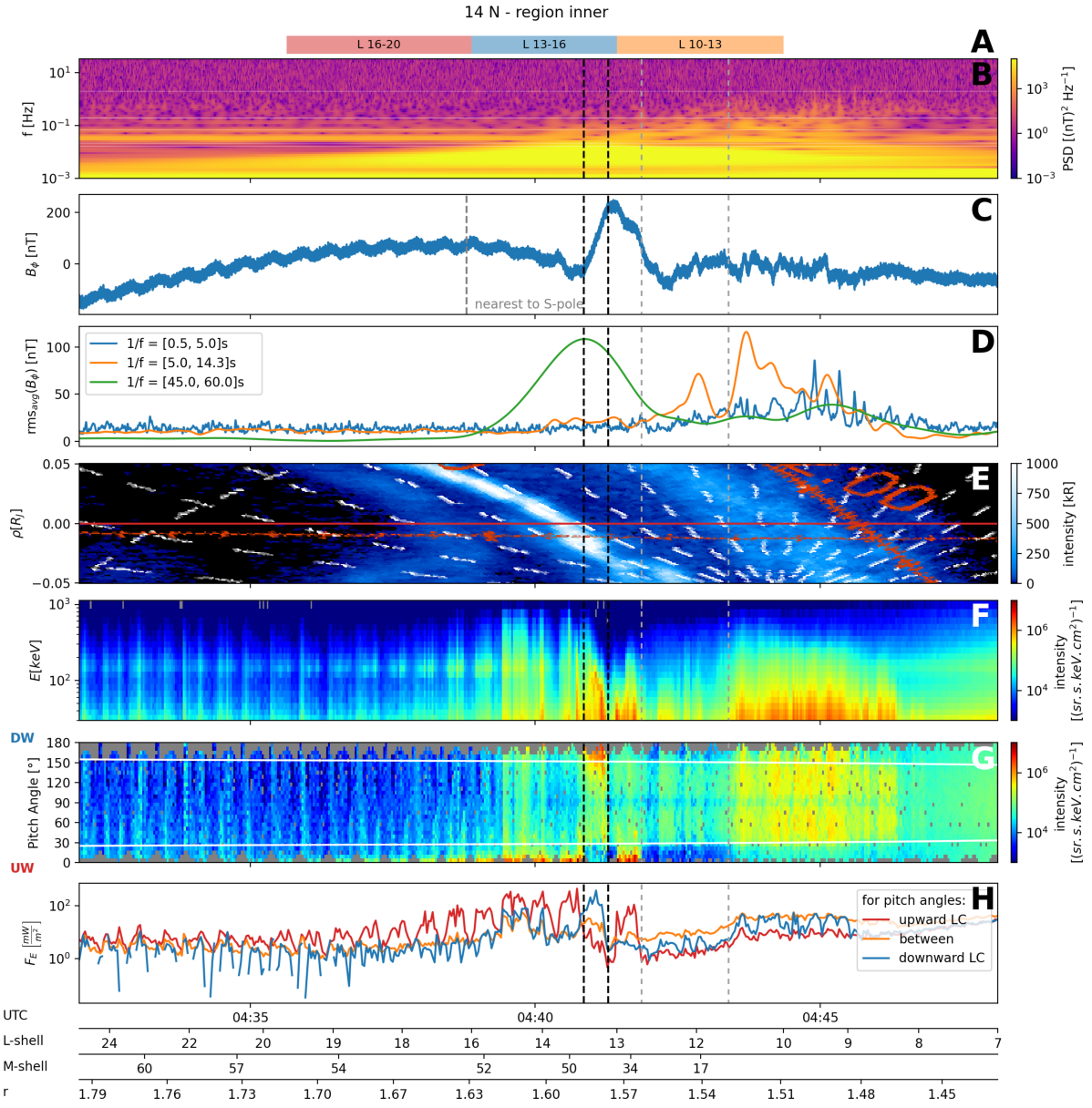

Figure 4.11: This figure gives an overview of the instrument data from Perijove 14, which passed through the northern hemisphere at altitudes lower than $2\,R_J$. Further details for each panel are provided in the caption of Figure 4.10. The vertical dashed black lines indicate regions of intense aurora and correspond to strong magnetic field gradients.

For perijove 14, the magnetic field B_ϕ increases by 260 nT in a span of 45 sec, and decreases by 300 nT in a span of 60 sec. The positive slope is above the UVS line, whereas

the negative slope maps to a dim region. The electron energy spectra show a mono-energetic peak with high electron intensities of 100 keV at 04:41. Simultaneously, the downward loss cone is filled with electrons, whereas the upward cone is empty. Hence, the electrons are accelerated downward mostly with a specific energy. This electron energy feature, also known as inverted V structure, is commonly associated with a static electric potential, accelerating electrons in one direction to a specific energy. The spacecraft's passage through the potential could cause the magnetic positive gradient, experiencing a curl of $\mathbf{B}$ due to the upward current generated by the potential, as further introduced in section 4.1.3. Here, the negative gradient 04:42 in Figure 4.11 would correspond to a downward current that would accelerate electrons mostly upward with a specific energy. Indeed, the pitch angle distributions demonstrate a filled upward loss cone but a wide range of energy levels with high intensities, described as broadband distribution. These unidirectional pitch angle distributions are also found in many other perijoves. All of them are accompanied by either a positive or negative magnetic field gradient in the azimuthal component, which is in line with the expected direction of the current, either downward or upward. Despite this, not all magnetic field variations with a gradient of more than 50 nT result in unidirectional electron pitch angle distributions or increased intensities. For example, the first perijove crosses the northern auroral region with a strong magnetic field variability of 200 nT at 12:12, but the loss cones of the pitch angle distribution remain empty at that time; see Figure A.4. The UVS images simultaneously show an intense auroral line, indicating auroral activity. Hence, it is essential to remember that the time lag between the different measurements may distort the comparison of the various readings from different instruments. Electrons aligned with the field may have already been absorbed in the atmosphere, resulting in the intense auroral line penetrating the aurora. Therefore, the spacecraft may not be able to detect electrons that have already traveled to smaller radial distances than the spacecraft's location, penetrating the atmosphere.

Nevertheless, unidirectional pitch angle distributions are commonly seen when the spacecraft crosses intense auroral regions, especially when they are thin in nature. Most unidirectional pitch angle distributions are in the downward direction, sometimes showing mono-energetic structures, as seen in Figure 4.11. The auroral crossings at greater radial distances also show mostly unidirectional magnetic field gradients aligned with intense auroral UV emissions matching upward currents. Those magnetic field gradients are smaller than those at low altitudes, usually observed with amplitudes ranging from a few tens of nT to no more than 100 nT. It is important to recall from section 4.1.3 that, due to the Juno flight trajectory, the direction of the magnetic field gradient created by a field-aligned current is opposite at the greater distant crossings than at close radial crossings. Hence, negative magnetic field gradients will correspond to upward-directed currents, causing electrons to be accelerated downward. At both low and high altitudes, most observations show magnetic field gradients accompanied by either downward- or

upward-filled electron loss cones and unidirectional magnetic field gradients corresponding to the direction of the expected upward or downward currents, respectively.

Bidirectional pitch angle distributions are often observed in the transition from upward to downward-filled cones and vice versa. These distributions show a comparable amount of energy flux in both cones, which is higher than outside of the cones. Interestingly, a bidirectional distribution is often observed when the magnetic field has a negative gradient, indicating a downward current but showing an equal amount of upward and downward accelerated electrons. This contradicts the idea that a static potential mainly accelerates the electrons since the electrons move in both directions independent of the possible current direction, determined from the magnetic field gradient. These features are located right above very intense auroral UV regions, as seen in Perijove three at 17:38 in Figure A.2. Despite a significant increase in the number of particles that are accelerated upward, there is also a considerable amount of particles that are accelerated downward. Therefore, even the most intense auroral emission can be caused by bidirectional acceleration in an area connected to downward currents, indicated by positive magnetic field gradients.

In conclusion, the observations made indicate that the regions ZI have intense magnetic field gradients of several 100 nT observed with intense UV emissions. In particular, downward-accelerated particles are located along the field lines, mapping to the intense, thin main emission lines. Mono-energetic energy distributions and strong positive magnetic field gradients indicate a downward current observed by the spacecraft. Negative magnetic gradients tend to be associated with unidirectional pitch angle distributions, which are linked to dim UV emissions. On the other hand, negative magnetic gradients with bidirectional pitch angle distributions are related to intense UV emissions.

Observations of the perijoves, which were not detailed enough to cover the full range of electron pitch angle space, still provide enough data to confirm the relation between the UV emissions and the changes in the magnetic field made before. Accordingly, positive magnetic field gradients are seen in areas with strong UV line emissions at low altitudes. In contrast, negative gradients are associated with patchy UV emissions or no emission. Accordingly, negative magnetic field gradients with intense UV emissions at higher altitudes are observed.

4.2.3 Bidirection and Upward Electron Distributions at high Latitudes

The transition from ZI to ZII is smooth and sometimes not distinct, but approximately marked by the red bar at the top of Figure 4.11 defined from L-shell 16 to 20. In the transition region, primarily bidirectional pitch angle distributions are observed. The energy distributions associated with this phenomenon are broad, with evidence that electrons with energies as high as 1 MeV penetrate the detectors, as indicated by the minimum ionizing

effect at 150 keV. These distributions are observed next to the strong unidirectional pitch angle distributions mapping to intense UV emissions. Despite the bidirectional acceleration of the electrons, only very dim UV emissions are observed within. Surprisingly, neither small-scale magnetic field fluctuations nor larger magnetic field gradients are observed. Acceleration in both directions may be driven by small fluctuations that are too faint to be detected in the inner radial areas.

Two distinct kinds of observations are present. A subset of perijoves, as listed in Table A.2a, exhibits minimal electron intensities for greater L-shells. Most of the electrons seen here are in the upward loss cone with energy fluxes of only a few milliwatts per square meter. The magnetic field variations are insignificant, and the ultraviolet radiations are dim. The other subset of perijoves, as listed in Table A.2b, show auroral signatures even through the higher L-shells. The UV emissions show intensities that are patchy with high intensities or blurry with intermediate intensities. The magnetic field shows mainly negative gradients of several 100 nT, corresponding to a downward current. Only perijove 20 has magnetic variations of less than 50 nT, yet it also displays faint ultraviolet emissions. Electron distributions in these areas are comparable in intensity to those of ZI. However, the pitch angle distributions are usually bidirectional, sometimes almost isotropic, or unidirectional in an upward direction. At the same time as the electron beams appear, negative magnetic field gradients, accompanied by intense UV radiation, are observed. As already observed in ZI, if the pitch angle distributions are bidirectional, this UV radiation is present (see Figure A.6 at 06:58), but when the electrons only fill the upward loss cone, nearly no UV emissions are visible (see Figure A.5 at 09:47).

4.2.4 Small Scale Magnetic Field Fluctuations

For all perijove observations, magnetic field variations on short temporal scales of a few seconds at smaller or larger radial distances were observed at L-shells smaller than 13, where mainly pancake distributions and some diffuse auroral beams were present. The amplitudes of the magnetic field variations ranged from 30 nT to 600 nT at low altitudes (less than 2 R_J) and from a few nT to several tens of nT at high altitudes (greater than 2 R_J). The typical periods ranged from a few seconds to a few minutes. Most low-altitude crossings did not observe small-scale fluctuations in ZI and ZII. Nevertheless, particular powerful electron beams could not be correlated to any alteration in the magnetic field, thus providing no insight into these intense beams' acceleration mechanisms. In a few cases, the magnetic field showed small-scale fluctuations of several seconds that directly contributed to intense emissions above the main emission zone, as seen in the Juno Ultraviolet Spectrograph (UVS) observations, Figure 4.12 (B).

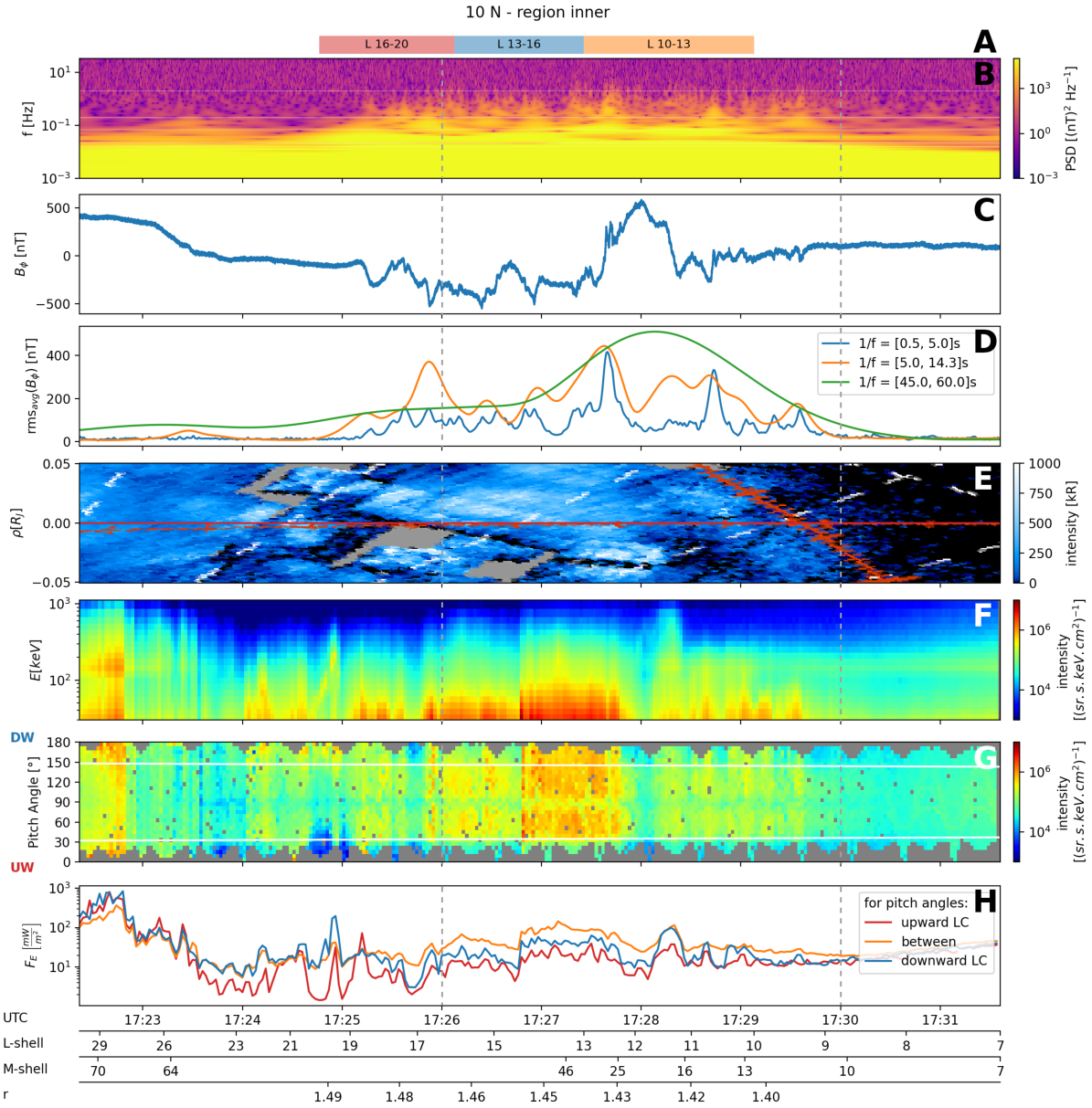

Figure 4.12: This figure gives an overview of the instrument data from Perijove 10, which passed through the northern hemisphere at altitudes lower than $2\,\mathrm{R_J}$. Further details for each panel are provided in the caption of Figure 4.10.

Unfortunately, the electron distribution during this perijove was not fully covered, especially the upward loss cone. Nevertheless, the upward loss cone seems empty, as seen at times between 17:26 - 17:30 in Figure 4.12 marked by gray lines, and the downward loss cone and outside of the cone are filled. The intensities in the downward loss cone are similar to those at intermediate pitch angles, suggesting that the auroral feature is more diffuse than that of a field-aligned beam. Interestingly, at 17:25, the electron energy distribution displays an inverted V structure. Yet, no magnetic gradients are detected, even though the pitch angle distribution indicates the presence of a downward electron beam. This means that no particular static potential, which a strong magnetic field gradient would imply, is present at this altitude. No alterations in the magnetic field are seen when downward

or bidirectional electron beams are present. It is conceivable that the resolution of the magnetic field components during this period is not adequate to reveal any clues to an acceleration mechanism. This could be due to either the spacecraft's position relative to an acceleration region or the restrictions of the spacecraft's instruments.

Only six other perijoves show small-scale variations for higher L-shells that map to intense UV emissions at these small radial distances. The amplitudes of the fluctuations are very small, almost equivalent to the noise level of 25 nT. The times listed in Table A.2 have a high degree of noise at these small radial distances due to the powerful background magnetic field, which directly affects the precision of the digitization. Consequently, when Juno passes through the main emission area at a greater distance than $3\,R_J$, it experiences lower noise levels, making it possible to detect smaller amplitudes more likely to be associated with small-scale fluctuations. More specifically, the noise level reaches amplitudes less than 0.1 nT. Throughout these times, small-scale fluctuations are also visible along the higher L-shells with a typical rolling rms of a few nT between 0.5 sec to 15 sec window size. Especially from the fifth perijove shown in Figure 4.13 (B) (3:10-4:50), we can clearly see that the small scale fluctuations range down to temporal scales of 0.5 s when the noise level is low with 0.024 nT. Rms values at 0.5 s to 5 s is about 2 nT to 10 nT, which is well below the typical noise level for radial distances $<3\,R_J$. The small-scale fluctuations observed with pancake distributions provide a higher rms at a 8 s to 20 s scale so that those fluctuations are still visible with high noise levels. Another example where small-scale fluctuations are directly linked to very intense UV emissions and bidirectional electron beams is shown in the appendix in Figure A.3 between 10:30-11:30.

The average power spectral densities were determined for the different digitization levels through the northern flyby 5 to display the limits within each digitization level. Five different regions display the power spectra for each digitization level, as illustrated in Figure 4.14. Each colored line in panel (B) corresponds to one period related to the different digitization levels, which is indicated by the dashed horizontal lines in the corresponding color. The corresponding periods are labeled above the power spectra in panel (A). The red and green lines correspond to the same digitization level, but one period is assigned to the main emission zone and one to the zone equatorward of the main emissions. The black line indicates the lowest digitization level, where small-scale fluctuations can be seen even in the higher L-shells. The Power Spectral Density is resolved down to $0.07\,(\mathrm{nT})^2/\mathrm{Hz}$, which corresponds to frequencies of a few Hz. The importance of the power provided on very short time scales is seen when the black spectral slope extends to frequencies up to 2 Hz, reaching power densities of less than $1\,(\mathrm{nT})^2/\mathrm{Hz}$. However, these power spectral densities are too small to be detected with digitization levels higher than 0.391 nT. On the other hand, small-scale fluctuations observed at smaller L-shells provide two orders of magnitude higher power spectral densities, reaching almost $100\,(\mathrm{nT})^2/\mathrm{Hz}$ at frequencies of 0.03 Hz, as shown by the orange and blue lines in Figure 4.14. Therefore, times with

digitization levels higher than 6.25 nT are unable to detect small-scale fluctuations of frequencies above 0.3 Hz.

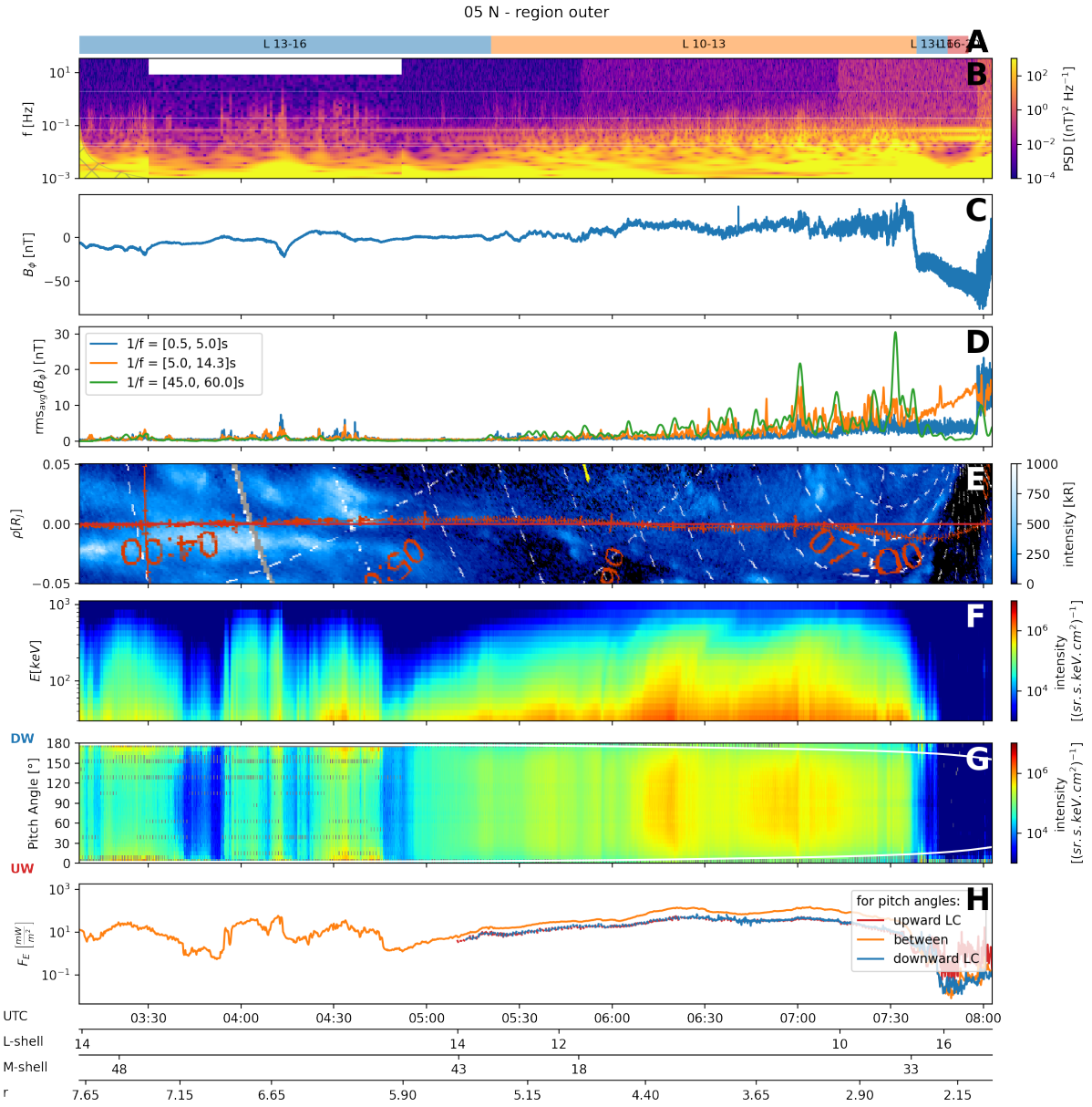

Figure 4.13: This figure gives an overview of the instrument data from Perijove 5, which passed through the northern hemisphere at altitudes higher than 2 R_J. Further details of each panel are provided in the caption of Figure 4.10.

Unfortunately, the frequencies between 0.01 Hz to 0.2 Hz are mainly dominated by magnetic field fluctuations caused by eddy currents generated by the spacecraft rotation, which have an approximate period of 30 sec corresponding to 0.03 Hz. As the eddy currents depend on the strength of the background magnetic field, the impact increases again at smaller radial distances when the digitization levels are already high. The Power Spectral Density of the eddy currents is much higher than the highest digitization level 25 nT, with power spectral densities reaching $1 \times 10^5\,(\mathrm{nT})^2/\mathrm{Hz}$. According to the fifth perijove, the MAG observations at small radial distances with less than 2 R_J distance from Jupiter do

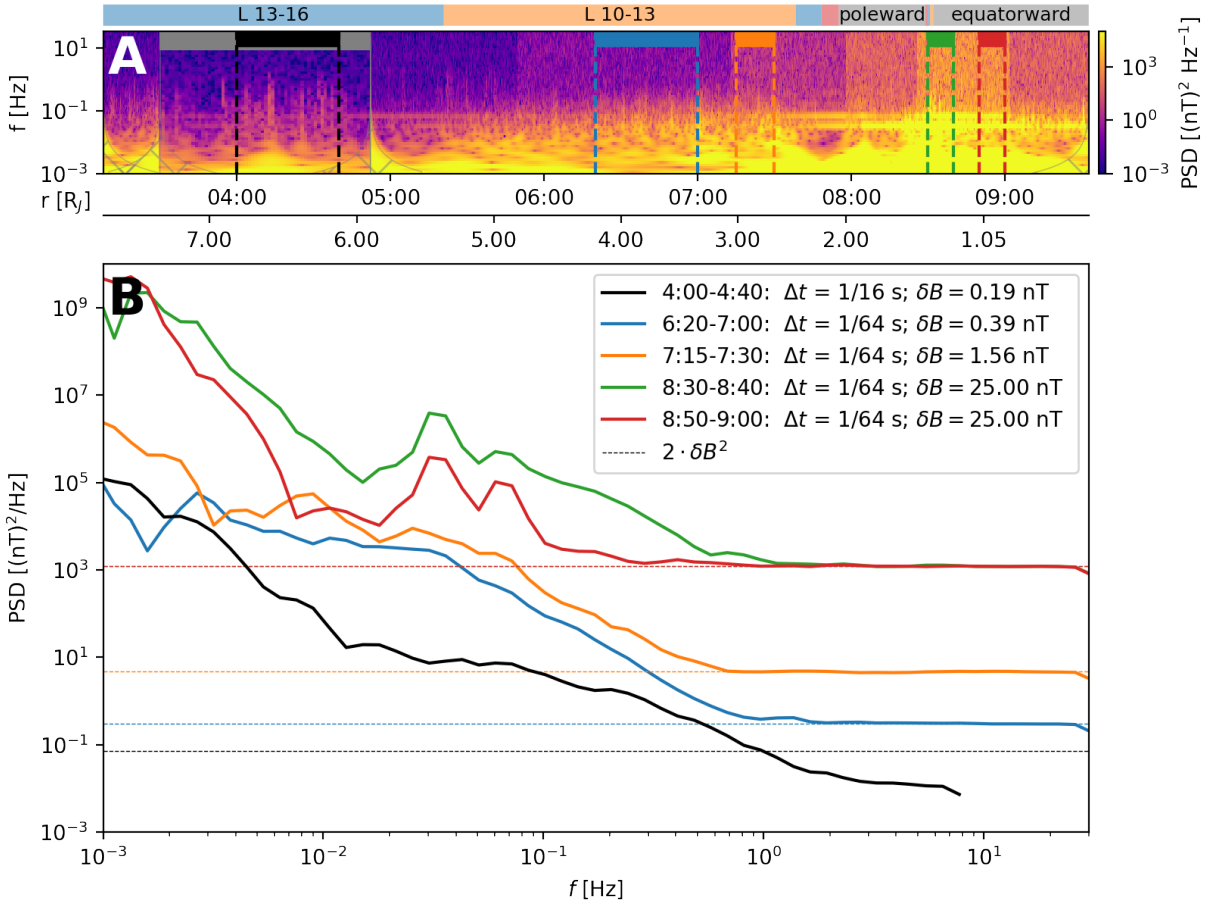

Figure 4.14: The wavelet spectra of the northern flyby of the fifth perijove are displayed over a wide temporal range. All the different digitization levels are visible. The lower part of the graph shows the time-averaged wavelet spectra, with the colored dashed lines indicating the corresponding digitization levels.

not allow observation of magnetic field fluctuations with less than $10\,(\mathrm{nT})^2/\mathrm{Hz}$, mostly corresponding to frequencies greater than 0.8 Hz. However, observations at the lowest digitization level of 0.024 nT provide a resolution that is sufficient to detect fluctuations up to a few Hz. A drawback of observations at higher radial distances is the changing temporal resolution of MAG data, which decreases from 64 Hz to 16 Hz. For example, the wavelet spectrum of the fifth perijove, as seen in Figure 4.14, shows that the Nyquist frequency, the highest resolvable frequency, is 8 Hz between 03:29 and 04:52 UTC.

When looking at the power spectral densities of different digitization levels, it can be seen that they have similar densities at frequencies that are resolved by both levels, as shown in Figure 4.14 by the orange and blue lines. However, the green and red lines in the same figure correspond to the same digitization level but provide a different amount of power in the 0.1 Hz to 0.6 Hz range, as corresponding to other auroral regions. Therefore, the power spectral densities are comparable on the resolved scale at different digitization levels δB for power spectral densities higher than $2 \cdot \delta B^2$.

To detect small-scale fluctuations at frequencies higher than 0.8 Hz, measurements must be taken at the lowest possible digitization level of less than 0.19 nT. This is only

possible at radial distances greater than 5 R_J, which are rarely observed above the main emission zone (see orange zone in Figure 4.9). Six different periods were identified that could provide sufficient location mapping for strong, intense ultraviolet emissions. The power spectra of these times were compared, and each showed small-scale fluctuations up to the highest frequencies (see Figure 4.15).

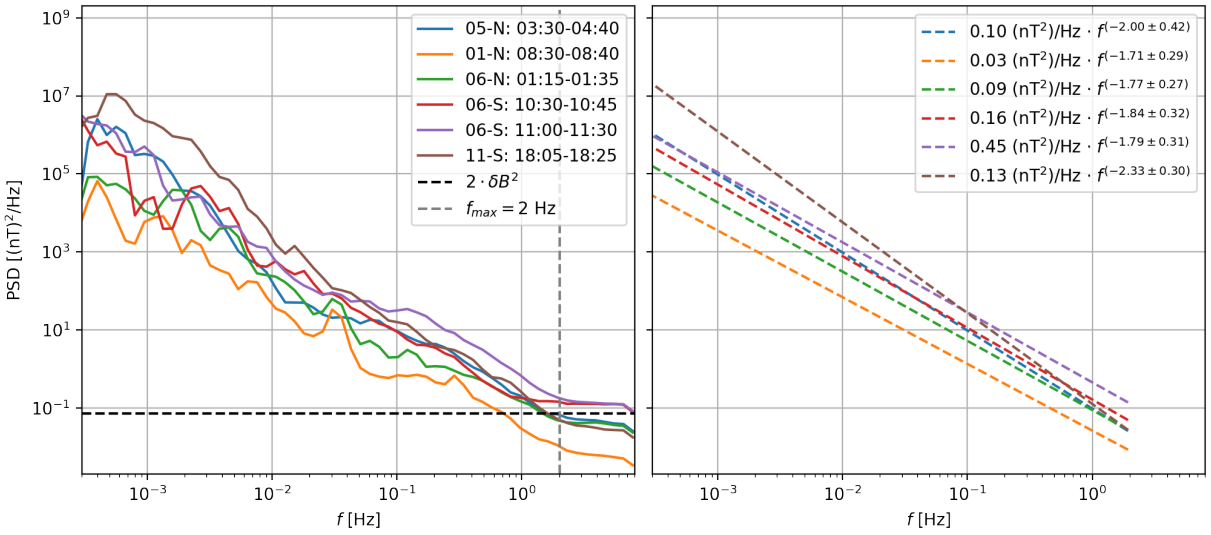

Figure 4.15: Six distinct time spans at high radial distances crossing the main emission zone. The power spectra of these time periods are shown, each providing evidence for small-scale fluctuations up to the highest frequencies. The right-hand side displays the linear regression of the time-averaged spectra on the left. The black and grey dashed line indicate the boundary to unresolved frequencies for the corresponding digitization levels.

The black bars in Figure 4.9 indicate when the spacecraft position is assigned to intense auroral emission. The power spectral densities of these selected times are linear in the log-log space, with a slope of ranging from 1.71 to 2.33 and a Power Spectral Density of 0.03 $(\mathrm{nT})^2/\mathrm{Hz}$ to 0.45 $(\mathrm{nT})^2/\mathrm{Hz}$ at a frequency of 1 Hz. The gray and black dashed lines in Figure 4.15 show the boundary of the resolved frequencies due to the noise level and the corresponding frequency limit. The power is spread over frequencies from 2×10^{-4} Hz to 2 Hz. Some spectra are steeper, providing more power at lower frequencies. The corresponding time intervals show strong magnetic field deviations at smaller frequencies, with amplitudes of up to 50 nT. All of the perijoves have bidirectional electron distributions or isotropic distributions with unresolved loss cones. The energy distribution is broad, and the ultraviolet emission is intense, reaching up to 1000 kR. The energy fluxes are mostly in the range of a few tens of $\mathrm{mW/m^2}$ but can reach a few hundred $\mathrm{mW/m^2}$ when magnetic field amplitudes are greater than 10 nT. All the perijoves where auroral arcs are crossed display small-scale fluctuations at the lowest digitization levels. These times are all at a radial distance between approximately 6 R_J to 7.5 R_J and L-shell between $12.5 - 17$. The flight trajectory only allows for six-time spans above the main emission zone at these high altitudes. As the mission progresses, the northern hemisphere will cover smaller L-shells. In comparison, the southern hemisphere will cover greater L-shells due to the orbit of

Juno being shifted and having a more southward apijove. Consequently, it is unlikely that crossing the main emission zone will occur frequently throughout the following perijoves. Nevertheless, the six time spans demonstrate small-scale fluctuations that could supply thermal energy to the plasma particles transmitted through wave-particle interaction. This implies that stochastic acceleration of these particles is possible, consistent with the wide range of auroral particle observations.

4.3 Discussion

A comprehensive and detailed examination of three of Juno's onboard instruments has revealed a broad overview of the processes that generate auroras. All three observations - magnetic field data, electron distributions, and ultraviolet emissions - were observed during the first 20 flybys of the Juno spacecraft through the polar regions of both hemispheres. The extended statistical analysis of the electron distributions indicated that the primary acceleration acted on a broad energy scale rather than being restricted to one specific energy. The magnetic field data was examined in the same locations where the statistical electron study was conducted to determine whether induced currents caused any sources of acceleration. A better resolution of the magnetic field data was achieved by utilizing additional higher altitude crossings through the main emissions. Ultraviolet emissions, which are associated the precipitated electrons, were used to illustrate the auroral intensities. The observations from all three instruments could be divided into three categories:

- A region of mostly trapped electrons located equatorward of the main emissions, which reached low latitudes affected by the high radiation zone.
- A region, where powerful unidirectional magnetic surges were observed, was linked to unidirectional current.
- A region displayed upward-accelerated electrons, dim and patchy auroras, and no magnetic field variations.

The following sections will provide a detailed analysis of all three types of auroral observations.

The diffuse aurora located mainly at small L-shells at the equatorward edge of the main emission zone, is characterized by high intensities outside the loss cone. This indicates that particles are mainly trapped between the poles, forming a pancake-like pitch angle distribution. As one moves closer to the equator, the pitch angle distributions change to isotropic distributions, indicative of the radiation zone, where particles are randomly deflected in all directions by turbulent magnetic fields. The impact of the radiation zone decreases as the L-shells increase beyond 8. The loss cones are mostly empty when reaching L-shells up to 11, as trapped electrons are not scattered but trapped leaving behind empty loss cones. The statistical study showed that pancake distributions dominate lower magnetic latitudes of less than 76°, corresponding to a L-shell of 16, with a significant contribution of $86.2\% \pm 9.6\%$. The energy flux outside the loss cone is between 10 and 100 $\mathrm{mW/m^2}$ for all radial distances. Verifying these findings, Shen et al. (2022) conducted a comprehensive statistical examination revealing that the pitch angle distributions mainly align with the field at $M > 25$ and become more pancake-shaped at the lower M-shells $M < 15$.

Ocassionally, the downward loss cone is filled with high intensities, where the energy flux rises to a few hundred $100\,\mathrm{mW/m^2}$. This occurs through most (63%) of the pancake-like distribution measurements. These strong intensities in the downward loss cone mostly precipitate into the atmosphere and create light emission, known as diffuse aurora. Therefore, it is not unexpected that ultraviolet emissions display patchy but faint intensities of a few 1000 kR, which is in agreement with the energy fluxes of a few $100\,\mathrm{mW/m^2}$ as suggested by Grodent, Clarke, Kim, et al. (2003), considering H_2 emission. Accordingly, UV emissions are nearly absent, only showing dim and blurred auroras when the downward loss cone is empty. At these times, the azimuthal component of the magnetic field, B_ϕ, is significantly different from the background magnetic field. Its deviation ranges from 50 to 100 nT at radial distances less than $2\,\mathrm{R_J}$ and down to a few nT at distances greater than $2\,\mathrm{R_J}$. The time scales for these deviations vary from 0.5 to 60 seconds. Observations of magnetic field fluctuations of the first perijove showed the presence of Alfvénic turbulence in high-altitude regions mapping to diffuse auroral regions, with broadband distributions and a Poynting flux reaching up to 100 $\mathrm{mW/m^2}$ (Gershman et al., 2019). Sulaiman et al. (2022) proposed that these Alfvénic fluctuations weaken as altitude increases, probably due to dissipation, which provides energy to auroral electrons. There was no correlation between small-scale fluctuations and altitude, as they were observed at all radial distances, but a relation was observed to L-shells smaller than 13. On Earth, the scattering of electrons in the loss cone is caused by whistler mode chorus waves (Ni et al., 2016). The same is likely true in Jupiter's system, with whistler-mode waves generated by anisotropic electron injections (Bhattacharya et al., 2001; Mauk et al., 2002), intensifying the diffuse auroras on Jupiter.

A transition to regions dominated by field-aligned electron beams is seen when the intensities between the loss cones decrease, with intensities outside of the loss cones dropping to around $1 \times 10^4\,1/(\mathrm{cm^2\,s\,sr\,keV})$, leaving the area where the majority of trapped particles are observed.

Strong electron beams are often observed at intermediate latitudes, filling the loss cones in the upward, downward, or both directions. Data collected from these times indicate that broadband distributions are the most common type of electron distribution, making up $93.0\% \pm 3.8$ % of all measurements taken in dipole L-shells between $8 - 50$. Mono-energetic structures, on the other hand, are rarely seen, accounting for only $7.0\% \pm 3.8\%$ of the total. It is possible that some mono-energetic structures were not fully resolved, as they may have been weaker than broadband distributions, making them difficult to distinguish in the presence of a strong background. Mauk et al. (2023) noticed that when strong downward electron broadband acceleration occurs, downward electron electrostatic acceleration disappears, where the cause of broadband preference over coherence is still unknown. However, broadband distributions remain the dominant type of electron distribution in all

regions.

It has been observed that electron beams tend to move in a downward direction at lower magnetic latitudes, whereas, at higher magnetic latitudes, the direction of the beams is upward. A shift between the two regions is observed in the form of bidirectional distributions, which are most prominent between 74° and 79° magnetic latitude. This is in line with the findings of Mauk et al. (2020), who proposed that downward electron acceleration is mainly seen at intermediate latitudes, and upward electron acceleration is more common at higher latitudes, likely due to the presence of upward and downward current regions, respectively. Kotsiaros et al. (2019) also observed that the upward and downward electric currents correspond well to the introduced Zone-I and Zone-II, where Zone-I is connected to the upward magnetic field-aligned currents, leading to downward electron acceleration. The authors also verified that electron distributions can be coherent or broadband in electron spectra, with the latter providing the most intense electron energy flux.

Examination of the magnetic field variations reveals a connection to field-aligned currents. Strong magnetic field increases of up to several hundred nT are observed to be associated with intense field-aligned electron distributions. The directions of the magnetic field change agree with Ampère's law and correspond to the direction of the particles. This means upward electron beams are usually accompanied by downward currents, and downward electron beams are usually associated with upward currents. Positive and negative magnetic field surges are often found close together, showing that downward and upward current regions are often located near each other, particularly when the width of the field-aligned regions is a few thousand kilometers. These findings agree with the theory of electrostatic potentials, which allows for only unidirectional acceleration, thus supporting the theory of stochastic acceleration in both directions along the magnetic field line. However, only a minority of the electron beams show mono-energetic energy distribution but broadband distributions, supporting the theory of stochastic acceleration. Thus, both types of acceleration might occur in a closely related manner. It is possible that mono-energetic distributions could become broadband distributions due to instability, as suggested by Mauk et al. (2018), or that mono-energetic distributions are not adequately resolved, as broadband structures are mostly more intense. Alternatively, powerful stochastic acceleration can occur at higher altitudes, resulting in the detection of strong electron beams only in the downward direction. Here, the unidirectional current would correspond to the charge separation indicated by the downward traveling electron beams rather than as a result of electrostatic potentials. However, the presence of these strong broadband distributions is still puzzling.

The evidence for stochastic acceleration is underlined by the presence of strong bidirectional pitch angle distributions that are associated with magnetic field surges. This is particularly evident when the surges are linked to downward currents. The unidirectional

acceleration would produce only upward electron beams. It is possible that the downward electron beams originate from the other hemisphere, where electrons may have been accelerated in an upward direction, allowing for a unidirectional acceleration resulting in bidirectional electron distributions. The observation of bidirectional electron beams between both upward and downward distributions could be the result of scattering of the upward-accelerated electrons from the other hemisphere, which could be caused by e.g., drift motion, interactions with plasma waves, or collisions with neutral particles as they move along the magnetic field line. This would lead to an overlap between the downward- and upward-accelerated electron regions.

It has been noticed, on certain occasions, that powerful electron beams aligned with the magnetic field have been seen without any alterations to the magnetic field. There are several explanations. The alterations in the magnetic field are too insignificant to be noticed above the background noise level or that both ions and electrons are moving in the same direction, preventing a current due to charge separation. Additionally, some of these structures showed mono-energetic energy distributions, usually seen when a downward electron beam is present and strong magnetic surges are detected. However, no changes in the magnetic field were observed. Thus, an acceleration process due to wave-particle interaction might occur on frequencies smaller than those resolved by the magnetometer. Additionally, lower-altitude observations might not detect direct signs of wave-particle interactions because the waves have dissipated as they contribute to particle acceleration at higher latitudes.

Small-scale fluctuations are intensely present at smaller L-shells that connect to diffuse aurora. However, they are not observable at higher latitudinal regions, yet the cause of decay within a short distance going poleward is uncertain. Sulaiman et al. (2022) found large-scale electron density reductions, known as auroral cavities, in Jupiter's polar regions between the diffuse aurora and Zone I. This could explain why no magnetic field fluctuations were seen in Zone I. As the density decreases, the Alfvén speed increases, and the magnetic field fluctuations decrease, while the Poynting flux remains constant. Furthermore, density depletions are linked to auroral particle acceleration, reducing the number of charge carriers for a strong field-aligned current. Minor magnetic field variations may appear too faint to be detected because of the density depletions.

Further investigations are conducted at greater radial distances to determine whether the magnetic field alterations are too small to be noticed above the noise level. They showed that small-scale fluctuations are not resolved at radial distances $<5\,\mathrm{R_J}$, as the digitization level only provides a resolution of $>1\,\mathrm{nT}$. Minor variations in field-aligned electron beams are observed at higher radial distances, with amplitudes of $2-10$ nT. At all times, when the spacecraft was located above the high-latitude emission zone at radial distances of $>5\,\mathrm{R_J}$, the Power Spectral Density follows a power law across a wide range of frequencies from $1\times10^{-3}\,\mathrm{Hz}$ extending well to 2 Hz. Some perijoves show at the same time

magnetic field surges of up to 50 nT and an electron energy flux of a few hundred mW/m^2, which could generate strong auroral emissions reaching 1000 kR, as suggested by Grodent, Clarke, Kim, et al. (2003). Thus, small-scale fluctuations are observed simultaneously as great magnetic field surges, indicating that wave-particle acceleration might also be related to the great magnetic field surges observed at the lower altitudes. Examining observations from even higher altitudes, Lorch et al. (2022) discovered magnetic field fluctuations indicating Alfvénic activity, characterized by turbulence and energy dissipation at the electron inertial scale. Their calculations indicated that the Poynting flux of these turbulent perturbations is powerful enough to generate auroral emissions. Previous research has also suggested that broadband acceleration of auroral particles can be accomplished through Alfvén waves traveling in the ionospheric Alfvén resonator, which is in agreement with recent Juno observations (Lysak et al., 2021; Damiano et al., 2019).

Appropriately, the electron pitch angle distributions observed are mostly energy-broad and bidirectional or isotropic with unresolved loss cones. Thus, a stochastic acceleration process could be operating in both directions. This implies that bidirectional acceleration at higher altitudes may drive the downward electron beams observed at lower altitudes. As the electrons move along the magnetic field lines to smaller distances, they are observed as upward currents, resulting in a magnetic curl and, thus, magnetic field surges associated with these currents. Particle instruments then detect unidirectional beams in a downward direction. In contrast, the upward-accelerated electrons move away from the planet and toward the other hemisphere, where they could add to the downward electric beams.

Thus, the dominant fraction of broadband energy distributions, the dominant fraction of bidirectional pitch angle distributions, and the observation of small-scale magnetic field variations at higher altitudes favor the importance of a stochastic acceleration process. Nevertheless, electrostatic acceleration is also very likely, as mono-energetic structures are observed with strong electric currents, directly indicating an electron acceleration through a specific potential drop. Electrostatic potentials sometimes cause downward electron acceleration and are near intense ultraviolet emissions. These mono-energetic beams are surrounded by intense broadband distributions, which could result from the instability of the powerful electron beams, broadening the spectra, or from a simultaneously occurring stochastic acceleration process. Bidirectional beams are primarily observed in downward current regions, with enough downward electron intensities to drive the intense auroral emissions. Strong downward currents also provide unidirectional electron acceleration, which might travel to the other hemisphere and contribute as downward electron beams. It is important to note that observations at higher altitudes mostly showed bidirectional electron distributions, indicating that either particles from both hemispheres are observed or that bidirectional acceleration might also occur on higher altitudes of 6 R_J. Therefore, investigating Juno Instrument measurements through radial distance and L-shells might reveal a better insight.

Regions of mostly downward currents are observed when reaching higher latitudes, with a smooth transition. Here, mostly field-aligned electron beams, either bidirectional or upward, and broadband energy distributions are observed. When electron beams are minimal with few mW/m^2 and are directed upwards, the magnetic field variations are insignificant, and UV emissions are faint through higher L-shells. This is particularly noticeable in the Southern Hemisphere as higher latitudes are more likely observed there. Otherwise, intense, patchy, and intermediate blurs are seen with electron beams comparable in intensity to the unidirectional electron beams. But these beams are mostly accelerated upward, sometimes showing bidirectional beams. Negative magnetic field gradients with intense UV emission are only seen when the currents are bidirectional. Additionally, electrons penetrate the detectors with energies as high as 1 MeV, as indicated by the minimum ionizing effect at 150 keV. These distributions are observed along with these strong upward electron beams. The UVS detected high-energy electrons, which revealed a barcode pattern of MeV electron bursts in the MeV range throughout $0.1 - 1$ s, suggesting the presence of whistler waves (Bonfond et al., 2018). According to Clark, Mauk, Haggerty, et al. (2017), JEDI detected protons with energies of around 200 keV that had a conic shape. This suggests that these protons were accelerated away from the planet by energetic electron beams, which generate waves that propelled the protons out of the ionosphere. This coincides with the observations, where intense electron upward beams are predominately observed, likely driving these proton accelerations. Energetic electrons (MeV) have also been observed over the polar cap, with persistent, strongly field-aligned, down-going heavy ions and mostly upward-going energetic electrons, with inverted V and broadband distributions (Ebert et al., 2017; Elliott, Gurnett, Kurth, Clark, et al., 2018; Mauk et al., 2020; Paranicas et al., 2018; Mauk, Haggerty, Paranicas, et al., 2017b). However, these beams did not explain the strong polar x-ray emissions observed (Haggerty et al., 2017). Still, these energetic upgoing electron beams are associated with whistler-mode waves that scatter these upgoing electrons away from the magnetic field line (Tetrick et al., 2017; Elliott, Gurnett, Kurth, Clark, et al., 2018). A strong correlation between probable intense whistler-mode waves and intense downward fluxes of electrons with a broad energy spectrum was deduced by Kurth et al. (2018) and mapped to auroral bright spots by Haewsantati et al. (2023). Thus, no clear physical boundary to the polar cap is found.

CHAPTER 5

SUMMARY

This study has conducted a detailed analysis of Juno's onboard instruments, focusing on magnetic field data, electron distributions, and ultraviolet emissions during 20 flybys through polar regions. The study revealed that the most intense auroral arcs are observed along with broadband electron energy distributions and significant azimuthal magnetic field deviation corresponding to field-aligned currents, favoring the observation of strong electron beams accelerated by a stochastic process, with occasionally electrostatic structures. Magnetic field data examined potential sources of acceleration as a result of induced currents. Higher altitude crossings enhanced magnetic field data resolution. Ultraviolet emissions demonstrated auroral intensities that reflect precipitated electrons. The observations could be divided into three categories:

1. **Diffuse auroral properties located at small L-shells** were observed near the equatorward edge of the main emission zone. In this region, particles are trapped between the poles, forming pancake-like pitch angle distributions at magnetic latitudes below 76° and a significant contribution of $86.2\% \pm 9.6\%$. As one moves closer to the equator, isotropic distributions with high intensities are observed, indicating the radiation zone. Downward electron beams are observed, where trapped particles are randomly scattered due to turbulent magnetic fields with energy flux outside the loss cone ranging from 10 to 100 $\mathrm{mW/m^2}$. These intense electrons precipitate into the atmosphere, creating diffuse auroras and patchy but faint ultraviolet emissions. Magnetic field measurements demonstrate considerable azimuthal field fluctuations, suggesting the presence of Alfvénic turbulence. The turbulence weakens when moving toward the poles while reaching higher altitudes. It fades likely because of auroral cavities reducing charge carriers, as observed by Sulaiman et al. (2022). Whistler-mode waves, generated by anisotropic electron injections, might intensify diffuse auroras (Mauk et al., 2002).

2. **Strong electron beams with unidirectional currents** are observed at intermediate magnetic latitudes above the most intense auroral emissions. A transition from diffuse auroral regions is observed while the intensities between the loss cones decrease to around $1e4$ $1/(\mathrm{cm}^2\,\mathrm{s}\,\mathrm{sr}\,\mathrm{keV})$. Intense electron beams are observed filling downward loss cones at intermediate latitudes and upward at higher latitudes, linked to magnetic field changes corresponding to upward and downward currents, respectively. Broadband distributions are common, comprising 93.0% of measurements, while mono-energetic structures are rare (7.0%). Often, bidirectional distributions are observed through intense electron beams originating from both hemispheres' upward electron acceleration or a stochastic acceleration process. Upward electric currents are frequently observed with bidirectional electron distributions, favoring the assumption that a stochastic acceleration process takes place at higher latitudes. Mono-energetic beams sometimes coexist with broadband distributions, even transitioning from one into the other due to instability or exceeding each other. Further observations at higher altitudes reveal magnetic field variations at high frequencies above 0.5 Hz, supporting the theory of wave-particle acceleration. Stochastic and electrostatic acceleration processes likely operate simultaneously, contributing to the complex electron dynamics in Jupiter's magnetosphere, while stochastic bidirectional acceleration contributes the primary amount in precipitating electron energy flux and intensity.

3. **Mostly upward electron beams with downward currents** at higher latitudes are observed. Frequently, intense bidirectional electron beams are observed with strong magnetic field surges indicating downward currents and intense patch auroral emissions. Upward electron beams are less intense but aligned with high-energy electrons up to 1 MeV. These upward electron beams may also drive proton accelerations away from the planet (Clark, Mauk, Haggerty, et al., 2017), as the energetic electrons in the MeV range are observed over the polar cap, along with intense whistler-mode waves and field-aligned down-going heavy ions (Ebert et al., 2017; Elliott, Gurnett, Kurth, Clark, et al., 2018; Mauk et al., 2020; Paranicas et al., 2018; Mauk, Haggerty, Paranicas, et al., 2017b). Despite these observations, no clear physical boundary to the polar cap is identified.

In summary, Juno's observations comprehensively show the diverse auroral phenomena occurring in Jupiter's polar regions. The interplay of discrete and stochastic acceleration processes contributes to Jupiter's auroras' complex and dynamic nature. The presence of bidirectional pitch angle distributions associated with magnetic field surges indicates either stochastic acceleration processes or scattering of upward-accelerated electrons from the other hemisphere. The transition from unidirectional to bidirectional distributions suggests a complex interplay of acceleration mechanisms operating in Jupiter's magnetosphere.

This work showed that each instrument has limitations within the different magnetospheric regions. Some resolve better at close distances, and some at distances farther away. Thus, the interpretation of the data may always be limited to a selection of observations but still would provide a broad overview of the magnetospheric properties. To understand the origin of bidirectional electron distributions, a better radial resolution that extends beyond $3\,R_J$ could indicate the acceleration region with a transition from bidirectional to only upward electron distributions. Proton observations should be included in the broad stochastical analysis to investigate whether electrostatic currents cause downward electron distributions. With electron and proton observations, one can see if the currents lead to electron and ion acceleration in the opposite direction. Additionally, considering isotropic distributions within the electron particle classification scheme would better distinguish the diffuse region from regions affected by the radiation zone. A broad statistical analysis of the magnetic field variations may also contribute to the understanding of the acceleration mechanism while studying any dependence on magnetospheric location, either L-shell or radius. A broad statistic is strongly limited by the digitization level and Eddy currents, drastically shaping the magnetic field observations at distances of less than $5\,R_J$. Nevertheless, the rms may provide any dependency on magnetospheric location. A line graph of the average ultraviolet emission brightness could enhance the comparability with other parameter and potentially enable higher temporal resolution.

In summary, Juno's observations have impressively illuminated the complex auroral phenomena in Jupiter's polar regions, challenging our existing knowledge of the Jupiter system. Auroral phenomena, in particular, proved to be far more complicated than initially anticipated. Despite the remarkable insights gained into the processes at small radial distances, understanding these highly intricate magnetospheric processes remains challenging because of limited spatial and temporal resolutions. Further research and observations are essential to unravel the complex mechanisms underlying these fascinating auroral lights. It is, therefore, of great interest to gain a more sophisticated statistical overview of the different plasma properties through the magnetic latitudes and, most interestingly, through the radial distances. Therefore, future research efforts should focus on refining data analysis techniques and integrating observations from the various instruments onboard Juno. Collaboration and continuous advancements are essential to uncover the underlying mechanisms driving Jupiter's auroral lights.

References

Allegrini, F., Bagenal, F., Bolton, S., Connerney, J. E. P., Clark, G., Ebert, R. W., ... Zink, J. (2017). Electron beams and loss cones in the auroral regions of jupiter. *Geophysical Research Letters*, *44*. doi: 10.1002/2017GL073180

Bagenal, F. (1994). Empirical model of the io plasma torus: Voyager measurements. *Journal of Geophysical Research: Space Physics*, *99*(A6). doi: 10.1029/93ja02908

Bagenal, F., Adriani, A., Allegrini, F., Bolton, S., Bonfond, B., Bunce, E. J., ... Zarka, P. (2017). Magnetospheric science objectives of the juno mission. *Space Science Reviews*, *213*(1). doi: 10.1007/s11214-014-0036-8

Bagenal, F., & Delamere, P. A. (2011). Flow of mass and energy in the magnetospheres of jupiter and saturn. *Journal of Geophysical Research: Space Physics*, *116*(A5). doi: 10.1029/2010JA016294

Bame, S. J., Barraclough, B. L., Feldman, W. C., Gisler, G. R., Gosling, J. T., McComas, D. J., ... Neugebauer, M. (1992). Jupiter's magnetosphere: Plasma description from the ulysses flyby. *Science*, *257*(5076). doi: 10.1126/science.257.5076.1539

Baron, R. L., Owen, T. C., Connerney, J. E. P., Satoh, T., & Harrington, J. (1996). Solar wind control of jupiter's h+3auroras. *Icarus*, *120*(2). doi: 10.1006/icar.1996.0063

Baumjohann, W., & Treumann, R. A. (1996). *Basic space plasma physics.* Imperial College Press. doi: 10.1142/p015

Bevington, P. R., Robinson, D. K., Blair, J. M., Mallinckrodt, A. J., & McKay, S. (1993). *Data reduction and error analysis for the physical sciences* (Vol. 7). McGraw-Hill Education. doi: 10.1063/1.4823194

Bhattacharya, B., Thorne, R. M., & Williams, D. J. (2001). On the energy source for diffuse jovian auroral emissivity. *Geophysical Research Letters*, *28*(14). doi: 10.1029/2000gl012616

Bieber, J. W., Chen, J., Matthaeus, W. H., Smith, C. W., & Pomerantz, M. A. (1993). Long-term variations of interplanetary magnetic field spectra with implications for cosmic ray modulation. *Journal of Geophysical Research: Space Physics*, *98*(A3). doi: 10.1029/92JA02566

Bigg, E. K. (1964). Influence of the satellite io on jupiter's decametric emission. *Nature*, *203*(4949). doi: 10.1038/2031008a0

Blöcker, A., Kronberg, E. A., Grigorenko, E. E., Clark, G., Kozak, L., Vogt, M. F., & Roussos, E. (2022). Plasmoids in the jovian magnetotail: Statistical survey of ion acceleration using juno observations. *Journal of Geophysical Research: Space Physics*, *127*(8). doi: 10.1029/2022ja030460

Bolton, S., Lunine, J., Stevenson, D., Connerney, J. E. P., Levin, S. M., Owen, T. C., ... Thorpe, R. (2017). The juno mission. *Space Science Reviews*, *213*(1-4). doi: 10.1007/s11214-017-0429-6

Bonfond, B. (2012). When moons create aurora: The satellite footprints on giant planets.

In *Auroral phenomenology and magnetospheric processes: Earth and other planets.* American Geophysical Union (AGU). doi: 10.1029/2011GM001169

Bonfond, B., Gladstone, G. R., Grodent, D., Gérard, J.-C., Greathouse, T. K., Hue, V., ... Connerney, J. E. P. (2018). Bar code events in the juno-uvs data: Signature 10 mev electron microbursts at jupiter. *Geophysical Research Letters*, *45*. doi: 10.1029/2018GL080490

Bonfond, B., Gladstone, G. R., Grodent, D., Greathouse, T. K., Versteeg, M., Hue, V., ... Kurth, W. S. (2017). Morphology of the uv aurorae jupiter during juno's first perijove observations. *Geophysical Research Letters*, *44*(10). doi: 10.1002/2017GL073114

Bonfond, B., Grodent, D., Gérard, J.-C., Radioti, A., Dols, V., Delamere, P. A., & Clarke, J. T. (2009). The io UV footprint: Location, inter-spot distances and tail vertical extent. *Journal of Geophysical Research: Space Physics*, *114*(A7). doi: 10.1029/2009ja014312

Bonfond, B., Grodent, D., Gérard, J.-C., Stallard, T. S., Clarke, J. T., Yoneda, M., ... Gustin, J. (2012). Auroral evidence of io's control over the magnetosphere of jupiter. *Geophysical Research Letters*, *39*(1). doi: 10.1029/2011GL050253

Bonfond, B., Yao, Z., Gladstone, G. R., Grodent, D., Gérard, J.-C., Matar, J., ... Bolton, S. (2021). Are dawn storms jupiter's auroral substorms? *AGU Advances*, *2*(1). doi: 10.1029/2020AV000275

Branduardi-Raymont, G., Bhardwaj, A., Elsner, R. F., Gladstone, G. R., Ramsay, G., Rodriguez, P., ... Cravens, T. E. (2007). Latest results on jovian disk x-rays from XMM-newton. *Planetary and Space Science*, *55*(9). doi: 10.1016/j.pss.2006.11.017

Broadfoot, A. L., Belton, M. J. S., Takacs, P. Z., Sandel, B. R., Shemansky, D. E., Holberg, J. B., ... McElroy, M. B. (1979). Extreme ultraviolet observations from voyager 1 encounter with jupiter. *Science*, *204*(4396). doi: 10.1126/science.204.4396.979

Bunce, E. J., & Cowley, S. W. H. (2001a). Divergence of the equatorial current in the dawn sector of jupiter's magnetosphere: analysis of pioneer and voyager magnetic field data. *Planetary and Space Science*, *49*(10-11). doi: 10.1016/s0032-0633(01)00004-6

Bunce, E. J., & Cowley, S. W. H. (2001b). Local time asymmetry of the equatorial current sheet in jupiter's magnetosphere. *Planetary and Space Science*, *49*(3-4). doi: 10.1016/s0032-0633(00)00147-1

Burke, B. F., & Franklin, K. L. (1955). Observations of a variable radio source associated with the planet jupiter. *Journal of Geophysical Research (1896-1977)*, *60*(2). doi: 10.1029/JZ060i002p00213

Clark, G., Mauk, B. H., Haggerty, D., Paranicas, C. P., Kollmann, P., Rymer, A., ... Valek, P. (2017). Energetic particle signatures of magnetic field-aligned potentials over jupiter's polar regions. *Geophysical Research Letters*, *44*(17). doi: 10.1002/2017GL074366

Clark, G., Mauk, B. H., Paranicas, C. P., Haggerty, D., Kollmann, P., Rymer, A., ... Valek, P. (2017). Observation and interpretation of energetic ion conics in jupiter's polar

magnetosphere. *Geophysical Research Letters*, *44*(10). doi: 10.1002/2016GL072325

Clark, G., Tao, C., Mauk, B. H., Nichols, J. D., Saur, J., Bunce, E. J., ... Valek, P. (2018). Precipitating electron energy flux and characteristic energies in jupiter's main auroral region as measured by juno/jedi. *Journal of Geophysical Research: Space Physics*, *123*(9). doi: 10.1029/2018JA025639

Clarke, J. T., Ajello, J. M., Ballester, G. E., Ben Jaffel, L., Connerney, J. E. P., Gérard, J.-C., ... Waite, J. H. (2002). Ultraviolet emissions from the magnetic footprints of io, ganymede and europa on jupiter. *Nature*, *415*(6875). doi: 10.1038/415997a

Clarke, J. T., Moos, H. W., Atreya, S. K., & Lane, A. L. (1980). Observations from earth orbit and variability of the polar aurora on jupiter. *The Astrophysical Journal*, *241*. doi: 10.1086/183386

Clarke, J. T., Nichols, J. D., Gérard, J.-C., Grodent, D., Hansen, K. C., Kurth, W. S., ... Cecconi, B. (2009). Response of jupiter's and saturn's auroral activity to the solar wind. *Journal of Geophysical Research: Space Physics*, *114*(A5). doi: 10.1029/2008ja013694

Connerney, J. E. P. (1981). The magnetic field of jupiter: A generalized inverse approach. *Journal of Geophysical Research: Space Physics*, *86*(A9). doi: 10.1029/JA086iA09p07679

Connerney, J. E. P., Acuña, M. H., & Ness, N. F. (1981). Modeling the jovian current sheet and inner magnetosphere. *Journal of Geophysical Research*, *86*(A10). doi: 10.1029/ja086ia10p08370

Connerney, J. E. P., Acuña, M. H., Ness, N. F., & Satoh, T. (1998). New models of jupiter's magnetic field constrained by the io flux tube footprint. *Journal of Geophysical Research: Space Physics*, *103*(A6). doi: 10.1029/97JA03726

Connerney, J. E. P., Adriani, A., Allegrini, F., Bagenal, F., Bolton, S., Bonfond, B., ... Waite, J. H. (2017). Jupiter's magnetosphere and aurorae observed by the juno spacecraft during its first polar orbits. *Science*, *356*(6340). doi: 10.1126/science.aam5928

Connerney, J. E. P., Kotsiaros, S., Oliversen, R. J., Espley, J. R., Joergensen, J. L., Joergensen, P. S., ... Levin, S. M. (2018). A new model of jupiter's magnetic field from juno's first nine orbits. *Geophysical Research Letters*, *45*(6). doi: 10.1002/2018GL077312

Connerney, J. E. P., Satoh, T., & Baron, R. L. (1996). Interpretation of auroral "lightcurves" with application to jovian h+3emissions. *Icarus*, *122*(1). doi: 10.1006/icar.1996.0107

Connerney, J. E. P., Timmins, S., Herceg, M., & Joergensen, J. L. (2020). A jovian magnetodisc model for the juno era. *Journal of Geophysical Research: Space Physics*, *125*(10). doi: 10.1029/2020JA028138

Connerney, J. E. P., Timmins, S., Oliversen, R. J., Espley, J. R., Joergensen, J. L., Kotsiaros, S., ... Levin, S. M. (2022). A new model of jupiter's magnetic field at the completion of juno's prime mission. *Journal of Geophysical Research: Planets*,

127(2). doi: 10.1029/2021JE007055

Cowley, S. W. H., Balogh, A., Dougherty, M. K., Dunlop, M. W., Edwards, T. M., Forsyth, R. J., ... Staines, K. (1996). Plasma flow in the jovian magnetosphere and related magnetic effects: Ulysses observations. *Journal of Geophysical Research: Space Physics*, *101*(A7), 15197-15210. doi: https://doi.org/10.1029/96JA00461

Cowley, S. W. H., & Bunce, E. J. (2001). Origin of the main auroral oval in jupiter's coupled magnetosphere–ionosphere system. *Planetary and Space Science*, *49*(10). doi: 10.1016/S0032-0633(00)00167-7

Cowley, S. W. H., & Bunce, E. J. (2003). Modulation of jupiter's main auroral oval emissions by solar wind induced expansions and compressions of the magnetosphere. *Planetary and Space Science*, *51*(1). doi: 10.1016/s0032-0633(02)00118-6

Cowley, S. W. H., Nichols, J. D., & Bunce, E. J. (2002). Distributions of current and auroral precipitation in jupiter's middle magnetosphere computed from steady-state hill–pontius angular velocity profiles: solutions for current sheet and dipole magnetic field models. *Planetary and Space Science*, *50*(7-8). doi: 10.1016/s0032-0633(02)00046-6

Cravens, T. E., & Ozak, N. (2012). Auroral ion precipitation and acceleration at the outer planets. In *Geophysical monograph series.* American Geophysical Union. doi: 10.1029/2011gm001159

Damiano, P. A., Chaston, C. C., Hull, A. J., & Johnson, J. R. (2018). Electron distributions in kinetic scale field line resonances: A comparison of simulations and observations. *Geophysical Research Letters*, *45*(12). doi: 10.1029/2018GL077748

Damiano, P. A., Delamere, P. A., Stauffer, B., Ng, C.-S., & Johnson, J. R. (2019). Kinetic simulations of electron acceleration by dispersive scale alfvén waves in jupiter's magnetosphere. *Geophysical Research Letters*, *46*(6). doi: 10.1029/2018gl081219

Delamere, P. A. (2004). Modeling temporal variability of plasma conditions in the io torus during the cassini era. *Journal of Geophysical Research*, *109*(A10). doi: 10.1029/2003ja010354

Delamere, P. A., & Bagenal, F. (2010). Solar wind interaction with jupiter's magnetosphere. *Journal of Geophysical Research: Space Physics*, *115*(A10). doi: 10.1029/2010ja015347

Dougherty, L. P., Bodisch, K. M., & Bagenal, F. (2017). Survey of voyager plasma science ions at jupiter: 2. heavy ions. *Journal of Geophysical Research: Space Physics*, *122*(8). doi: 10.1002/2017ja024053

Drake, F. D., & Hvatum, S. (1959). Non-thermal microwave radiation from Jupiter. *Astronomical Journal*, *64*. doi: 10.1086/108047

Ebert, R. W., Allegrini, F., Bagenal, F., Bolton, S., Connerney, J. E. P., Clark, G., ... Wilson, R. J. (2017). Spatial distribution and properties of 0.1–100 kev electrons in jupiter's polar auroral region. *Geophysical Research Letters*, *44*(18). doi: 10.1002/2017GL075106

Ebert, R. W., Ebert, R. W., Greathouse, T. K., Clark, G., Allegrini, F., Bagenal, F., ... Wilson, R. J. (2019). Comparing electron energetics and uv brightness in jupiter's northern polar region during juno perijove 5. *Geophysical Research Letters*, *46*. doi: 10.1029/2018GL081129

Ebert, R. W., Greathouse, T. K., Clark, G., Allegrini, F., Bagenal, F., Bolton, S., ... Wilson, R. J. (2021). Simultaneous uv images and high-latitude particle and field measurements during an auroral dawn storm at jupiter. *Journal of Geophysical Research: Space Physics*, *126*. doi: 10.1029/2021JA029679

Elliott, S., Gurnett, D. A., Kurth, W. S., Clark, G., Mauk, B. H., Bolton, S., ... Levin, S. M. (2018). Pitch angle scattering of upgoing electron beams in jupiter's polar regions by whistler mode waves. *Geophysical Research Letters*, *45*(3). doi: 10.1002/2017GL076878

Elliott, S., Gurnett, D. A., Kurth, W. S., Mauk, B. H., Ebert, R. W., Clark, G., ... Bolton, S. (2018). The acceleration of electrons to high energies over the jovian polar cap via whistler mode wave-particle interactions. *Journal of Geophysical Research: Space Physics*, *123*(9). doi: 10.1029/2018JA025797

Elsner, R. F. (2005). Simultaneous chandra x ray, hubble space telescope ultraviolet, and ulysses radio observations of jupiter's aurora. *Journal of Geophysical Research*, *110*(A1). doi: 10.1029/2004ja010717

Elsner, R. F., Ramsey, B. D., Waite, J. H., Rehak, P., Johnson, R. E., Cooper, J. F., & Swartz, D. A. (2005). X-ray probes of magnetospheric interactions with jupiter's auroral zones, the galilean satellites, and the io plasma torus. *Icarus*, *178*(2). doi: 10.1016/j.icarus.2005.06.006

Field, G. B. (1959). The Spin Temperature of Intergalactic Neutral Hydrogen. *Journal of Applied Physics*, *129*. doi: 10.1086/146653

Frank, L. A., & Paterson, W. R. (2002). Galileo observations of electron beams and thermal ions in jupiter's magnetosphere and their relationship to the auroras. *Journal of Geophysical Research: Space Physics*, *107*(A12). doi: 10.1029/2001ja009150

Geiss, J., Gloeckler, G., Balsiger, H., Fisk, L. A., Galvin, A. B., Gliem, F., ... Wilken, B. (1992). Plasma composition in jupiter's magnetosphere: Initial results from the solar wind ion composition spectrometer. *Science*, *257*(5076). doi: 10.1126/science.257.5076.1535

Gérard, J.-C., Bonfond, B., Grodent, D., Radioti, A., Clarke, J. T., Gladstone, G. R., ... Shematovich, V. I. (2014). Mapping the electron energy in jupiter's aurora: Hubble spectral observations. *Journal of Geophysical Research: Space Physics*, *119*(11). doi: 10.1002/2014ja020514

Gérard, J.-C., Bonfond, B., Mauk, B. H., Gladstone, G. R., Yao, Z., Greathouse, T. K., ... Levin, S. M. (2019). Contemporaneous observations of jovian energetic auroral electrons and ultraviolet emissions by the juno spacecraft. *Journal of Geophysical Research: Space Physics*, *124*(11). doi: 10.1029/2019JA026862

Gérard, J.-C., Dols, V., Prangé, R., & Paresce, F. (1994a). The morphology of the north jovian ultraviolet aurora observed with the hubble space telescope. *Planetary and Space Science*, *42*(11). doi: 10.1016/0032-0633(94)90051-5

Gershman, D., Connerney, J. E. P., Kotsiaros, S., DiBraccio, G. A., Martos, Y. M., Viñas, A. F., ... Bolton, S. (2019). Alfvénic fluctuations associated with jupiter's auroral emissions. *Geophysical Research Letters*, *46*(13). doi: 10.1029/2019GL082951

Gladstone, G. R., Versteeg, M., Greathouse, T. K., Hue, V., Davis, M. W., Gérard, J.-C., ... Bagenal, F. (2017). Juno-UVS approach observations of jupiter's auroras. *Geophysical Research Letters*, *44*(15). doi: 10.1002/2017gl073377

Greathouse, T. K., Gladstone, G. R., Versteeg, M., Hue, V., Kammer, J. A., Giles, R. S., ... Vogt, M. F. (2021). Local time dependence of jupiter's polar auroral emissions observed by juno UVS. *Journal of Geophysical Research: Planets*, *126*(12). doi: 10.1029/2021je006954

Grodent, D., Bonfond, B., Yao, Z., Gérard, J.-C., Radioti, A., Dumont, M., ... Valek, P. (2018). Jupiter's aurora observed with hst during juno orbits 3 to 7. *Journal of Geophysical Research: Space Physics*, *123*(5). doi: 10.1002/2017JA025046

Grodent, D., Clarke, J. T., Kim, J., Waite Jr., J. H., & Cowley, S. W. H. (2003). Jupiter's main auroral oval observed with hst-stis. *Journal of Geophysical Research: Space Physics*, *108*(A11). doi: 10.1029/2003JA009921

Grodent, D., Clarke, J. T., Waite, J. H., Cowley, S. W. H., Gérard, J.-C., & Kim, J. (2003). Jupiter's polar auroral emissions. *Journal of Geophysical Research*.

Haewsantati, K., Bonfond, B., Wannawichian, S., Gladstone, G. R., Hue, V., Greathouse, T. K., ... G´erard, J.-C. M. C. (2023). Juno's multi-instruments observations during the flybys of auroral bright spots in jupiter's polar aurorae. *Journal of Geophysical Research: Space Physics*, *128*. doi: 10.1029/2023JA031396

Haggerty, D., Mauk, B. H., Paranicas, C. P., Clark, G., Kollmann, P., Rymer, A., ... Levin, S. M. (2017). Juno/jedi observations of 0.01 to >10 mev energetic ions in the jovian auroral regions: Anticipating a source for polar x-ray emission. *Geophysical Research Letters*, *44*(13). doi: 10.1002/2017GL072866

Hess, S., Mottez, F., Zarka, P., & Chust, T. (2008). Generation of the jovian radio decametric arcs from the io flux tube. *Journal of Geophysical Research: Space Physics*, *113*(A3). doi: 10.1029/2007ja012745

Hill, T. W. (1979). Inertial limit on corotation. *Journal of Geophysical Research: Space Physics*, *84*(A11). doi: 10.1029/JA084iA11p06554

Hill, T. W. (2001). The jovian auroral oval. *Journal of Geophysical Research: Space Physics*, *106*(A5). doi: 10.1029/2000JA000302

Hill, T. W., Dessler, A. J., & Goertz, C. K. (1983). Magnetospheric models. In (chap. Magnetospheric models). Cambridge Univ. Press.

Hue, V., Greathouse, T. K., Gladstone, G. R., Bonfond, B., Gérard, J.-C., Vogt, M. F., ... Connerney, J. E. P. (2021). Detection and characterization of circular expanding

UV-emissions observed in jupiter's polar auroral regions. *Journal of Geophysical Research: Space Physics*, *126*(3). doi: 10.1029/2020ja028971

Hui, Y., Schultz, D. R., Kharchenko, V. A., Bhardwaj, A., Branduardi-Raymont, G., Stancil, P. C., ... Dalgarno, A. (2010). Comparative analysis and variability of the jovian x-ray spectra detected by the chandra and XMM-newton observatories. *Journal of Geophysical Research: Space Physics*, *115*(A7). doi: 10.1029/2009ja014854

Janser, S., Saur, J., Clark, G., Sulaiman, A. H., & Szalay, J. R. (2022). Properties of turbulent alfvénic fluctuations and wave-particle interaction associated with io's footprint tail. *Journal of Geophysical Research: Space Physics*, *127*. doi: 10.1029/2022JA030675

Joy, S. P. (2002). Probabilistic models of the jovian magnetopause and bow shock locations. *Journal of Geophysical Research*, *107*(A10). doi: 10.1029/2001ja009146

Khurana, K. K. (2001). Influence of solar wind on jupiter's magnetosphere deduced from currents in the equatorial plane. *Journal of Geophysical Research: Space Physics*, *106*(A11). doi: 10.1029/2000JA000352

Khurana, K. K., Kivelson, M. G., Vasyliunas, V. M., Krupp, N., Woch, J., Lagg, A., ... Kurth, W. S. (2004). The configuration of jupiters magnetosphere. In *Jupiter : The planet, satellites and magnetosphere* (chap. 24). Cambridge University Press.

Kimura, T., Badman, S. V., Tao, C., Yoshioka, K., Murakami, G., Yamazaki, A., ... Clarke, J. T. (2015). Transient internally driven aurora at jupiter discovered by hisaki and the hubble space telescope. *Geophysical Research Letters*, *42*(6). doi: 10.1002/2015gl063272

Kivelson, M. G. (2005). The current systems of the jovian magnetosphere and ionosphere and predictions for saturn. *Space Science Reviews*, *116*(1). doi: 10.1007/s11214-005-1959-x

Kivelson, M. G., Bagenal, F., Kurth, W. S., Neubauer, F. M., Paranicas, C. P., & Saur, J. (2004). Magnetospheric interactions with satellites. *Jupiter: The planet, satellites and magnetosphere*, *1*.

Kivelson, M. G., Khurana, K. K., Russell, C. T., Joy, S. P., Volwerk, M., Walker, R. J., ... Linker, J. A. (2001). Magnetized or unmagnetized: Ambiguity persists following galileo's encounters with io in 1999 and 2000. *Journal of Geophysical Research: Space Physics*, *106*(A11). doi: 10.1029/2000ja002510

Kliore, A., Cain, D. L., Fjeldbo, G., Seidel, B. L., & Rasool, S. I. (1974). Preliminary results on the atmospheres of io and jupiter from the pioneer 10 s-band occultation experiment. *Science*, *183*(4122). doi: 10.1126/science.183.4122.323

Knight, S. (1973). Parallel electric fields. *Planetary and Space Science*, *21*(5). doi: 10.1016/0032-0633(73)90093-7

Kotsiaros, S., Connerney, J. E. P., Clark, G., Allegrini, F., Gladstone, G. R., Kurth, W. S., ... Levin, S. M. (2019). Birkeland currents in jupiter's magnetosphere observed by the polar-orbiting juno spacecraft. *Nature Astronomy*, *3*. doi: 10.1038/

s41550-019-0819-7

Kotsiaros, S., Connerney, J. E. P., & Martos, Y. M. (2020). Analysis of eddy current generation on the juno spacecraft in jupiter's magnetosphere. *Earth and Space Science*, *7*(7). doi: 10.1029/2019EA001061

Kronberg, E. A., Woch, J., Krupp, N., Lagg, A., Daly, P. W., & Korth, A. (2008). Comparison of periodic substorms at jupiter and earth. *Journal of Geophysical Research: Space Physics*, *113*(A4). doi: 10.1029/2007ja012880

Krupp, N., Keppler, E., Seidel, R., Woch, J., Korth, A., Cheng, A. F., ... Dougherty, M. K. (1997). Field-aligned particle streaming in the duskside high latitude jovian magnetosphere. *Advances in Space Research*, *20*(2). doi: 10.1016/s0273-1177(97)00538-3

Kurth, W. S., Mauk, B. H., Elliott, S., Gurnett, D. A., Hospodarsky, G. B., Santolík, O., ... Levin, S. M. (2018). Whistler mode waves associated with broadband auroral electron precipitation at jupiter. *Geophysical Research Letters*, *45*. doi: 10.1029/2018GL078566

Lanzerotti, L. J., Armstrong, T. P., Maclennan, C. G., Simnett, G. M., Cheng, A. F., Gold, R. E., ... Tappin, S. J. (1993). Measurements of hot plasmas in the magnetosphere of jupiter. *Planetary and Space Science*, *41*(11). doi: 10.1016/0032-0633(93)90096-K

Li, W., Ma, Q., Shen, X., Zhang, X., Mauk, B. H., Clark, G., ... Bolton, S. (2021). Quantification of diffuse auroral electron precipitation driven by whistler mode waves at jupiter. *Geophysical Research Letters*, *48*. doi: 10.1029/2021GL095457

Li, W., Thorne, R. M., Ma, Q., Zhang, X., Gladstone, G. R., Hue, V., ... Bolton, S. (2017). Understanding the origin of jupiter's diffuse aurora using juno's first perijove observations. *Geophysical Research Letters*, *44*. doi: 10.1002/2017GL075545

Livengood, T. A., & Moos, H. W. (1990). Jupiter's north and south polar aurorae with IUE data. *Geophysical Research Letters*, *17*(12). doi: 10.1029/gl017i012p02265

Livengood, T. A., Moos, H. W., Ballester, G. E., & Prangé, R. M. (1992). Jovian ultraviolet auroral activity, 1981–1991. *Icarus*, *97*(1). doi: 10.1016/0019-1035(92)90055-C

Lorch, C. T. S., Ray, L. C., Wilson, R. J., Bagenal, F., Crary, F., Delamere, P. A., ... Allegrini, F. (2022). Evidence of alfvénic activity in jupiter's mid-to-high latitude magnetosphere. *Journal of Geophysical Research: Space Physics*, *127*(6). doi: 10.1029/2021JA029853

Luhr, H., Warnecke, J. F., & Rother, M. K. A. (1996). An algorithm for estimating field-aligned currents from single spacecraft magnetic field measurements: a diagnostic tool applied to freja satellite data. *IEEE Transactions on Geoscience and Remote Sensing*, *34*(6). doi: 10.1109/36.544560

Lysak, R. L., Song, Y., Elliott, S., Kurth, W. S., Sulaiman, A. H., & Gershman, D. (2021). The jovian ionospheric alfvén resonator and auroral particle acceleration. *Journal of Geophysical Research: Space Physics*. doi: 10.1029/2021JA029886

Masters, A. (2017). Model-based assessments of magnetic reconnection and kelvin-

helmholtz instability at jupiter's magnetopause. *Journal of Geophysical Research: Space Physics*, *122*(11). doi: 10.1002/2017ja024736

Masters, A. (2018). A more viscous-like solar wind interaction with all the giant planets. *Geophysical Research Letters*, *45*(15). doi: 10.1029/2018gl078416

Masters, A., Dunn, W. R., Stallard, T. S., Manners, H., & Stawarz, J. (2021). Magnetic reconnection near the planet as a possible driver of jupiter's mysterious polar auroras. *Journal of Geophysical Research: Space Physics*, *126*(8). doi: 10.1029/2021ja029544

Mauk, B. H. (2004). Energetic ion characteristics and neutral gas interactions in jupiter's magnetosphere. *Journal of Geophysical Research*, *109*(A9). doi: 10.1029/2003ja010270

Mauk, B. H. (2013). Analysis of EMIC-wave-moderated flux limitation of measured energetic ion spectra in multispecies magnetospheric plasmas. *Geophysical Research Letters*, *40*(15). doi: 10.1002/grl.50789

Mauk, B. H., Allegrini, F., Bagenal, F., Bolton, S., Clark, G., Connerney, J. E. P., ... Sulaiman, A. H. (2022). Loss of energetic ions comprising the ring current populations of jupiter's middle and inner magnetosphere. *Journal of Geophysical Research: Space Physics*, *127*. doi: 10.1029/2022JA030293

Mauk, B. H., & Bagenal, F. (2012). Comparative auroral physics: Earth and other planets. In *Auroral phenomenology and magnetospheric processes: Earth and other planets.* American Geophysical Union (AGU). doi: 10.1029/2011GM001192

Mauk, B. H., Clark, G., Gladstone, G. R., Kotsiaros, S., Adriani, A., Allegrini, F., ... Rymer, A. (2020). Energetic particles and acceleration regions over jupiter's polar cap and main aurora: A broad overview. *Journal of Geophysical Research: Space Physics*, *125*(3). doi: 10.1029/2019JA027699

Mauk, B. H., Clarke, J. T., Grodent, D., Waite, J. H., Paranicas, C. P., & Williams, D. J. (2002). Transient aurora on jupiter from injections of magnetospheric electrons. *Nature*, *415*(6875). doi: 10.1038/4151003a

Mauk, B. H., Haggerty, D., Jaskulek, S., Schlemm, C., Brown, L., Cooper, S., ... Stokes, M. (2017). The jupiter energetic particle detector instrument (jedi) investigation for the juno mission. *Space Science Reviews*, *213*(1). doi: 10.1007/S11214-013-0025-3

Mauk, B. H., Haggerty, D., Paranicas, C. P., Clark, G., Kollmann, P., Rymer, A., ... Valek, P. (2017a). Discrete and broadband electron acceleration in jupiter's powerful aurora. *Nature*, *549*(7670). doi: 10.1038/nature23648

Mauk, B. H., Haggerty, D., Paranicas, C. P., Clark, G., Kollmann, P., Rymer, A., ... Valek, P. (2017b). Juno observations of energetic charged particles over jupiter's polar regions: Analysis of monodirectional and bidirectional electron beams. *Geophysical Research Letters*, *44*(10). doi: 10.1002/2016GL072286

Mauk, B. H., Haggerty, D., Paranicas, C. P., Clark, G., Kollmann, P., Rymer, A., ... Valek, P. (2018). Diverse electron and ion acceleration characteristics observed over jupiter's main aurora. *Geophysical Research Letters*, *45*. doi: 10.1002/2017GL076901

Mauk, B. H., & Saur, J. (2007). Equatorial electron beams and auroral structuring at jupiter. *Journal of Geophysical Research: Space Physics*, *112*(A10). doi: 10.1029/2007JA012370

Mauk, B. H., Szalay, J. R., Allegrini, F., Bagenal, F., Bolton, S., Clark, G., ... Sulaiman, A. H. (2023). How bi-modal are jupiter's main aurora zones? *Journal of Geophysical Research: Space Physics*, *128*. doi: 10.1029/2022JA031237

McComas, D. J., Alexander, N., Allegrini, F., Allegrini, F., Bagenal, F., Beebe, C., ... White, D. (2017). The jovian auroral distributions experiment (jade) on the juno mission to jupiter. *Space Science Reviews*, *213*(1). doi: 10.1007/S11214-013-9990-9

McComas, D. J., & Cowley, S. W. H. (2007). Jupiter: A fundamentally different magnetospheric interaction with the solar wind. *Geophysical Research Letters*, *34*(20). doi: 10.1029/2007gl031078

McNutt, R. L., Belcher, J. W., Sullivan, J. D., Bagenal, F., & Bridge, H. S. (1979). Departure from rigid co-rotation of plasma in jupiter's dayside magnetosphere. *Nature*, *280*(5725). doi: 10.1038/280803a0

NASA Planetary Data System. (2022). *Juno magnetometer jupiter archive.* doi: 10.17189/1519711

NASA Planetary Data System. (2023). *Juno jedi jupiter standard calibrated products (jno j jed 3 cdr v1.0).* doi: 10.17189/1519713

Newell, P. T., Sotirelis, T., & Wing, S. (2009). Diffuse, monoenergetic, and broadband aurora: The global precipitation budget. *Journal of Geophysical Research: Space Physics*, *114*(A9). doi: 10.1029/2009JA014326

Ni, B., Thorne, R. M., Zhang, X., Bortnik, J., Pu, Z., Xie, L., ... Gu, X. (2016). Origins of the earth's diffuse auroral precipitation. *Space Science Reviews*, *200*(1). doi: 10.1007/s11214-016-0234-7

Nichols, J. D., Badman, S. V., Bagenal, F., Bolton, S., Bonfond, B., Bunce, E. J., ... Yoshikawa, I. (2017). Response of jupiter's auroras to conditions in the interplanetary medium as measured by the hubble space telescope and juno. *Geophysical Research Letters*, *44*(15). doi: 10.1002/2017gl073029

Nichols, J. D., Clarke, J. T., Gérard, J.-C., & Grodent, D. (2009). Observations of jovian polar auroral filaments. *Geophysical Research Letters*, *36*(8). doi: 10.1029/2009gl037578

Nichols, J. D., & Cowley, S. W. H. (2004). Magnetosphere-ionosphere coupling currents in jupiter's middle magnetosphere: effect of precipitation-induced enhancement of the ionospheric pedersen conductivity. *Annales Geophysicae*, *22*(5). doi: 10.5194/angeo-22-1799-2004

Pallier, L., & Prangé, R. (2001). More about the structure of the high latitude jovian aurorae. *Planetary and Space Science*, *49*(10-11). doi: 10.1016/s0032-0633(01)00023-x

Paranicas, C. P., Mauk, B. H., Haggerty, D., Clark, G., Kollmann, P., Rymer, A., ...

Bolton, S. (2018). Intervals of intense energetic electron beams over jupiter's poles. *Journal of Geophysical Research: Space Physics*, *123*. doi: 10.1002/2017JA025106

Paschmann, G., & Daly, P. W. (1998). Analysis Methods for Multi-Spacecraft Data. ISSI Scientific Reports Series SR-001, ESA/ISSI, Vol. 1. ISBN 1608-280X, 1998. *ISSI Scientific Reports Series*, *1*.

Phipps, P. H., Withers, P., Buccino, D. R., & Yang, Y.-M. (2018). Distribution of plasma in the io plasma torus as seen by radio occultation during juno perijove 1. *Journal of Geophysical Research: Space Physics*, *123*(8). doi: 10.1029/2017ja025113

Pryor, W. R., Stewart, A. I. F., Esposito, L. W., McClintock, W. E., Colwell, J. E., Jouchoux, A. J., ... Dougherty, M. K. (2005). Cassini UVIS observations of jupiter's auroral variability. *Icarus*, *178*(2). doi: 10.1016/j.icarus.2005.05.021

Rabia, J., Hue, V., Szalay, J. R., André, N., Nénon, Q., Blanc, M., ... Sulaiman, A. H. (2023). Evidence for non-monotonic and broadband electron distributions in the europa footprint tail revealed by juno in situ measurements. *Geophysical Research Letters*, *50*. doi: 10.1029/2023GL103131

Radioti, A., Tomás, A. T., Grodent, D., Gérard, J.-C., Gustin, J., Bonfond, B., ... Menietti, J. D. (2009). Equatorward diffuse auroral emissions at jupiter: Simultaneous HST and galileo observations. *Geophysical Research Letters*, *36*(7). doi: 10.1029/2009gl037857

Ray, L. C., Ergun, R. E., Delamere, P. A., & Bagenal, F. (2010). Magnetosphere-ionosphere coupling at jupiter: Effect of field-aligned potentials on angular momentum transport. *Journal of Geophysical Research: Space Physics*, *115*(A9). doi: 10.1029/2010JA015423

Salveter, A., Saur, J., Clark, G., & Mauk, B. H. (2022). Jovian auroral electron precipitation budget—a statistical analysis of diffuse, mono-energetic, and broadband auroral electron distributions. *Journal of Geophysical Research: Space Physics*, *127*(8). doi: 10.1029/2021JA030224

Sarkango, Y., Szalay, J. R., Poppe, A. R., Nénon, Q., Kollmann, P., Clark, G., & McComas, D. J. (2023). Proton equatorial pitch angle distributions in jupiter's inner magnetosphere. *Geophysical Research Letters*, *50*(11). doi: 10.1029/2023gl104374

Saur, J. (2004). Turbulent heating of jupiter's middle magnetosphere. *The Astrophysical Journal*, *602*(2). doi: 10.1086/382588

Saur, J., Janser, S., Schreiner, A., Clark, G., Mauk, B. H., Kollmann, P., ... Kotsiaros, S. (2018). Wave-particle interaction of alfvén waves in jupiter's magnetosphere: Auroral and magnetospheric particle acceleration. *Journal of Geophysical Research: Space Physics*, *123*. doi: 10.1029/2018JA025948

Saur, J., Mauk, B. H., Mitchell, D. G., Krupp, N., Khurana, K. K., Livi, S., ... Dougherty, M. K. (2006). Anti-planetward auroral electron beams at saturn. *Nature*, *439*(7077). doi: 10.1038/nature04401

Saur, J., Politano, H., Pouquet, A., & Matthaeus, W. H. (2002). Evidence for weak mhd turbulence in the middle magnetosphere of jupiter. *A&A*, *386*(2). doi: 10.1051/

0004-6361:20020305

Saur, J., Pouquet, A., & Matthaeus, W. H. (2003). An acceleration mechanism for the generation of the main auroral oval on jupiter. *Geophysical Research Letters*, *30*(5). doi: 10.1029/2002GL015761

Seidel, R., Keppler, E., Krupp, N., Woch, J., Hawkins, S. E., Lanzerotti, L. J., & Dougherty, M. K. (1997). Energetic electron beams in the duskside jovian magnetosphere: Ulysses epac and hi-scale measurements. *Planetary and Space Science*, *45*(11). doi: 10.1016/S0032-0633(97)00148-7

Seiff, A., Kirk, D. B., Knight, T. C. D., Young, R. E., Mihalov, J. D., Young, L. A., ... Atkinson, D. (1998). Thermal structure of jupiter's atmosphere near the edge of a 5-μm hot spot in the north equatorial belt. *Journal of Geophysical Research: Planets*, *103*(E10). doi: 10.1029/98JE01766

Shen, X., Li, W., Ma, Q., Nishimura, Y., Daly, A., Kollmann, P., ... Bolton, S. (2022). Energetic proton distributions in the inner and middle magnetosphere of jupiter using juno observations. *Geophysical Research Letters*, *49*. doi: 10.1029/2022GL099832

Sinclair, J. A., Orton, G. S., Fernandes, J., Kasaba, Y., Sato, T. M., Fujiyoshi, T., ... Irwin, P. G. J. (2019). A brightening of jupiter's auroral 7.8-nanometer CH4 emission during a solar-wind compression. *Nature Astronomy*, *3*(7). doi: 10.1038/s41550-019-0743-x

Smith, E. J., Davis, L., Jones, D. E., Coleman, P. J., Colburn, D. S., Dyal, P., & Sonett, C. P. (1975). Jupiter's magnetic field. magnetosphere, and interaction with the solar wind: Pioneer 11. *Science*, *188*(4187). doi: 10.1126/science.188.4187.451

Smith, E. J., Davis Jr., L., Jones, D. E., Coleman Jr., P. J., Colburn, D. S., Dyal, P., ... Frandsen, A. M. A. (1974). The planetary magnetic field and magnetosphere of jupiter: Pioneer 10. *Journal of Geophysical Research (1896-1977)*, *79*(25). doi: 10.1029/JA079i025p03501

Sulaiman, A. H., Allegrini, F., Clark, G., Gladstone, G. R., Kotsiaros, S., Kurth, W. S., ... Bolton, S. (2022). Jupiter's low-altitude auroral zones: Fields, particles, plasma waves, and density depletions. *Journal of Geophysical Research. Space Physics*, *127*. doi: 10.1029/2022JA030334

Szalay, J. R., Allegrini, F., Bagenal, F., Bolton, S., Clark, G., Connerney, J. E. P., ... Wilson, R. J. (2017). Plasma measurements in the jovian polar region with juno/jade. *Geophysical Research Letters*, *44*(14). doi: 10.1002/2017GL072837

Szalay, J. R., Allegrini, F., Bagenal, F., Bolton, S., Clark, G., Connerney, J. E. P., ... Wilson, R. J. (2021). Proton outflow associated with jupiter's auroral processes. *Geophysical Research Letters*, *48*(1). doi: 10.1029/2020GL091627

Szalay, J. R., Bonfond, B., Allegrini, F., Bagenal, F., Bolton, S., Clark, G., ... Wilson, R. J. (2018). In situ observations connected to the io footprint tail aurora. *Journal of Geophysical Research: Planets*, *123*. doi: 10.1029/2018JE005752

Tao, C., Kimura, T., Badman, S. V., André, N., Tsuchiya, F., Murakami, G., ... Fujimoto, M. (2015). Variation of jupiter's aurora observed by hisaki/exceed: 2. estimations of

auroral parameters and magnetospheric dynamics. *Journal of Geophysical Research: Space Physics*, *121*(5). doi: 10.1002/2015JA021272

Tao, X., Thorne, R. M., Horne, R. B., Ni, B., Menietti, J. D., Shprits, Y. Y., & Gurnett, D. A. (2011). Importance of plasma injection events for energization of relativistic electrons in the jovian magnetosphere. *Journal of Geophysical Research: Space Physics*, *116*(A1). doi: 10.1029/2010ja016108

Tetrick, S., Gurnett, D. A., Kurth, W. S., Imai, M., Hospodarsky, G. B., Bolton, S., ... Mauk, B. H. (2017). Plasma waves in jupiter's high-latitude regions: Observations from the juno spacecraft. *Geophysical Research Letters*, *44*(10). doi: 10.1002/2017GL073073

Thomas, N., Bagenal, F., Hill, T. W., & Wilson, J. K. (2004). The io neutral clouds and plasma torus. *Jupiter. The Planet, Satellites and Magnetosphere*, *-1*.

Torrence, C., & Compo, G. P. (1998). A practical guide to wavelet analysis. *Bulletin of the American Meteorological Society*, *79*(1). doi: 10.1175/1520-0477(1998)079<0061:APGTWA>2.0.CO;2

Vogt, M. F., Jackman, C. M., Slavin, J. A., Bunce, E. J., Cowley, S. W. H., Kivelson, M. G., & Khurana, K. K. (2014). Structure and statistical properties of plasmoids in jupiter's magnetotail. *Journal of Geophysical Research: Space Physics*, *119*(2). doi: 10.1002/2013ja019393

Waite Jr., J. H., Cravens, T. E., Kozyra, J., Nagy, A. F., Atreya, S. K., & Chen, R. H. (1983). Electron precipitation and related aeronomy of the jovian thermosphere and ionosphere. *Journal of Geophysical Research: Space Physics*, *88*(A8). doi: 10.1029/JA088iA08p06143

Wang, Y., Blanc, M., Louis, C., Wang, C., André, N., Adriani, A., ... Tao, C. (2021). A preliminary study of magnetosphere-ionosphere-thermosphere coupling at jupiter: Juno multi-instrument measurements and modeling tools. *Journal of Geophysical Research: Space Physics*, *126*(9). doi: 10.1029/2021JA029469

Williams, D. J., & Mauk, B. H. (1997). Pitch angle diffusion at jupiter's moon ganymede. *Journal of Geophysical Research: Space Physics*, *102*(A11). doi: 10.1029/97JA02260

Wilson, R. J., Vogt, M. F., Provan, G., Kamran, A., James, M. K., Brennan, M., & Cowley, S. W. H. (2023). Internal and external jovian magnetic fields: Community code to serve the magnetospheres of the outer planets community. *Space Science Reviews*, *219*(1). doi: 10.1007/s11214-023-00961-3

Yao, Z., Bonfond, B., Grodent, D., Chané, E., Dunn, W. R., Kurth, W. S., ... Bolton, S. (2022). On the relation between auroral morphologies and compression conditions of jupiter's magnetopause: Observations from juno and the hubble space telescope. *Journal of Geophysical Research: Space Physics*, *127*(10). doi: 10.1029/2021ja029894

Yao, Z., Dunn, W. R., Woodfield, E. E., Clark, G., Mauk, B. H., Ebert, R. W., ... Bolton, S. (2021). Revealing the source of jupiter's x-ray auroral flares. *Science Advances*, *7*(28). doi: 10.1126/sciadv.abf0851

Yao, Z., Grodent, D., Kurth, W. S., Clark, G., Mauk, B. H., Kimura, T., ... Levin, S. M. (2019). On the relation between jovian aurorae and the loading/unloading of the magnetic flux: Simultaneous measurements from juno, hubble space telescope, and hisaki. *Geophysical Research Letters*, *46*(21). doi: 10.1029/2019gl084201

Zhang, B., Delamere, P. A., Yao, Z., Bonfond, B., Lin, D., Sorathia, K. A., ... Lyon, J. G. (2021). How jupiter's unusual magnetospheric topology structures its aurora. *Science Advances*, *7*(15). doi: 10.1126/sciadv.abd1204

APPENDIX

A.1 Auroral Properties of the Main Emission Crossings

In this section, the observations from the three instruments, FGM, JEDI, and UVS, are used to parametrize each main emission crossing. Table A.1 lists the auroral properties of the main emission crossings, which are dominated by the spacecraft's spin and thus are disregarded as the instrument observations are contaminated. Table A.2 and Table A.3 lists the auroral properties of the main emission crossings below and above 2 R_J respectively. These tables are divided into subcategories as further explained in the captions.

The first two columns in each table correspond to the perijove and the hemisphere of the crossing. The columns "$L \lesssim 13$" and "$13 \lesssim L \lesssim 16$" refer to the electron distribution observations in the respective regions, with the first referring to diffuse aurora regions and the second to ZI and ZII regions. If the LC is not resolved, no data is provided, or no intensities are seen, this is indicated in those columns. Otherwise, either diffuse, pancake, bidirectional (BI), and upward (UW)/downward (DW) filled loss cones are observed. The columns "UV" and "M-UV" refer to the observations from UVS. The "UV" column describes the pattern of the emissions located around the intense field-aligned electron beams when present. Otherwise, the pattern of the whole flyby is described. The "M-UV" column indicates whether magnetic field surges are aligned with auroral arcs and, if so, provides the expected direction of the field-aligned current. The columns "δB [nT]" and "$f > 0.05$ Hz" refer to the MAG observations, with the maximum magnetic field changes of each crossing given in the "δB [nT]" column. The other column, "$f > 0.05$ Hz," indicates whether small-scale fluctuations on frequencies higher than $f > 0.05$ Hz are observed. If small-scale fluctuations are only observed in diffuse or pancake data regions, then "diffuse" is given. Otherwise, the highest frequency range of detectable fluctuations is provided between 0.5 s − 5 s or 5 s − 14.3 s.

PJ	$L \lesssim 13$	$13 \lesssim L \lesssim 16$	$L \gtrsim 16$	UV	M-UV	δB [nT]	$f > 0.05$ Hz
12 N	Pancake	BI-UW		intense arc	no	NaN	no
09 N		LC not covered		dim	no	NaN	diffuse
16 N		LC not covered		arc	DW	NaN	diffuse
19 S		LC not covered		arc	no	NaN	diffuse

Table A.1: Auroral properties of the main emission crossings dominated by spacecrafts spin

PJ	$L \lesssim 13$	$13 \lesssim L \lesssim 16$	$L \gtrsim 16$	UV	M-UV	δB [nT]	$f > 0.05$ Hz
01 N	Diffuse	BI-UW	low	intense arc	UW	350	diffuse
03 N	Diffuse	BI-UW-DW	low	intense arc	UW	350	diffuse
04 N	Diffuse	BI-UW	low	arc	UW	100	diffuse
06 N	Diffuse	BI-UW	low	arc	peak	200	diffuse
08 N	Diffuse	BI-UW	low	dim	no	200	diffuse
12 N	Diffuse	BI-UW-DW	low	intense arc	peak	200	diffuse
13 N	Diffuse	BI-UW	low	arc	DW	200	diffuse
14 N	Diffuse	BI-UW-DW	low	intense arc	UW	200	diffuse
03 S	Diffuse	BI-UW-DW	low	intense arc	peak	500	diffuse
04 S	Pancake	BI-UW-DW	low	intense arc	UW	100	diffuse
08 S	Diffuse	BI-UW-DW	low	intense arc	UW	200	diffuse
16 S	Diffuse	BI-UW	low	arc	UW	200	diffuse

(a) Low electron intensities at $L \gtrsim 16$ with sufficient pitch angle coverage

PJ	$L \lesssim 13$	$13 \lesssim L \lesssim 16$	$L \gtrsim 16$	UV	M-UV	δB [nT]	$f > 0.05$ Hz
05 N	Diffuse	BI-UW-DW	high	arc	UW	500	diffuse
07 N	Diffuse	BI-UW-DW	high	arc	UW	500	diffuse
20 N	Diffuse	BI-UW-DW	high	dim	no	200	diffuse
01 S	Diffuse	BI-UW-DW	high	patchy	no	500	diffuse
05 S	Diffuse	BI-UW-DW	high	intense arc	UW	350	diffuse
06 S	Diffuse	BI-UW-DW	high	intense arc	UW	500	diffuse
07 S	Diffuse	BI-UW-DW	high	intense arc	UW	350	diffuse
09 S	Diffuse	BI-UW	high	intense arc	UW	350	diffuse
12 S	Pancake	BI-UW-DW	high	intense arc	peak	350	diffuse

(b) High electron intensities at $L \gtrsim 16$ with sufficient pitch angle coverage

PJ	$L \lesssim 13$	$13 \lesssim L \lesssim 16$	$L \gtrsim 16$	UV	M-UV	δB [nT]	$f > 0.05$ Hz
17 S		LC not covered		patchy	no	20	diffuse
13 S		LC not covered		arc	peak	50	diffuse
14 S		LC not covered		intense arc	peak	100	diffuse
20 S		LC not covered		arc	UW	100	diffuse
18 S		no data		arc	peak	100	diffuse
11 S		LC not covered		intense arc	UW	200	diffuse
15 N		no data		patchy	no	350	diffuse
15 N		no data		patchy	no	350	diffuse
18 N		LC not covered		intense arc	UW	500	diffuse
10 S		LC not covered		patchy	no	500	diffuse
15 S		no data		patchy	no	500	diffuse
10 S		LC not covered		patchy	no	500	diffuse
17 N	Diffuse	None	low	outside	no	200	diffuse
19 N	Diffuse	Pan	low	outside	no	NaN	NaN
01 N	Diffuse	BI-UW	high	intense arc	UW	350	diffuse
10 N	Diffuse	BI-UW-DW	high	patchy	no	1000	0.5 s − 5 s

(c) Insufficient pitch angle coverage

Table A.2: Auroral properties of the main emission crossings below 2 R_J

PJ	$L \lesssim 13$	$13 \lesssim L \lesssim 16$	$L \gtrsim 16$	UV	M-UV	δB [nT]	$f > 0.05$ Hz
01 S		no intensity		inside	no	0	no
03 S		no intensity		inside	no	0	no
07 S		no intensity		outside	no	0	0.5 s − 5 s
08 S		no data		inside	no	0	5 s − 14.3 s
10 S		no intensity		intense arc	no	0	5 s − 14.3 s
12 S		no intensity		arc	no	0	0.5 s − 5 s
13 S		no intensity		inside	no	0	5 s − 14.3 s
14 S		no intensity		inside	no	0	no
15 S		no intensity		outside	no	0	no
16 S		no intensity		inside	no	0	no
17 S		no data		inside	no	0	no
19 S		no intensity		outside	no	0	no
20 S		no intensity		outside	no	0	no

(a) Auroral properties of the main emission crossings in poleward or equatorward location with no auroral particle evidence

PJ	$L \lesssim 13$	$13 \lesssim L \lesssim 16$	$L \gtrsim 16$	UV	M-UV	δB [nT]	$f > 0.05$ Hz
09 S		no data		along	no	5	0.5 s − 5 s
18 S		no data		patchy	no	5	no
07 N		no data		arc	UW	5	diffuse
15 N		no data		arc	UW	5	diffuse
04 S	Isotrop	UW	low	intense arc	UW	5	diffuse
05 S	Isotrop	UW	low	intense arc	UW	5	diffuse
06 N	Isotrop	UW	low	dim	no	5	diffuse
09 N		LC not covered		arc	UW	50	diffuse
11 N		LC not covered		arc	UW	200	0.5 s − 5 s
13 N		LC not covered		arc	UW	20	diffuse
14 N		LC not covered		arc	UW	20	diffuse
18 N		LC not covered		arc	UW	200	diffuse
20 N		LC not covered		intense arc	UW	50	0.5 s − 5 s
06 S		LC not covered		arc	no	5	0.5 s − 5 s
11 S		LC not covered		intense arc	UW	50	0.5 s − 5 s
17 N		LC not covered		outside	no	20	diffuse
19 N		LC not covered		outside	no	20	diffuse

(b) Very low intensities electron intensities and no magnetic field deviations.

PJ	$L \lesssim 13$	$13 \lesssim L \lesssim 16$	$L \gtrsim 16$	UV	M-UV	δB [nT]	$f > 0.05$ Hz
03 N	Pancake	BI-UW	low	arc	peak	20	diffuse
08 N	Pancake	UW	low	dim	no	20	diffuse
04 N	Pancake	UW-DW	low	arc	peak	50	diffuse
10 N	Pancake	BI-UW-DW	low	intense arc	peak	100	diffuse
16 N	Pancake	UW	low	arc	UW	200	diffuse
01 N	Isotrop	BI	low	dim	no corr	5	0.5 s − 5 s
05 N	Pancake	BI	low	patchy	no	50	0.5 s − 5 s

(c) Electron beams observed with magnetic field changes.

Table A.3: Auroral properties of the main emission crossings above 2 R_J

A.2 Overview Plots of Supplementary Perijoves

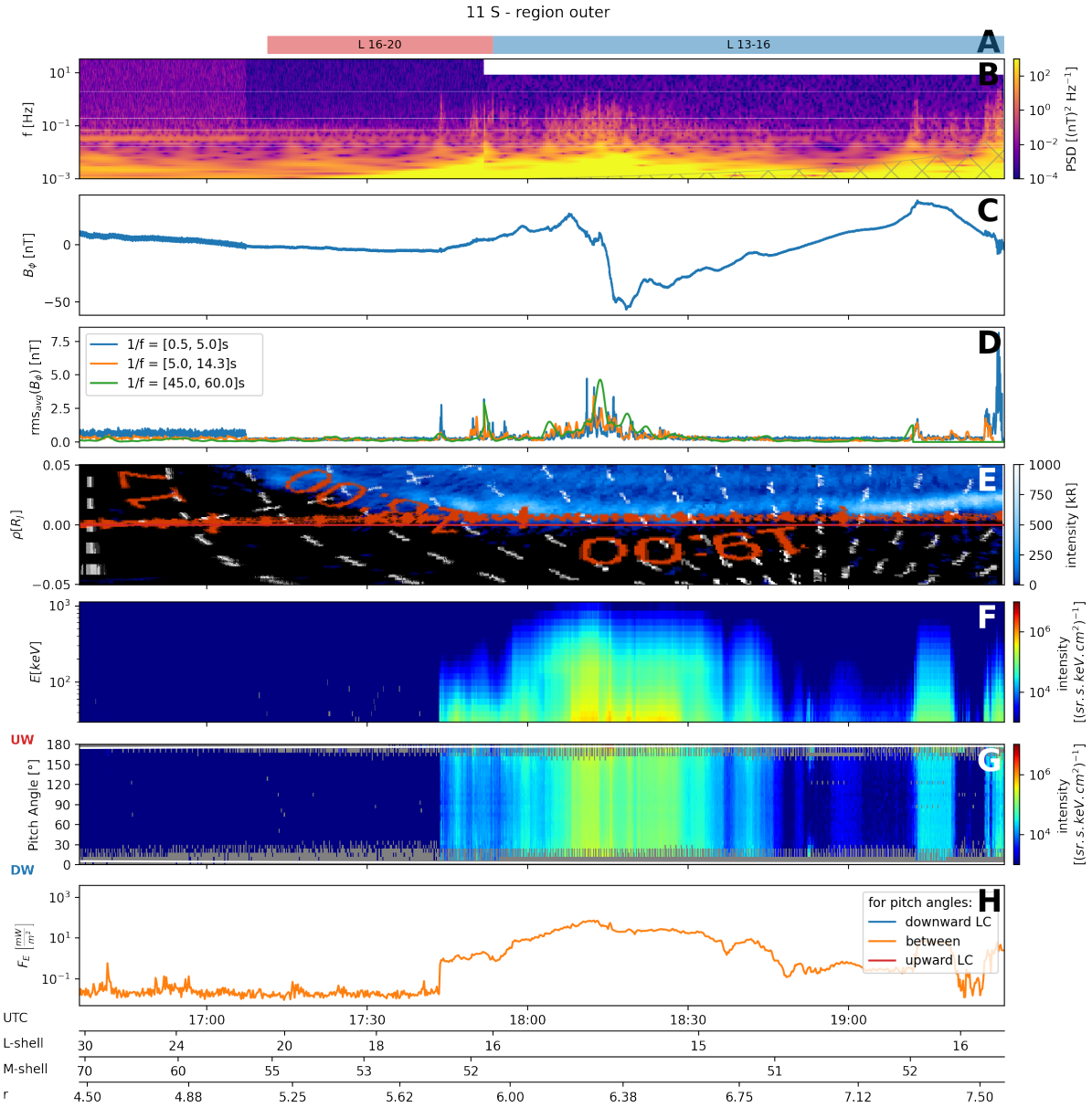

Figure A.1: This figure gives an overview of the instrument data from perijove 11, which passed through the southern hemisphere at altitudes higher than $2\,\mathrm{R_J}$. Further details for each panel are provided in the caption of Figure fig. 4.10.

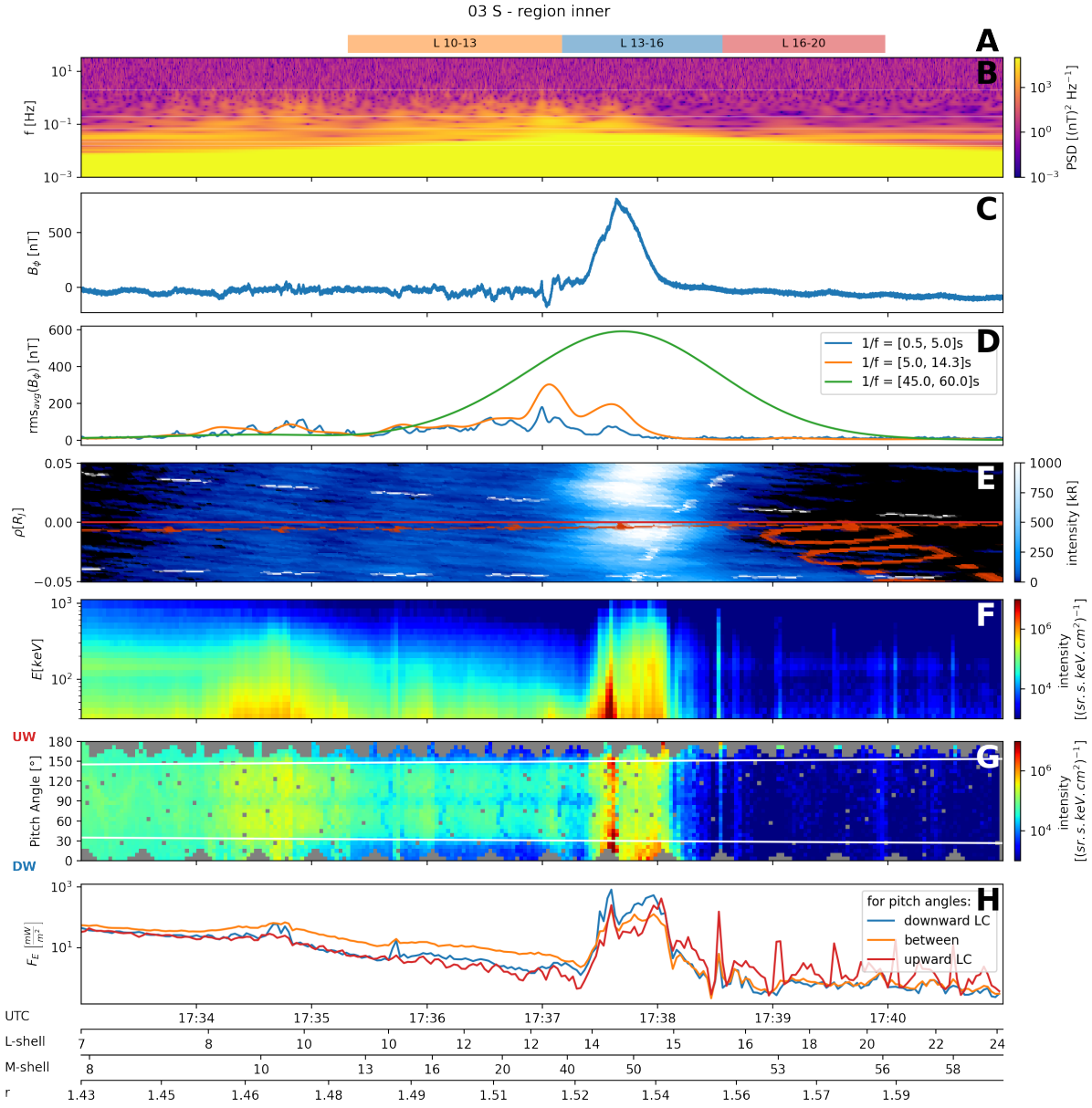

Figure A.2: This figure gives an overview of the instrument data from perijove 3, which passed through the southern hemisphere at altitudes lower than $2\,\mathrm{R_J}$. Further details for each panel are provided in the caption of Figure fig. 4.10.

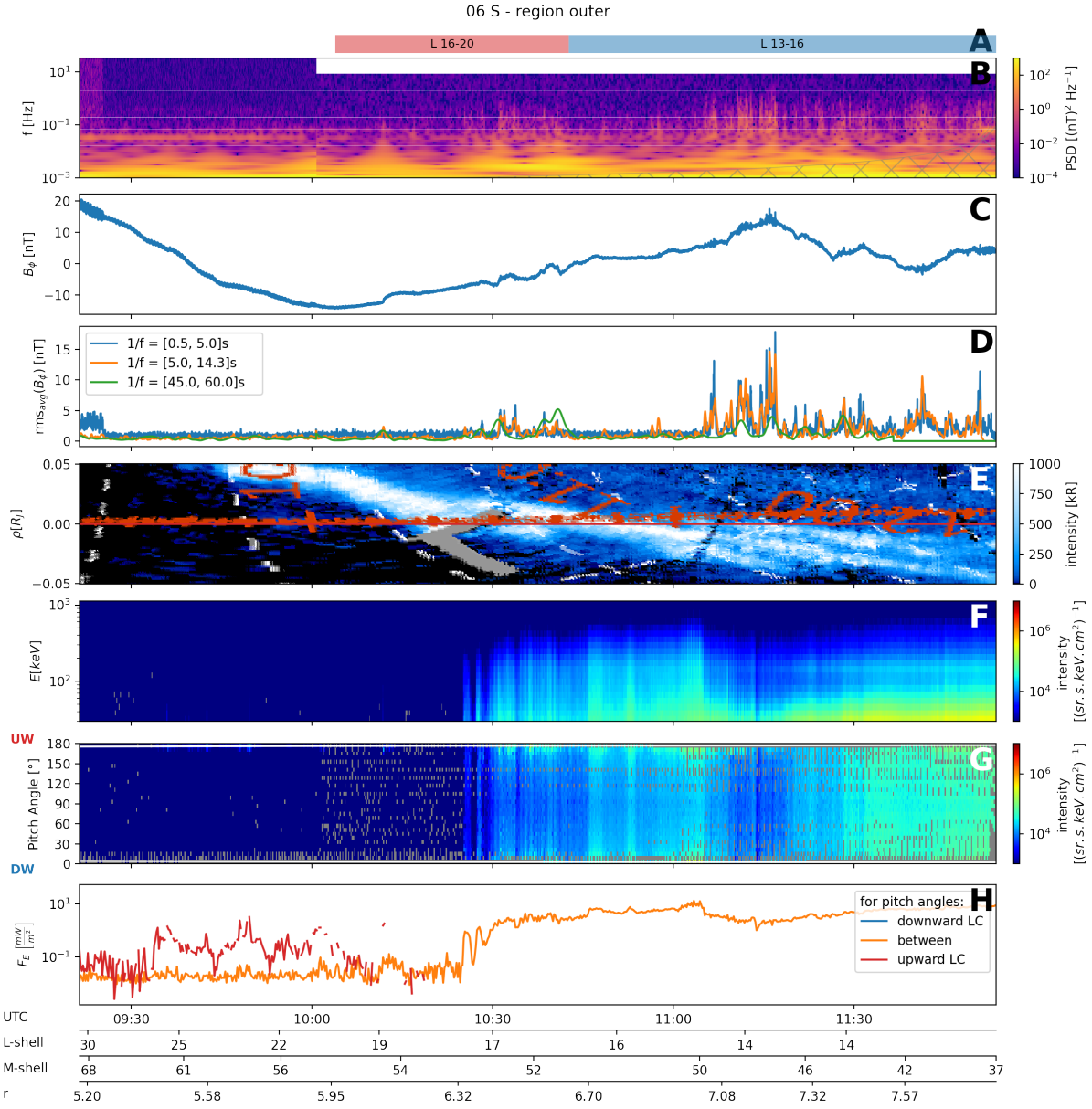

Figure A.3: This figure gives an overview of the instrument data from perijove 6, which passed through the southern hemisphere at altitudes higher than $2\,\mathrm{R_J}$. Further details for each panel are provided in the caption of Figure fig. 4.10.

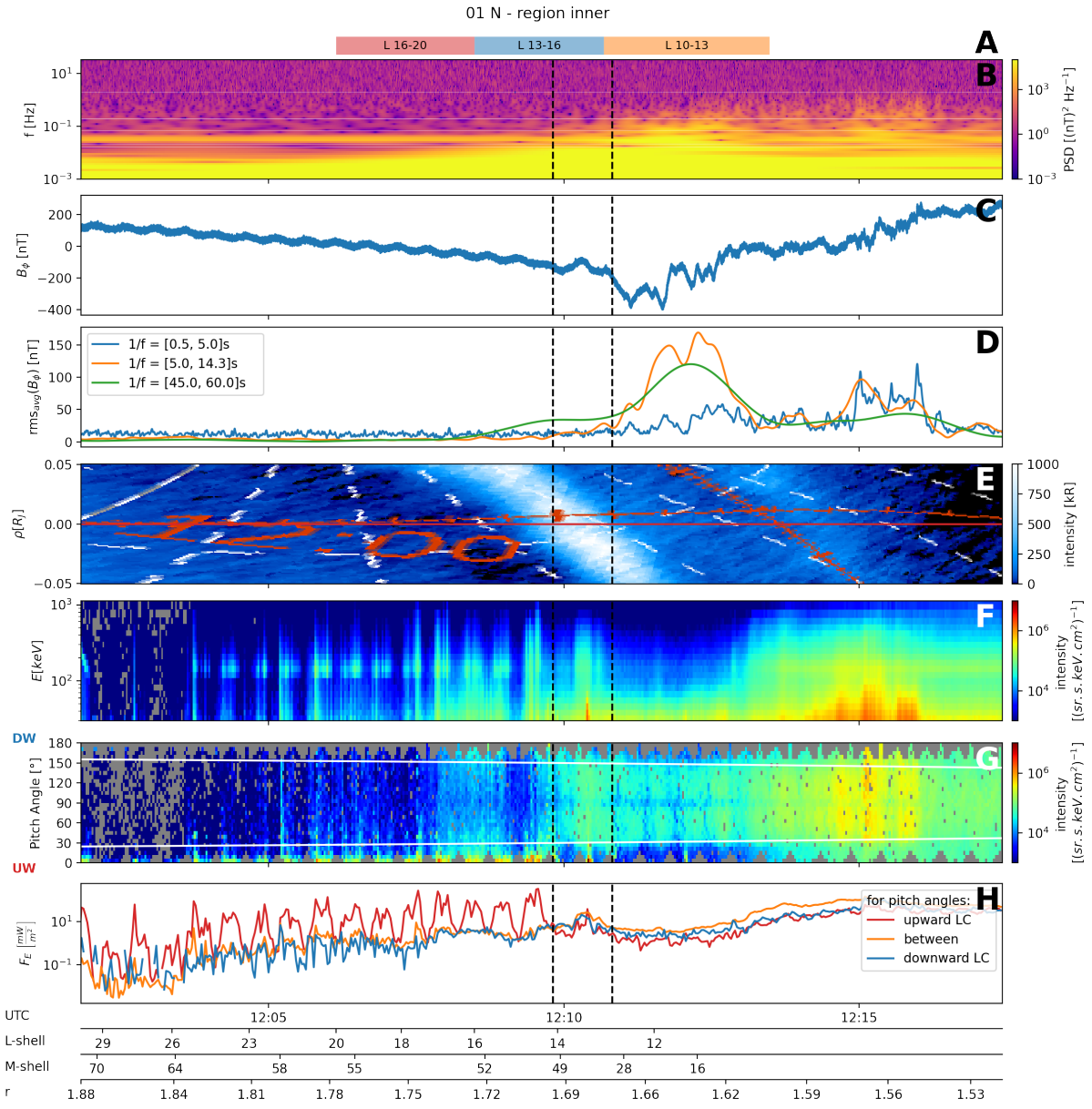

Figure A.4: This figure gives an overview of the instrument data from perijove 5, which passed through the southern hemisphere at altitudes higher than $2\,\mathrm{R_J}$. Further details for each panel are provided in the caption of Figure fig. 4.10. The vertical dashed black lines indicate regions of intense aurora and correspond to strong magnetic field gradients.

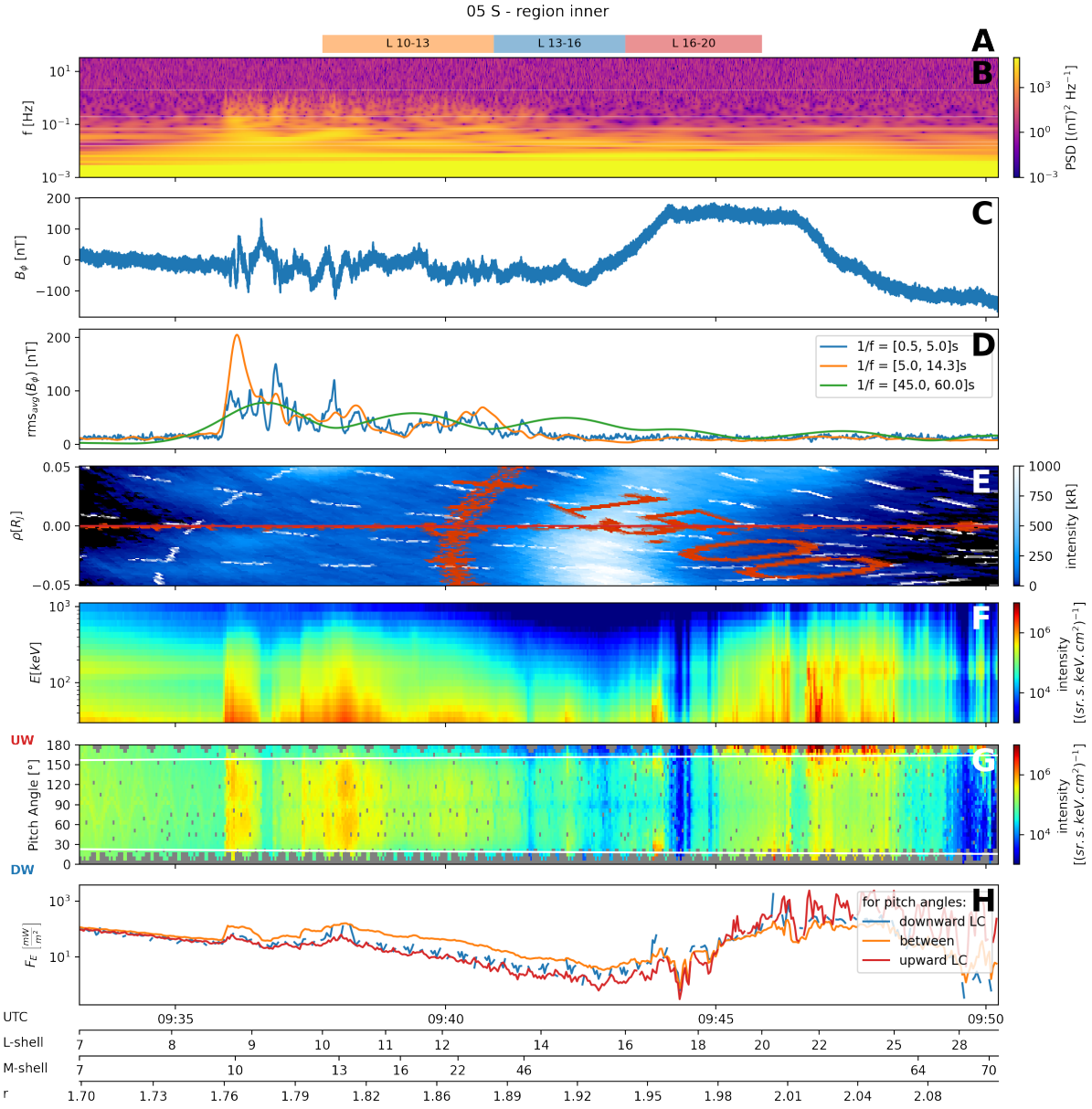

Figure A.5: This figure gives an overview of the instrument data from perijove 5, which passed through the southern hemisphere at altitudes higher than $2\,\mathrm{R_J}$. Further details for each panel are provided in the caption of Figure fig. 4.10. The vertical dashed black lines indicate regions of intense aurora and correspond to strong magnetic field gradients.

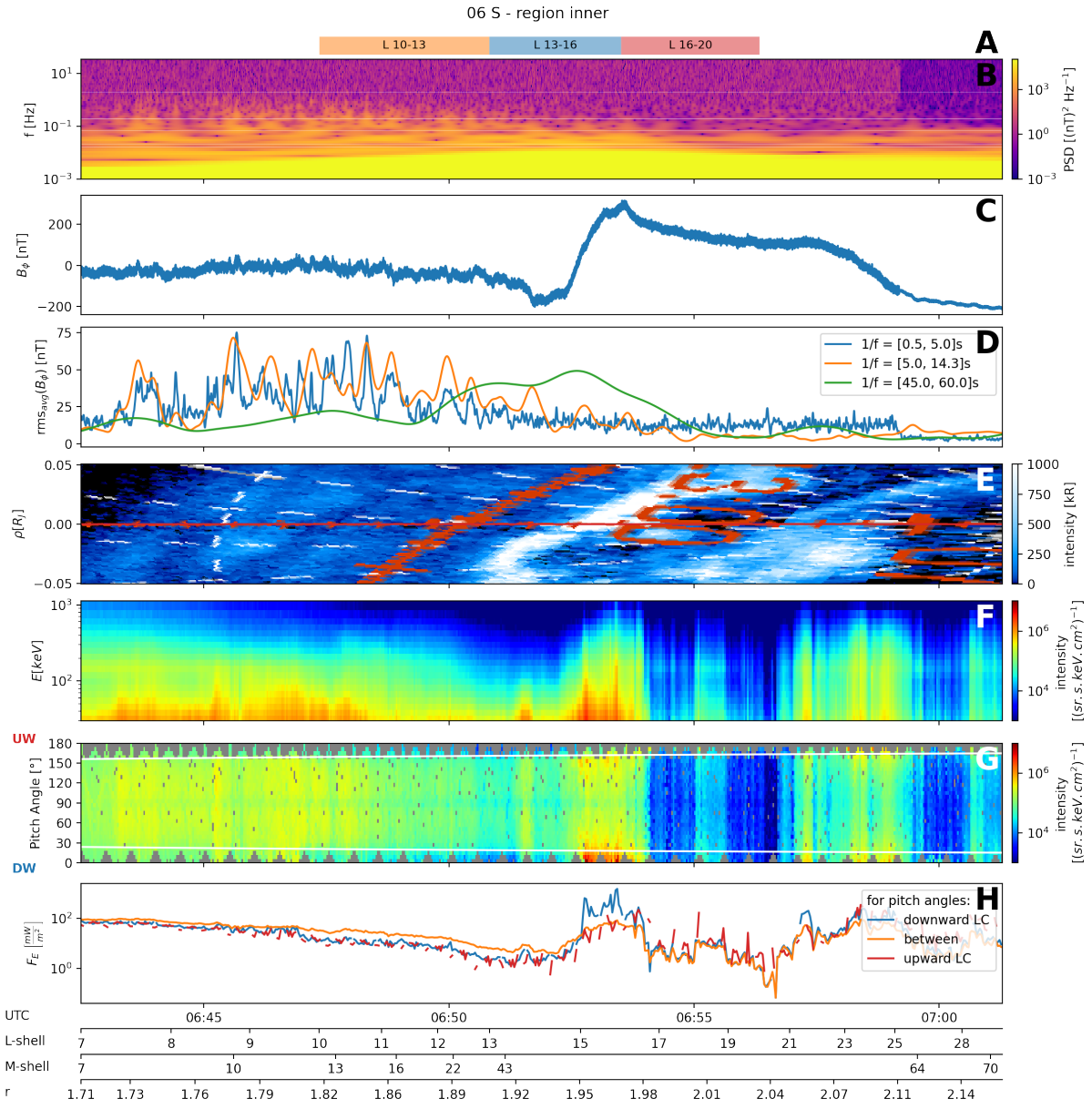

Figure A.6: This figure gives an overview of the instrument data from perijove 6, which passed through the southern hemisphere at altitudes higher than $2\,\mathrm{R_J}$. Further details for each panel are provided in the caption of Figure fig. 4.10. The vertical dashed black lines indicate regions of intense aurora and correspond to strong magnetic field gradients.

A.3 UVS Slice Routine - A Test Image

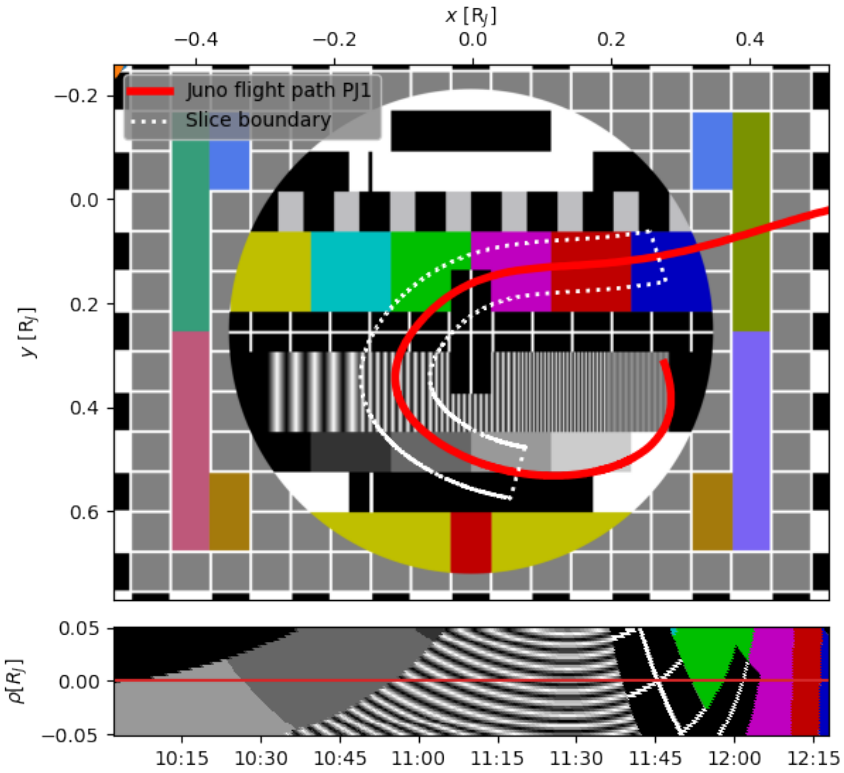

Figure A.7: A graphical representation of a typical flight trajectory (shown in red) is depicted in a kartesian coordinate system. The routine is tested using a standard PAL test pattern. The white lines indicate the enlarged region around the flight trajectory, which is used to plot the background image as an uncurved rectangle plot, with the timeline as the x-axis and the distance ρ from the line of flight in the atmosphere in the y direction.

OPEN RESEARCH AND DATA AVAILABILITY

The Juno-JEDI data (NASA Planetary Data System, 2023) as well as the Juno-Magnetometer data (NASA Planetary Data System, 2022) were obtained from the website of the NASA Planetary Data System:Planetary Plasma Interactions (`https://pds-ppi.igpp.ucla.edu/mission/JUNO/JNO/JEDI` and `https://pds-ppi.igpp.ucla.edu/mission/JUNO/JNO/FGM`). The Juno-UVS calibrated data data can be utilized from `https://pds-atmospheres.nmsu.edu/cgi-bin/getdir.pl?dir=DATA%26volume=jnouvs_3001` to obtain the polar projection images described by Bonfond et al. (2021). Juno footprints are available using JRM09 and Con81 models at `https://lasp.colorado.edu/home/mop/files/2020/04/20190412_Imai_MagFootReader_UIowa_rev.pdf`. Tracing of the magnetic field lines with JRM33 and Con2020 is provided by Wilson et al. (2023). The classification results for calculating the precipitation budget of the different electron distributions are provided as supplementary material in Salveter et al. (2022).

ERKLÄRUNG ZUR DISSERTATION

gemäß der Promotionsordnung vom 12. März 2020

„„Hiermit versichere ich an Eides statt, dass ich die vorliegende Dissertation selbstständig und ohne die Benutzung anderer als der angegebenen Hilfsmittel und Literatur angefertigt habe. Alle Stellen, die wörtlich oder sinngemäß aus veröffentlichten und nicht veröffentlichten Werken dem Wortlaut oder dem Sinn nach entnommen wurden, sind als solche kenntlich gemacht. Ich versichere an Eides statt, dass diese Dissertation noch keiner anderen Fakultät oder Universität zur Prüfung vorgelegen hat; dass sie - abgesehen von unten angegebenen Teilpublikationen und eingebundenen Artikeln und Manuskripten - noch nicht veröffentlicht worden ist sowie, dass ich eine Veröffentlichung der Dissertation vor Abschluss der Promotion nicht ohne Genehmigung des Promotionsausschusses vornehmen werde. Die Bestimmungen dieser Ordnung sind mir bekannt. Darüber hinaus erkläre ich hiermit, dass ich die Ordnung zur Sicherung guter wissenschaftlicher Praxis und zum Umgang mit wissenschaftlichem Fehlverhalten der Universität zu Köln gelesen und sie bei der Durchführung der Dissertation zugrundeliegenden Arbeiten und der schriftlich verfassten Dissertation beachtet habe und verpflichte mich hiermit, die dort genannten Vorgaben bei allen wissenschaftlichen Tätigkeiten zu beachten und umzusetzen. Ich versichere, dass die eingereichte elektronische Fassung der eingereichten Druckfassung vollständig entspricht“

Teilpublikationen:

A. Salveter, J. Saur, G. Clark, and B. Mauk. Jovian auroral electron precipitationbudget—a statistical analysis of diffuse, mono-energetic, and broadband auroral electron distributions. Journal of Geophysical Research: Space Physics, 127(8), 2022. doi: 10.1029/2021JA030224.

October 19, 2024, Annika Salveter